



**FLIGHT CHARACTERISTIC VERIFICATION
OF THE VARIABLE CAMBER COMPLIANT
WING**

THESIS

Sharee B Acosta, Second Lieutenant, USAF
AFIT-ENG-MS-20-M-003

**DEPARTMENT OF THE AIR FORCE
AIR UNIVERSITY**

AIR FORCE INSTITUTE OF TECHNOLOGY

Wright-Patterson Air Force Base, Ohio

DISTRIBUTION STATEMENT A
APPROVED FOR PUBLIC RELEASE; DISTRIBUTION UNLIMITED.

The views expressed in this document are those of the author and do not reflect the official policy or position of the United States Air Force, the United States Department of Defense or the United States Government. This material is declared a work of the U.S. Government and is not subject to copyright protection in the United States.

AFIT-ENG-MS-20-M-003

Flight Characteristic Verification of the Variable Camber Compliant Wing

THESIS

Presented to the Faculty
Department of Electrical and Computer Engineering
Graduate School of Engineering and Management
Air Force Institute of Technology
Air University
Air Education and Training Command
in Partial Fulfillment of the Requirements for the
Degree of Master of Science in Electrical Engineering

Sharee B Acosta, B.S.E.E.
Second Lieutenant, USAF

March 26, 2020

DISTRIBUTION STATEMENT A
APPROVED FOR PUBLIC RELEASE; DISTRIBUTION UNLIMITED.

AFIT-ENG-MS-20-M-003

Flight Characteristic Verification of the Variable Camber Compliant Wing

THESIS

Sharee B Acosta, B.S.E.E.
Second Lieutenant, USAF

Committee Membership:

Robert C Leishman, Ph.D
Chair

David R Jacques, Ph.D
Member

Doug Hunsaker, Ph.D
Member

Abstract

Morphing wing technology gives aircraft the ability to fly various missions in one flight. Morphing technology changes the wing shape to act as the controls of the aircraft. AFIT, AFRL, and USU Aero Lab collaborated to design and test the variable camber compliant wing (VCCW). VCCW has a non-stretch, continuous skin that slides during shape changes and has the ability to eliminate ailerons and flaps.

Flight testing demonstrates the capabilities of the VCCW in roll and yaw controls. The wing has four modes to change the deflection of the trailing edge symmetrically and/or anti-symmetrically. Flight testing provides data collections on how well the VCCW controls work. The data is also incorporated in the simulation refinement.

USU Aero Lab developed a simulation that uses MachUp software to simulate the VCCW in flight. This research focuses on making the simulation performance as close to the actual flight test data. The flight test data has to be filtered and converted to be compatible with the simulation. Once compatible, tuning the simulation involves analyzing control bias and testing thrust models.

This thesis provides a simulation that performs closer to actual flight test data. Simulations help improve situational awareness of the aircraft and decreases human error operation. This research provides a tool to reduce time and cost for flight testing for future wing development.

Acknowledgement

AFIT gave me opportunities that advanced my academic and military career. I am extremely thankful for everything AFIT offered me.

I would like to thank everyone who helped and supported me with my thesis. Thank you to AFIT's ANT Center, AFRL, and USU Aero Lab for letting me be part of your project. It has been an honor working with all of you and I hope to work with you in the future. I would like to give a special thanks to my thesis advisor for mentoring me in my thesis and academic career. Thank you to my father-in-law and undergraduate mentor for reviewing my thesis.

I would like to give an additional thanks to my undergraduate mentor. He believes in my success more than I do. His constant support gave me the the courage to finish my thesis.

Finally, I would like to thank my husband and parents for unconditionally supporting me. They encouraged me everyday (sometimes multiple times a day) that I worked on my thesis. I cannot express my gratitude enough. Thank you and I love you.

Sharee Butuyan Acosta

Table of Contents

	Page
Abstract	iv
List of Figures	viii
List of Tables	xvii
I. Introduction	1
1.1 Background	1
1.2 Problem Statement	2
1.3 Research Objectives	2
1.4 Scope	4
1.5 Limitations and Assumptions	4
1.6 Contribution	5
1.7 Thesis Overview	5
II. Background and Literature Review	7
2.1 Unmanned Aerial Vehicles	7
2.1.1 Low Altitude Fliers	7
2.2 Morphing Wing Technology	8
2.2.1 Advantages of a Morphing Wing	8
2.3 Morphing Wings Types	9
2.3.1 Planform Alteration	12
2.3.2 Airfoil Adjustment	13
2.3.3 Out-of-Plane Transformation	14
2.4 Camber Morphing Wings	16
2.4.1 Variable Wing Camber Development	17
2.4.2 Variable Camber Compliant Wing	18
2.5 Background Summary	22
III. Methodology	23
3.1 Aircraft Dynamics	23
3.1.1 Stability	25
3.2 Variable Camber Compliant Wing Overview	28
3.2.1 Design	28
3.2.2 Controller	29
3.2.3 Flight Modes	31
3.3 Bi-filar Pendulum	32
3.3.1 Procedure	32
3.3.2 Trial Test Improvements	33
3.4 High Speed Static Wind Test	34

	Page
3.5 Flight Test	38
3.5.1 Flight Test Objectives.....	38
3.6 Variable Camber Compliant Wing Simulation	51
3.6.1 MachUp.....	51
3.6.2 Original Simulation	52
3.6.3 Research Simulation Refinement	55
3.7 Methodology Summary.....	57
IV. Results and Analysis	58
4.1 Bi-filar Pendulum	58
4.1.1 Bi-filar Pendulum Test	58
4.1.2 Bi-filar Pendulum Results	62
4.1.3 Verification Test	65
4.2 High Speed Static Wind Test Results	66
4.3 Flight Test	67
4.3.1 Base Wing	68
4.3.2 Variable Camber Compliant Wing Flight Test	69
4.3.3 Flight Analysis	71
4.4 Data Collection Analysis	74
4.4.1 RC Input	75
4.4.2 Airspeed Parameters	77
4.4.3 Sample and Hold	78
4.5 Simulation Refinement	78
4.5.1 Flight Segments	80
4.5.2 Data Conditioning: Filtering	82
4.5.3 Data Conditioning: Aircraft Control Bias	84
4.5.4 Thrust Model	89
4.6 Results and Analysis Summary	110
V. Conclusions	111
5.1 Research Conclusion	111
5.2 Future Work	112
5.2.1 Bi-Filar Pendulum Test Improvement	112
5.2.2 Flight Test Improvement	113
5.2.3 Simulation Improvement	114
5.3 Thesis Conclusion	115
Appendix A. Roll Control Law	116
Appendix B. Yaw Control Law	117
Appendix C. Flight Simulation Plots.....	122
Bibliography	143

List of Figures

Figure		Page
1	Wing morphing technology dates back to 1903. Different morphing types are used to achieve mission criteria in numerous aircraft: twist, sweep, span, chord and camber changes.	11
2	The expandable wing changes its aspect ratio. (a) shows the wing in its expanded state and (b) shows the wing in folded state. The aspect ratio changes from 4.7 to 8.5 in two seconds which decreases drag significantly.	12
3	USSR designed the first aircraft with changing wing chords. The design used six chord-wise overlapping sections that were manually controlled from the cockpit.	13
4	The first camber variation wing was the Parker Camber Variation Wing. The figure shows the ribs of the wing and where the deflection points change the camber shape.	14
5	Gano and Renaud designed the variform wing. The wing has a tank fuel embedded inside. As the fuel depletes, the airfoil decreases.	14
6	Rockwell International created the Active Flexible Wing that used wing flexibility to twist the wing. The wing reduced load and prevent aileron reversal.	15
7	Lockheed-Martin developed Z-wing morphing. The aircraft has the ability to fold its wings toward the center to change the aircraft from a long-range flight to high speed dash and kill and back.	16
8	The pitching-rolling plates use span-wise and chordwise bending. The bending increases thrust production while maintaining propulsive efficiency.	16
9	AFRL's VCCW changes its shape by actuating the leading and trailing edge. a) no deformations b) 6% camber deformed c) twisted d) rear view of (b)	19
10	There were flight complications from the wing surface. Wing comparison before and after take off (a) before with no expansion (b) after take off with ballooning effect	21

Figure		Page
11	Aircraft dynamics components are defined by forces, moments and velocity. There are three axes that have their each dynamic component described in Table 1.	24
12	Phugoid and short period aircraft motion. Phugoid has a longer period and therefore, takes longer to stabilize. Short period stabilizes within a shorter period.	26
13	When aircraft become unstable, they are described in three motions: (a) spiral, (b) roll, and (c) dutch roll. Over time, spiral and dutch roll become more unstable. Roll reaches stability over time.	27
14	The diagram shows the flow of the wing controller. The wing controller involves the receiver, autopilot, controller, and servo. The controller is capable of computing the lift coefficient and deflection angle using the control law.	30
15	Bi-filar pendulums were used to measure the MOI for complex bodies. The test suspended the object and measured the time the object takes to perform one period.	32
16	Vicon recorded data of XY axes test of time vs z rotation of aircraft. (a) shows the raw recording. In order to find the most accurate start and end time of the period, the data is trimmed in (b).	34
17	USU Aero Lab created a model to describe the wing's performance. The model shows the drag and power of aircraft at different air speeds. The minimum drag occurs at 45-48 mph cruise speed.	35
18	The figure shows USU Aero Lab's model to predict the load factor on the wing. The model is described at five different angle of attacks at various air speeds. The deflection angle changes according to the angle of attack. The suggested test points for the 2019 wind test are defined along the load factor line of 3.0, in black dots.	36
19	USU Aero Lab created test points to determine the amount of load the VCCW could withstand. The test points changed the angle of attack, deflection angle, and airspeed.	37

Figure		Page
20	The simulation initializes the aircraft then enters a loop that computes the flight states. The simulation provides a visual of the aircraft with real-time inputs.	53
21	The simulation has graphics to give the user awareness of the aircraft's orientation. a) shows the user in the cockpit and b) shows the user a backside view of the aircraft. All of the flight states are shown along the left and right side of the screen with the corresponding time step and flight time at the bottom of the screen.	54
22	The plot displays all of the flight states. The figure shows $[u, v, w, p, q, r, \phi, \theta, \psi, \dot{p}, \dot{r}, \delta_e, \delta_r, lo, lm, li, ro, rm, ri]$. This was a nominal flight of four seconds to use all control inputs.	55
23	The plot displays the comparison between the actual flight data and the calculated simulation data. The simulation flight is in blue and the actual flight data is in orange. The data is a nine second snippet of a flight. The simulation data stops around five seconds because the aircraft's altitude was zero.	56
24	Bi-filar pendulum testing configurations shown in (a) roll, (b) pitch, and (c) yaw. The aircraft could not be suspended directly through the CG as holes could not be made in the aircraft. The difference between the suspension point and CG provided the calculated MOI at the CG.	60
25	Testing on the VCCW occurred after all the flight test were completed. The aircraft is in the roll configuration and suspended by the fuselage to prevent damage to the wing. One of the Vicon cameras is shown in the top right corner. The 15° rotation marker is shown below the aircraft.	61
26	Base wing during take off. The base wing has all of the standard control capabilities: aileron, elevator, and rudder. The fuselage is designed to use either the base wing or VCCW.	69

Figure		Page
27	The VCCW shows anti-symmetric trailing edge deflection. The right ribs are deflecting the edge down. The deflection changes cause the wind to blow over the wing creating lift on the wing to control the aircraft.	70
28	The plot shows the RC input for aileron and rudder and the attitude for roll and yaw. The aileron and roll plots shows the roll capabilities of the aircraft. The yaw plot helps determine the orientation of flight. The roll attitude ranges from about -50 to 10°.	72
29	The plot shows the RC input for aileron and rudder and the attitude for roll and yaw. The aileron and roll plots shows the roll capabilities of the aircraft. The roll attitude ranges from about -52 to 18°.	73
30	The plot shows zoomed version of Figure 29. There is no rudder input in this plot with one pass of left and right aileron turns.	74
31	The relationship between PWM and degree measurements are linear. The elevator and rudder equations were used to convert the PWM values into degrees of deflection. The elevator relationship is $y = -0.0282x + 44.306$ and the rudder relationship is $y = -0.0353x + 52.556$ where x is the PWM value and y is the corresponding degree value.	76
32	The figure shows flight path of the entire flight and each segment. Take off and landing are the origin. The winds for this flight was two mph SSW. The entire flight is in a blue dashed line, Segment A is a solid green line, Segment B is a solid red line, Segment C is a solid black line, and Segment D is a sold magenta line.	81
33	The figure shows the original output of the simulation for the Segment B. Blue shows the simulation data and orange shows the actual flight data. Flight states of u , v , w , p , q , r , ϕ , θ , and ψ are compared.	82

Figure	Page
34	The plot contains the original angular rate p data and filtered data. The data was processed through a lowpass filter with a bandpass frequency of 0.3. The simulation took the first data point and calculated the rest of the aircraft's flight. Filtering the noise provided more accurate data for the simulation. 83
35	Segment C data (blue = simulation, orange = actual flight). (a) shows the original RC input and (b) shows the bias removed from the RC control input. (b) shows closer trends in v , w , q , r , and ψ . Although the bias was less than 1° , the bias changed all of the flight states. 88
36	The figure shows the Design I: Segment A's thrust model. (a) shows the entire flight segment data. (b) shows the trimmed data from 0 to 50. The trimmed data can produce another thrust model of T constants that will be more closely correlated. 92
37	The simulation results used the original T constants ($T0 = 28.8$, $T1 = 0.1263$, $T2 = -0.0022$) on the Segment C flight. There are trends for p , q and some of ψ 94
38	The simulation results used the trimmed Segment A (1:50) T constants ($T0 = -205.1880$, $T1 = 5.4134$, $T2 = -0.0211$). The model was used on the Segment C flight. There are trends in v , p , and r 95
39	The simulation results used the trimmed Segment C (1:100) T constants ($T0 = 6193.8251$, $T1 = -127.0050$, $T2 = 0.6364$). The model was used on the Segment C flight. There are trends in w , q , and r . There are similar trends on half of the data for the θ and ψ 96
40	The graphs show the relationship between the throttle, propeller rotation rate and thrust. With these two equations, there was a direct relationship between the throttle and thrust. The simulation provided the throttle input and this model provides one value for the thrust found in (20). 97
41	The graph shows the relationship between the throttle and the thrust of the VCCW aircraft. The thrust peaks around 80-100% throttle. 98

Figure	Page
42	(a) shows the MotorCalc model and (b) shows the VCCW model on Segment A. The results are almost identical. In the VCCW model, the u and w velocity is a little faster. 100
43	(a) shows the MotorCalc model and (b) shows the VCCW model on Segment B. The results are almost identical. The VCCW model is a little faster and the Euler angles are more drastic. 101
44	(a) shows the MotorCalc model and (b) shows the VCCW model on Segment C. There are a lot of the same trends. However, the VCCW model has results closer to the actual flight test. 102
45	(a) shows the MotorCalc model and (b) shows the VCCW model on Segment D. The results are almost identical. The u and w velocity are faster in the VCCW model. 103
46	(a) shows the least squares model and (b) shows the static model on Segment A. There are similar characteristic trends for v , w , p , q , r , ϕ and ψ 105
47	(a) shows the least squares model and (b) shows the static model on Segment B. There are similar characteristic trends for p and r 106
48	(a) shows the least squares model and (b) shows the static model on Segment C. There are similar characteristic trends for v , w , p , r , ϕ and ψ 107
49	(a) shows the least squares model and (b) shows the static model on Segment D. There are similar characteristic trends for v , θ , and ψ 108
50	This is the first iteration of the simulation for Segment A. The blue shows the simulation data and the orange shows the actual flight data. The results use the raw control input data. There are all the flight characteristics: u , v , w , p , q , r , ϕ , θ , and ψ 123

Figure	Page
51	This is the first iteration of the simulation for Segment B. The blue shows the simulation data and the orange shows the actual flight data. The results use the raw control input data. There are all the flight characteristics: $u, v, w, p, q, r, \phi, \theta$, and ψ 124
52	This is the first iteration of the simulation for the Segment C. The blue shows the simulation data and the orange shows the actual flight data. The results use the raw control input data. There are all the flight characteristics: $u, v, w, p, q, r, \phi, \theta$, and ψ 125
53	This is the first iteration of the simulation for Segment D. The blue shows the simulation data and the orange shows the actual flight data. The results use the raw control input data. There are all the flight characteristics: $u, v, w, p, q, r, \phi, \theta$, and ψ 126
54	This is the second iteration of the simulation for Segment A. The blue shows the simulation data and the orange shows the actual flight data. There was an input bias on the aileron, elevator and rudder. However, the elevator bias was too drastic. This iteration removes the bias for the aileron and rudder. 127
55	This is the second iteration of the simulation for Segment B. The blue shows the simulation data and the orange shows the actual flight data. There was an input bias on the aileron, elevator and rudder. However, the elevator bias was too drastic. This iteration removes the bias for the aileron and rudder. 128
56	This is the second iteration of the simulation for Segment C. The blue shows the simulation data and the orange shows the actual flight data. There was an input bias on the aileron, elevator and rudder. However, the elevator bias was too drastic. This iteration removes the bias for the aileron and rudder. 129

Figure	Page
57	This is the second iteration of the simulation for the Segment D. The blue shows the simulation data and the orange shows the actual flight data. There was an input bias on the aileron, elevator and rudder. However, the elevator bias was too drastic. This iteration removes the bias for the aileron and rudder. 130
58	This is the third iteration of the simulation for Segment A. The blue shows the simulation data and the orange shows the actual flight data. This simulation uses the Least Squares Approach Design I: Segment C thrust model. 131
59	This is the third iteration of the simulation for Segment B. The blue shows the simulation data and the orange shows the actual flight data. This simulation uses the Least Squares Approach Design I: Segment C thrust model. 132
60	This is the third iteration of the simulation for Segment C. The blue shows the simulation data and the orange shows the actual flight data. This simulation uses the Least Squares Approach Design I: Segment C thrust model. 133
61	This is the third iteration of the simulation for the Segment D. The blue shows the simulation data and the orange shows the actual flight data. This simulation uses the Least Squares Approach Design I: Segment C thrust model. 134
62	This is the fourth iteration of the simulation for Segment A. The blue shows the simulation data and the orange shows the actual flight data. This simulation uses the MotorCalc static thrust model. 135
63	This is the fourth iteration of the simulation for Segment B. The blue shows the simulation data and the orange shows the actual flight data. This simulation uses the MotorCalc static thrust model. 136
64	This is the fourth iteration of the simulation for Segment C. The blue shows the simulation data and the orange shows the actual flight data. This simulation uses the MotorCalc static thrust model. 137

Figure		Page
65	This is the fourth iteration of the simulation for the Segment D. The blue shows the simulation data and the orange shows the actual flight data. This simulation uses the MotorCalc static thrust model.	138
66	This is the fifth iteration of the simulation for Segment A. The blue shows the simulation data and the orange shows the actual flight data. This simulation uses the VCCW static thrust model.	139
67	This is the fifth iteration of the simulation for Segment B. The blue shows the simulation data and the orange shows the actual flight data. This simulation uses the VCCW static thrust model.	140
68	This is the fifth iteration of the simulation for Segment C. The blue shows the simulation data and the orange shows the actual flight data. This simulation uses the VCCW static thrust model.	141
69	This is the fifth iteration of the simulation for the Segment D. The blue shows the simulation data and the orange shows the actual flight data. This simulation uses the VCCW static thrust model.	142

List of Tables

Table		Page
1	Aircraft has forces, moments and velocity components in three axes	24
2	The table shows all the test points for the base wing flight testing. The same maneuvers were performed with different rudder mixing, deflection level, and speed to provide a vast data collection on the flight states.	41
3	Bi-Filar Pendulum Base Wing Results. Average MOI and standard deviation are calculated from the all of the MOI from each configuration. Roll MOI = 2.08 kg m ² , pitch MOI = 1.95 kg m ² , and yaw MOI = 3.29 kg m ²	63
4	Bi-Filar Pendulum Variable Camber Compliant Wing Results. Roll MOI = 4.67 kg m ² , pitch MOI = 1.75 kg m ² , and yaw MOI = 5.47 kg m ² . The standard deviations are better as a whole than the base wing testing.	64
5	80/20 Rod Verification Test Results on Bi-Filar Pendulum. The test was completed to compare how accurate the method was to the actual MOI measurement. The test had a 0.7315% error.	66
6	The aircraft had a bias on the RC input. All of the average RC input for the aileron, elevator and rudder controls were calculated. The table shows the bias values for each segment.	84
7	The table shows the average of all of the additional flight sections with its respective segment from Table 6 for the aileron, elevator, and rudder. The average uses flight data outside of the Segments A-D to give a variety of controls in addition to the actual flight.	85
8	Design I and II produced different T constants. The highlighted constants were the best performing thrust models. The rest of the models had unstable flights in the simulation.	91

Table		Page
9	The models that had closely matched Y relationships were put through another iteration of the least squares thrust approach. The model and actual data were compared through the entire data set. The highlighted model shows the best performing model. However, the simulation performed best when the values were inverted.	93
10	There were three least square models that performed well against the respective flight. To find the best model, each of the models was simulated with all of four segments.	94

I. Introduction

1.1 Background

The research on morphing wings has many different directions. Wing morphing started with the Wright Brothers. They developed a twisting wing to control the roll maneuver [1]. Today, morphing wing research is developing on all different types of aircraft (advanced fighters, transporters, helicopters, and unmanned aerial vehicles). Morphing technology allows the wing to control the aircraft by replacing the use of ailerons and rudders which results in optimizing the lift and drag characteristics for various flight conditions [2]. There are many ideas of how to morph wings to best fit the flight conditions. For example, Dr. Inman, Ph.D Mechanical Engineering, based his research on how birds fly and their wing shapes [3][4]. Changes in wing geometry create different aircraft controls. As another example, extending the leading and trailing edge allows for control along the wing surface [3][5].

Air Force Research Lab (AFRL) started morphing wing research in 2013. They began conjoint work with Utah State University (USU) Aero Lab in 2016 and the Air Force Institute of Technology (AFIT) in 2018. The combined efforts resulted in research of a morphing wing on a unmanned aerial vehicle (UAV) that moves the leading and trailing edge simultaneously, known as a variable camber compliant wing (VCCW). Their work involved designing and building the wing, developing the morphing shape for flight, and executing flight test.

There were different roles in developing the VCCW. AFRL designed and built

the VCCW. USU Aero Lab developed the calculations for wing deflection. The wing deflection provides roll and yaw surface control of the aircraft. AFIT performed system integration and provided the test team to execute flight test for the VCCW.

1.2 Problem Statement

The VCCW is new technology that is not validated on a working prototype. There are few tools to verify if the flight will be successful. Is the VCCW capable of equilibrium flight involving various maneuvers without sustaining damage? Is it possible to refine a flight simulation that aligns with the actual flight test data? Verifying the VCCW capabilities and improving the simulation would make future research more efficient for the Department of Defense (DoD) by reducing the cost and time consumption of flight testing.

1.3 Research Objectives

The purpose of this research is to verify the VCCW's performance through flight test and simulation. Flight testing will demonstrate the roll and yaw surface control of the VCCW. All of the flights need to have stable control of the aircraft without any damage to the wing. Flight testing will also provide data collections of flight states to refine the VCCW simulation. The data collection will show the correlation between the actual flight data and simulation performance. The simulation will serve as a tool to predict flight outcomes in various environments.

The VCCW provides aircraft control that eliminates the need for ailerons and flaps. This research will provide the DoD with a tool to further develop the VCCW. The DoD wants to develop a morphing winged system that is more efficient than a standard wing. In this research, the VCCW uses a programmed controller to morph the wing.

Human error, when working with autonomous technology, has been found to be the result of poor situational awareness [6]. Situational awareness has three levels: perception of current status, comprehension of current status and projection of future status. A solution to improve situational awareness in the projection of future status is simulation use [6]. This research will focus on refining a simulation to improve situational awareness for the VCCW user. The simulation will provide more time for the user to understand the capabilities of the system and how to best operate the aircraft.

Objectives:

- Verify capabilities of the VCCW prototype
 - Develop test points to demonstrate flight capabilities
 - Execute flight test for VCCW prototype
 - Record flight test data
 - Analyze flight test data
- Measure moment of inertia (MOI) for VCCW
 - Perform bi-filar pendulum test
 - Analyze data
 - Verify measuring method
- Refine simulation that shows close alignment to flight test data
 - Convert flight test data to be compatible with the simulation
 - Tune flight parameters to improve simulation performance

1.4 Scope

This research has three parts: MOI measurement, flight testing, and simulation refinement. The MOI will be measured using the bi-filar pendulum test. The measurement is essential to understanding the flight states of the VCCW.

The second part of this thesis will demonstrate the capabilities of the VCCW through flight testing. The flight test focus on executing and recording the results of each flight. The flight test objective is to demonstrate viable control of the aircraft during flight.

The third part of this work attempts to create a python simulation, built upon USU Aero lab MachUp [7][8], that closely replicates the aircraft's physical states obtained from original flight data. The simulation will use the flight test data as input values and will have the same physical parameters as the aircraft flown during flight testing. The simulation will help future flight tests and studies of the VCCW. The research will help verify the VCCW design.

1.5 Limitations and Assumptions

There were some limitations and assumptions throughout this research. All flight test data collection came from the Pixhawk autopilot. The Pixhawk recorded the data at different time stamps. The time and data had to be interpolated to best fit the frequency of recorded data set.

The Pixhawk did not completely capture all of the flight data. There are assumptions of the aircraft's velocity on the ground versus airspeed. The pitot tube was the only tool to calculate the airspeed of the aircraft. It is noted that the pitot tube captures only the longitudinal component of the airspeed.

This research assumed the wind speed estimates from the autopilot were correct. These estimates are developed by the autopilot from comparisons between ground

speed (from GPS) and measured airspeed (from the pitot tube). The quality of the data was questionable in comparison to online weather sources.

1.6 Contribution

This thesis work contributes to various parts of the AFRL funded project. The thesis will provide verification and characterization for the VCCW. This research contributes the following areas:

1. Measure and estimate the aircraft's moment of inertia
2. Lead flight testing on the prototype aircraft as one of the test directors
3. Refine a simulation to predict flight behaviors of real system
4. Verify the VCCW model.

1.7 Thesis Overview

This thesis contains five chapters (including Chapter I). Chapter II is the background of morphing wings. It reviews previous research on standard airplanes and on UAVs. Chapter III provides the methodology of the thesis. Chapter IV presents the analysis of the research. Chapter V summarizes this thesis and future work opportunities.

Chapter II provides background on morphing wing technology. The chapter gives a brief overview of UAVs then breaks down morphing wing technology. There are three different categories of morphing wings: planform alteration (span, chord and sweep morphing) [2][9][10][11][12][13], airfoil adjustment (thickness and camber) [2][14][15][16][17], and out-of-plane transformation (twist, span-wise bending and gull) [2][9][18][19][20][21][22][23][24]. Chapter II discusses morphing wings advantages over

conventional controls (aileron, elevator, and rudder). Finally, the chapter finishes with camber variation development to include the most recent research from AFRL. AFRL created the VCCW which is the precedent work of this thesis.

Chapter III focuses on the process for the research. In order to understand flight states, the chapter explains the aircraft dynamics and stability of flight. A vital measurement to characterize the VCCW is the moment of inertia (MOI). The MOI is measured using the bi-filar pendulum test [25]. The chapter then explains the VCCW testing that includes a high speed static wind test and flight testing. The high speed static wind test is a checkout test to confirm the wing can withstand loads during flight. Flight testing will demonstrate the capabilities of the wing. Finally, the chapter discusses the refinement of the VCCW simulation. The simulation uses the flight data to closely match the simulation performance to flight tests.

Chapter IV discusses the results and analyzes the research data. The chapter reviews the results from the bi-filar pendulum and flight testing. All of the flight test data is analyzed to convert for future work. The chapter finishes with simulation refinement. The simulation refinement includes data filtering, aircraft control bias, and thrust models.

Finally, Chapter V is the research conclusion. The chapter explores the significance of the research and future work suggestion. There are future work suggestions for the bi-filar pendulum test, flight testing, and simulation refinement.

II. Background and Literature Review

Chapter II provides background on unmanned aerial vehicles and morphing wing technology. Morphing wing technology has three major types of morphing: plan-form alteration (span, chord and sweep morphing) [2][9][10][11][12][13], airfoil adjustment (thickness and camber) [2][14][15][16][17], and out-of-plane transformation (twist, span-wise bending and gull) [2][9][18][19][20][21][22][23][24]. All morphing types provide advantages over conventional aircraft control. Because this research work focuses on camber morphing, the chapter talks explores more camber variation research. Finally, the chapter discusses the development of this research project: the variable camber compliant wing (VCCW).

2.1 Unmanned Aerial Vehicles

Unmanned aerial vehicles (UAVs) are aerial vehicles that do not carry a human operator. The vehicle has the ability to fly autonomously or through remote piloting [5][26]. UAV technology allows for higher levels of risk without harming the human operator. UAVs also have the mobility to travel around rough landscape and urban areas [27]. There are five groups to classify UAVs. Classification depends on the aircraft's weight, operating altitude, and speed [5][26]. Specifically for this thesis, the UAV is classified as group two.

2.1.1 Low Altitude Fliers

A low altitude flier has specific characteristics and abilities. Natural fliers such as birds and UAVs are categorized as low altitude fliers [5][26]. Tailwind increases side-slip three times greater in low altitude fliers [5][26]. Increased side-slip results in more rudder actuation but a more efficient cambered actuation. Headwind initiates

side-slip but low altitude fliers can easily correct for it using greater propulsion to maintain forward flight. Headwinds do not induce a side-slip greater than 90° [5][26].

Low altitude fliers do not fly higher than 3500 AGL because of the high winds and weather. However, the wind speeds below 3500 AGL can be the same or faster than the fliers maximum velocity. Therefore, they experience a wind magnitude that is greater than their velocity [5].

2.2 Morphing Wing Technology

Morphing wing technology gives an aircraft wing or structure the ability to change size and shape during flight [2][22][28]. The wing or structure transformation allows the aircraft to change its standard performance. The performance includes the flight time, weight, and maneuverability [2][22][28]. Each technique manipulates specific characteristics according to the mission and flying environment.

Morphing wing technology is still evolving. There is on-going research to optimize and understand the performance of each design. Because the morphing wing is still evolving, there is not a clear definition of “shape morphing.” [2] Shape morphing involves geometric change but researchers have not determined the magnitude of geometric change to qualify as shape morphing [2].

2.2.1 Advantages of a Morphing Wing

Morphing wings provide many capabilities that a conventional wing cannot. Wings change their shape to control roll and yaw through geometry changes or twisting of the wing [2][22][28]. The ability to morph the wing allows the aircraft to operate in various flight conditions. Morphing wings can also perform multiple missions in one flight such as long range flight and high-speed dash [22][23]. A morphing wing can operate in some ways like how a bird changes wing shape to change its flight

parameters [3][22].

Morphing wings can control the distribution of pressure along the wing [29][30][31]. Depending on the flight conditions and maneuvers, the aircraft experiences various loads. A standard wing design focuses on the ability to withstand structural loads from all of the aircraft's flight capabilities. Morphing wing geometry can improve the lift distribution which decreases the load on the wing [29][30][31]. Current designs minimize drag at cruise lift conditions to withstand maneuvers of at least 2.5 g's as federal regulation requirements [30]. Morphing technology gives the aircraft different lift distributions during flight maneuvers other than just cruise flight conditions.

Changing the lift distribution allows for lateral control [29][30][32]. Lateral movements are controlled by roll and yaw inputs. The standard wing uses ailerons to control rolling maneuvers in flight. However, ailerons cause adverse yaw. Adverse yaw is a force that causes the aircraft to yaw in the opposite direction that the pilot desires to roll and comes from increasing lift on one wing and decreasing drag on the other [32]. Because of the aileron effects of adverse yaw, the aircraft must compensate with vertical stabilizers and rudders [29][30]. Morphing wings can eliminate adverse yaw and remove the need for ailerons, vertical stabilizers and rudders [30][31].

Geometry changes allow for different control of the aircraft. Extending the leading and trailing edge allows the wing to control wing surfaces along the camber at each segment of the wing [3]. Asymmetric wing extension allows the camber to produce effective rolling and yawing moment and counteract disruption in the rolling and yawing motion [5][33].

2.3 Morphing Wings Types

The Wright Brothers developed a twisting wing to control the roll of the aircraft. Their aircraft twisted the wing tips in different directions [1][28]. When the right

wing tip was twisted upward, the left wing tip was twisted downward. The wing design rotated like a windmill and allowed the aircraft to control roll. The wing also produced greater lift on one side of the aircraft than the other [1].

Since the years of the Wright Brothers, there have been many developments in morphing wings: twist, sweep, span bending, bi-to monoplane, gull, chord, camber, pitch and folding, to name a few, all of which involve geometry changes of the wing [2]. The type of morphing depends on the mission of the aircraft. Geometry changes are classified into three categories: planform alteration (span, chord and sweep morphing) [2][9][10][11][12][13], airfoil adjustment (thickness and camber) [2][14][15][16][17], and out-of-plane transformation (twist, span-wise bending and gull) [2][9][18][19][20][21][22][23][24]. Figure 1 [2] shows a timeline of the different morphing technology.









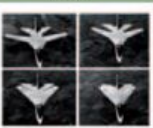
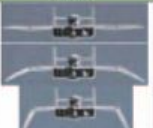

























1903	1931	1931	1932	1937	1947	1951
						
Wright Flyer <i>Twist</i>	Pterodactyl IV <i>Sweep</i>	MAK-10 <i>Span</i>	IS-1 <i>Bi-to monoplane</i>	LIG-7 <i>Chord</i>	MAK-123 <i>Span</i>	X 5 <i>Sweep</i>
1952	1964	1964	1966	1967	1967	1969
						
XF10F <i>Sweep</i>	F 111 <i>Sweep</i>	XB 70 <i>Span bending</i>	Su 17 IG <i>Sweep</i>	MIG 23 <i>Sweep</i>	SU 24 <i>Sweep</i>	Tu 22 M <i>Sweep</i>
1970	1972	1974	1974	1979	1981	1985
						
F 14 <i>Sweep</i>	FS 29 <i>Span</i>	B 1 <i>Sweep</i>	Tornado <i>Sweep</i>	AD 1 <i>Obliquing</i>	Tu 160 <i>Sweep</i>	AFTI/F 111 <i>M.A.W.</i>
1993	1994	2001	2002	2003	2004	2005
						
FLYRT <i>Span</i>	MOTHRA <i>Camber</i>	AAL <i>Pitch</i>	F/A 18 <i>A.A.W.</i>	Virginia Tech <i>Span</i>	Univ. of Florida <i>Twist</i>	Univ. of Florida <i>Gull</i>
2006	2006	2007	2007	2007	2008	2010
						
MFX 1 <i>Sweep & Span</i>	Univ. of Florida <i>Sweep</i>	Virginia Tech <i>Camber</i>	Univ. of Florida <i>Folding</i>	MFX 2 <i>Sweep & span</i>	Delft Univ. <i>Sweep</i>	Virignia tech <i>Camber</i>

Figure 1: Wing morphing technology dates back to 1903. Different morphing types are used to achieve mission criteria in numerous aircraft: twist, sweep, span, chord and camber changes.

2.3.1 Planform Alteration

Planform alteration includes span change, chord length change, and sweep angle change [2][9][10][11] [12][13]. Span and sweep angle changes are mainly used for fixed wings while chord length changes are used for rotary [9].

Span and sweep changes affect the wing's aspect ratio, which is based off the wing area. Changing the aspect ratio ultimately affects the lift-to-drag ratio [2][9][10]. If the aspect ratio increase, then there is more lift and less drag. Therefore, the endurance and range of the aircraft increases. For example, the expandable morphing wing was created in 2005 [12][13]. The wing had the ability to change its aspect ratio from 4.7 to 8.5 in two seconds. The wing change resulted in decreasing drag by more than 10% [12][13]. Figure 2 [12][13] shows the morphing design.



Figure 2: The expandable wing changes its aspect ratio. (a) shows the wing in its expanded state and (b) shows the wing in folded state. The aspect ratio changes from 4.7 to 8.5 in two seconds which decreases drag significantly.

Chord changes alter the leading and trailing edges [11][22]. Chord changes are used to improve performance of the aircraft. The USSR designed the Bakshaev LIG-7 (shown in Figure 1) in 1937 with the first chord changes [2][11]. The wing had six chord-wise overlapping sections that was manually controlled from the cockpit. The mechanism used tensioned steel wire to extend and retract the wing. The retractable sections had an area change of 44% [2][11]. Figure 3 [11] shows the Bakshaev LIG-7

design.

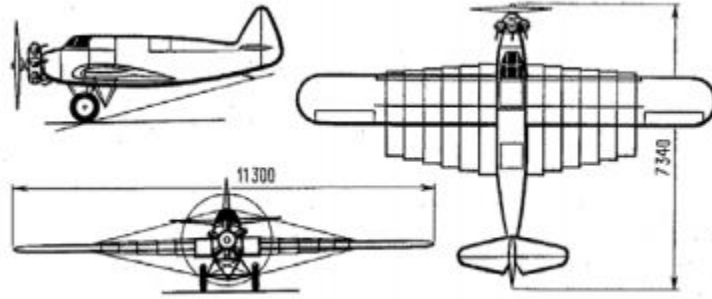


Figure 3: USSR designed the first aircraft with changing wing chords. The design used six chord-wise overlapping sections that were manually controlled from the cockpit.

In today's research, chord changes are mainly used in rotary because of the complexity. Fixed wings have fuel tanks, multiple spars, and other components that add complexity and aerodynamic loads. Rotary wings only have a single D-spar and honeycomb filler [22].

2.3.2 Airfoil Adjustment

Adjusting the airfoil involves changing the camber and thickness [2][14][15][16][17]. Camber variation is more common than thickness changes. Camber variation is found on fixed wing and rotary while thickness changes are mainly found in fixed wing.

The camber is the curvature or shape of the airfoil. Camber control involves changing the airfoil shape by means of actuators [2][14]. Actuators change the shape through the trailing and leading edge or changing the whole wing surface.

The first camber variation was the Parker Camber Variation Wing [15]. Changing the airfoil increased the lift-to-drag ratio. Figure 4 [15] shows the rib blueprint of the Parker Camber Variation wing.

The most common camber variation is the conventional control surface [2]. Conventional control surface deflects the leading and trailing edge. However, the trailing

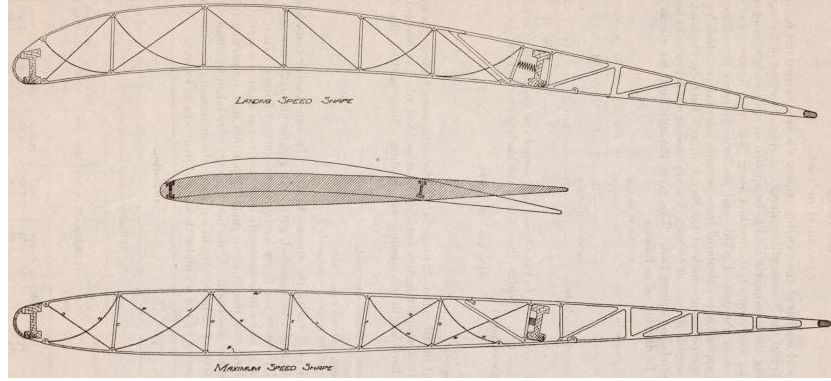


Figure 4: The first camber variation wing was the Parker Camber Variation Wing. The figure shows the ribs of the wing and where the deflection points change the camber shape.

edge is more customarily deflected. The surface area that is deflected increases its angle of attack and lift [2].

An example of thickness changing is Gano and Renaud's work [16]. They changed the airfoil thickness on a UAV called the variform wing. The variform wing had a fuel tank inside the wing. Figure 5 [17] shows the variform wing design.

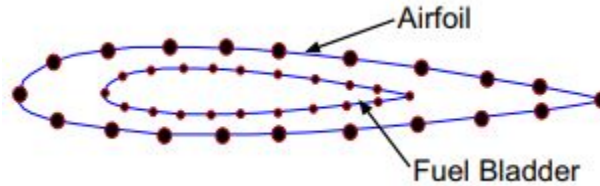


Figure 5: Gano and Renaud designed the variform wing. The wing has a tank fuel embedded inside. As the fuel depletes, the airfoil decreases.

As the fuel depleted, the airfoil thickness would decrease. Therefore, decreasing the airfoil thickness also decreases drag and increases endurance and range [17].

2.3.3 Out-of-Plane Transformation

Out-of-plane transformations involve twisting, dihedral/gull, and span-wise bending [18][19][20][21][22][23][24]. Transformations can involve all three parameters or work individually.

Twisting the wing is used to enhance control or performance of an aircraft. During the twisting, the angle of attack is modified and the lift-to-drag ratio increases [18][19][20]. Twisting provides a more powerful roll control that allows for quick maneuvers [18][19]. Rockwell International created the Active Flexible Wing program [21][34]. The program focused on using wing flexibility to reduce load and prevent aileron reversal. The wing allowed the aircraft to perform past the dynamic pressure of aileron reversal [21][34]. Figure 6 [34] shows the schematic of the Active Flexible Wing.

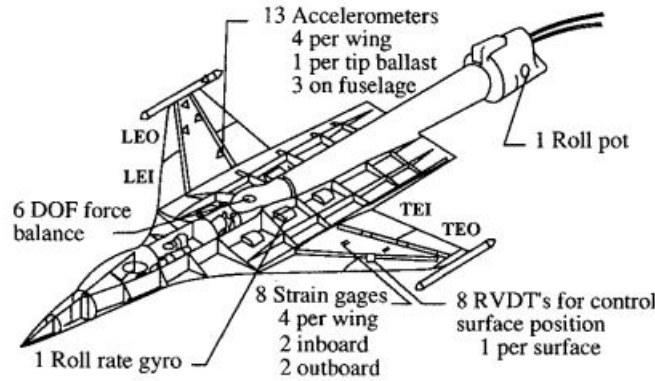


Figure 6: Rockwell International created the Active Flexible Wing that used wing flexibility to twist the wing. The wing reduced load and prevent aileron reversal.

Dihedral/gull wings improve the performance and control of an aircraft [22][23]. Dihedral wings have the ability to control the span and replace control surfaces. The transformations also improves the flight characteristics by decreasing drag and increasing stall [22][23]. Overall, dihedral wings improve the agility of the aircraft. For example, Lockheed-Martin created the Z-wing morphing design using folding wing in addition to span and sweep changes [22][23]. The Z-wing has two missions. One part of the mission is to perform long-range flight and do reconnaissances which require endurance and range. The second part of the mission is to perform high speed dash and attack [22][23]. Figure 7 [22] shows the Z-wing design.

Span-wise bending is used to improve the performance of an aircraft. Span-wise



Figure 7: Lockheed-Martin developed Z-wing morphing. The aircraft has the ability to fold its wings toward the center to change the aircraft from a long-range flight to high speed dash and kill and back.

bending was inspired by the hyper elliptic cambered span (HECS) concept from NASA researchers [22]. Bending is induced through actuators along the span-wise. An example of span-wise bending is the pitching-rolling plate [24]. The pitching-rolling plate uses span-wise and chordwise twisting to get the best performance of thrust production while maintaining propulsive efficiency [24]. Figure 8 [24] shows the bending of the pitching-rolling plates.

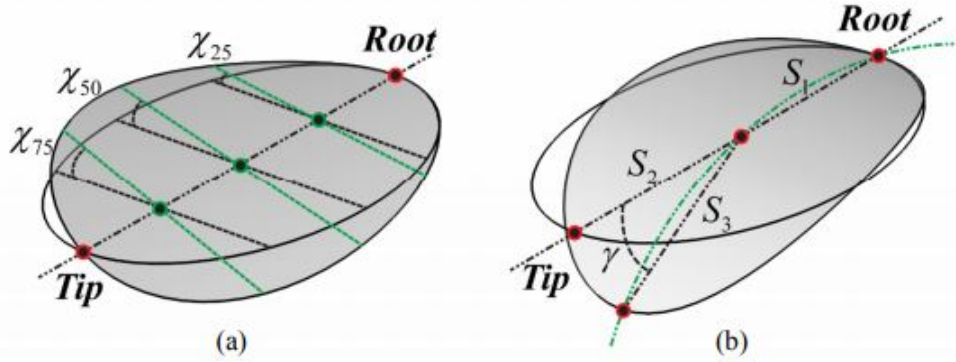


Figure 8: The pitching-rolling plates use span-wise and chordwise bending. The bending increases thrust production while maintaining propulsive efficiency.

2.4 Camber Morphing Wings

As discussed earlier, camber morphing involves changing the camber shape by deflecting the leading or trailing edge. Camber morphing wings use different structures,

skin and/or actuators [35]. The structure of the wing determines the type of actuators used. There are actuators are each segment of the wing to perform deflection in that area [35]. If the segment is too light, there will be structural dynamic issues. If the segment is too heavy, the wing needs larger actuators [35].

An example of an actuator material is the micro fiber composite (MFC), a piezo-ceramic composite actuator. MFC allows the structure of the aircraft to be flexible and obtain a high actuation authority [36][37][38]. When pressure is applied to the material, it generates a voltage which in turn changes the material shape [36][37][38]. It is a lightweight component that requires little power consumption due to its low current drain but requires a high voltage input [36][37][38]. The combination of the electrical and mechanical system allows the wing to change shape.

Because the camber changes, the skin needs to be flexible but have the ability to withstand different loads [39]. There are different camber morphing wings that have active or passive skin. Active morphing skin has the ability to change the airfoil chord and camber by itself [39]. Passive skin is morphed by the wing structure and actuators [39]. Active morphing skin is still in its preliminary stages of research so most camber morphing wings use actuators.

2.4.1 Variable Wing Camber Development

Variable wing camber technology has been developing since the 1980s. In the 1980s, the U.S. Air Force added the Mission Adaptive Wing to the F-111A [32][40][41][42]. The wing design changed the camber by separating the leading and trailing edge. The wing optimized cruise and maneuver conditions by providing variable camber, roll control, and reducing loads [32][40][41]. In the 1990's the Defense Advanced Research Project Agency (DARPA) Smart Wing Project created a wing that had variable wing twist along the trailing edge [32][40][41]. The Smart Wing had the ability to deflect

± 25 degrees. In most recent work, Flex Sys created the Mission Adaptive Compliant Wing. The wing used a stretchable skin with a smooth, variable trailing edge to improve high altitude endurance [32][40][41].

2.4.2 Variable Camber Compliant Wing

The Air Force Research Lab (AFRL) started their own work in variable wing camber technology. AFRL started developing the variable camber compliant wing (VCCW) in 2013. The wing's purpose was to actively re-contour the airfoil to optimize geometric shapes based off the flight states of altitude, airspeed and lift-to-drag ratio [32][40][41]. The following sections will discuss the different wing designs and testing procedures for the VCCW.

2.4.2.1 2015 Wing Design and Testing

The wing had a single, non-stretchable composite skin and a single actuation for the leading and trailing edge deflection [32][40][41]. Because the wing had a seamless skin (no gaps or holes), there was no separated flow or parasitic drag [32][40][41]. Seamless skin increased the range and endurance, allowed for surface control, and reduced power and noise [32][40][41][42]. Control surface gaps and edges create flap side edge noise which is a large contributor to the overall air frame noise. The seamless skin decreased the additional noise by eliminating gaps and holes [32][40][41][42]. The wing underwent testing to demonstrate its capabilities.

In 2015, AFRL tested the VCCW in AFRL's Vertical Wing Tunnel at Wright-Patterson Air Force Base [40][41]. The purpose of the test was to observe the prototype during low speed conditions [40][41]. The objective of the test was to achieve 6% camber change [40][41]. The test had uniform and nonuniform variation.

The prototype underwent two testing: benchtop and wind tunnel testing [40][41].

The benchtop model tested the aerodynamic load of a one foot span version of the wing [40][41]. The test refined the wing design for aerodynamic load, provided flow visualization (at 50 knots), developed fabrication methods, and measured the wing shape [40][41].

The vertical wind tunnel test used the full size wing model (six feet span by 2 feet chord) [40][41][43]. The wing was designed to change maximum section camber [43]. Individual ribs in the wing structure controlled the section profile shape [43]. During testing, the section profile camber changed while the maximum camber location remained constant by vertically deflecting the leading and trailing edges equal distances respect to the spar [43]. The test showed the wing was capable of a nearly 6% maximum camber change and was able to withstand flow speeds up to 50 knots [43]. Figure 9 [32] shows the prototype deflections.

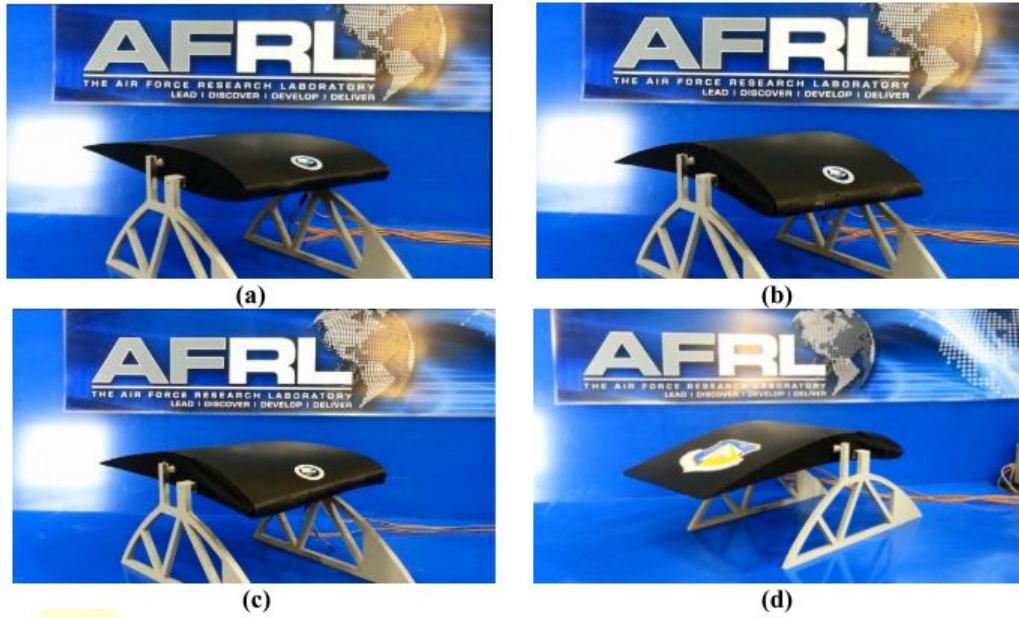


Figure 9: AFRL's VCCW changes its shape by actuating the leading and trailing edge. a) no deformations b) 6% camber deformed c) twisted d) rear view of (b)

2.4.2.2 2018 Wing Design and Test

Over the development years, AFRL collaborated with the Utah State University (USU) Aero Lab and the Autonomous and Navigation Technology (ANT) Center at Air Force Institute of Technology (AFIT). The VCCW changed its structure, actuation system, and skin. The wing had actuators at each of the six ribs to control the inner, middle, and outer trailing edges [30][32]. The skin was a combination of thin carbon fiber sheets covered by nylon [32]. The wing underwent flight testing to demonstrate its capabilities.

AFRL designed and built the wing while USU Aero Lab developed the lift coefficient calculations to optimize geometry shaping. AFIT performed system integration for controls and executed the flight testing.

The 2018 VCCW design underwent flight testing at Camp Atterbury, IN. However, the test revealed issues with the wing design and controller. The wing surface expanded after take off around 20 m/s [32]. Wind speeds were high for that day and the spandex skin created a ballooning effect [32]. Figure 10 [32] shows the wing expansion during the flight test.



(a)



(b)

Figure 10: There were flight complications from the wing surface. Wing comparison before and after take off (a) before with no expansion (b) after take off with ballooning effect

In addition to the ballooning, the ground controller lost communication with the wing and there was no signal to the wing actuators during flight [32]. Surface control was lost due to the wing expansion and no actuator movement. Therefore, there was zero aileron control of the aircraft, and rudder/elevator control was insufficient to sustain flight.

These two issues helped improve the wing for the current design. AFRL developed a new wing with a different skin. There were modifications to the the control code and pre-flight procedures to prevent loss of control [32].

2.5 Background Summary

Chapter II discussed the background of the UAVs and morphing wing. Morphing wings are found on all different types of aircraft: advanced fighters, transporters, helicopters, and UAVs. UAVs can fly dangerous flights and missions that are too risky for human operators. Wing morphing improves the performance of an aircraft and has the ability to fly multiple missions in one flight. Morphing wing technology involves planform alternation, airfoil adjustment and out-of-plane transformation.

Because this research focuses on camber variation, the chapter closed with the technology development of wing camber variation. The most recent AFRL morphing wing work is the VCCW on a UAV. The wing deflects the trailing edge for surface control (primary roll control). AFRL, USU Aero Lab, and AFIT worked on the wing over the course of this thesis and contributed to camber variation work. The next few chapters discuss the development of the VCCW research.

III. Methodology

Methodology discusses technical background and various tests performed for this thesis. This chapter begins by describing, in general, an aircraft's flight dynamics and stability. Then, the chapter provides an overview of the variable camber compliant wing (VCCW). The chapter then discusses the bi-filar pendulum procedure that measures the moment of inertia (MOI) for the base wing and VCCW. There are two sections for wing testing, which demonstrate the capabilities of the wing: high speed static wind testing and flight testing. The final section of the chapter introduces the VCCW simulation tool.

3.1 Aircraft Dynamics

This thesis involves analysis of flight test data. Analysis requires the understanding of aircraft dynamics. From a high level explanation, aircraft dynamics are described by their components and stability. Aircraft dynamic components describe the movement of the vehicle and stability is necessary for a successful flight.

There are three axes in aircraft dynamics: roll (x), pitch (y), and yaw (z). Each axis has its own forces, moments, and velocity components. The dynamics are described by angular rates, velocity, forces, moments, and inertia. A simplistic explanation is shown in Figure 11 and cataloged in Table 1. In general, there are intermediate frames in an Euler angle sequence [44].

An aircraft is controlled by four inputs: throttle, ailerons, elevator, and rudder. Throttle controls the thrust of the aircraft. Aileron, elevator, and rudder impart moments aligned with the roll, pitch and yaw axes, respectively.

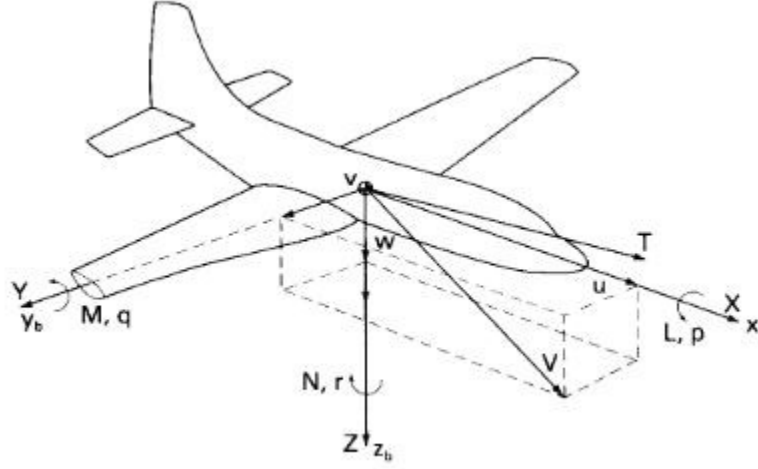


Figure 11: Aircraft dynamics components are defined by forces, moments and velocity. There are three axes that have their each dynamic component described in Table 1.

Table 1: Aircraft has forces, moments and velocity components in three axes

	Roll Axis (x_b)	Pitch Axis (y_b)	Yaw Axis (z_b)
Angular rates	p	q	r
Velocity components	u	v	w
Aerodynamic force components	X	Y	Z
Aerodynamic moment components	L	M	N
Moment of inertia about each axis	I_x	I_y	I_z
Products of inertia	I_{yz}	I_{xz}	I_{xy}

3.1.1 Stability

According to [45], there are two conditions for an aircraft to have a successful flight: 1) achieve equilibrium flight and 2) have the capability to perform flight maneuvers [45]. An equilibrium state is when an object returns to its trim condition over time [45]. When an aircraft's motion is disturbed from trim, the aircraft can become unstable if not adequately configured. An aircraft must have the ability to fly at a broad range of velocities and altitudes in a stable manner. A working control system will provide the ability to perform flight maneuvers. The design and performance of control systems is vital for flight [45].

Stability of an aircraft is defined around trim conditions. If an aircraft is stable (at the trim condition), the resultant force and resultant moment about the center of gravity is equal to zero [45]. Stability is described by static and dynamic stability. Static stability is when an object's initial tendency is to return to the equilibrium state after a disturbance [45]. Dynamic stability is when an object dampens its disturbance oscillation to restore moments and return to its equilibrium state [45]. An aircraft must be statically stable in order to be dynamically stable [45].

Stability of an aircraft is described through longitudinal and lateral aircraft dynamics. Longitudinal aircraft dynamics are those in the plane defined by the x and z axes, and include the thrust, drag, and lift force, and the moments in pitch [45]. Lateral aircraft dynamics are those in the plane defined by the x and y body axes, and include the side force and the moments in roll and yaw [45].

3.1.1.1 Longitudinal Motion

When an aircraft is disturbed from longitudinal equilibrium, the flight condition is described by two modes: phugoid and short period. Figure 12 [45] shows the aircraft motion in the longitudinal modes.

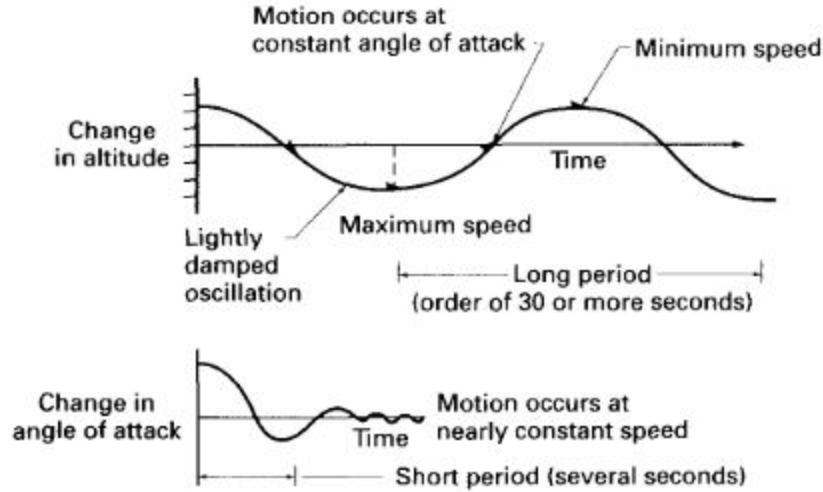


Figure 12: Phugoid and short period aircraft motion. Phugoid has a longer period and therefore, takes longer to stabilize. Short period stabilizes within a shorter period.

The phugoid mode has a long period with a low frequency and is lightly damped. The short period mode has a high frequency and is heavily damped resulting in a shorter period. The aircraft takes longer to stabilize in presence of the phugoid mode [45].

3.1.1.2 Lateral Motion

When an aircraft is disturbed from lateral stability, the aircraft is characterized by three modes: roll, spiral, and dutch roll. Figure 13 [45] shows the aircraft's motion in the different lateral modes.

The spiral mode has a slowly convergent or divergent motion. An unstable spiral slowly increases the aircraft bank angle, resulting in an increasing side-slip angle and the aircraft's path becomes a tighter spiral. The rolling mode is a highly convergent motion. Because the rolling mode is usually highly damped, the aircraft will reach a steady state. The Dutch roll mode has a low frequency resulting in a lightly damped oscillatory motion and is a combination of roll, slide-slip and yaw all at once [45].

Stability of the aircraft is essential with new designs. Without stability and con-

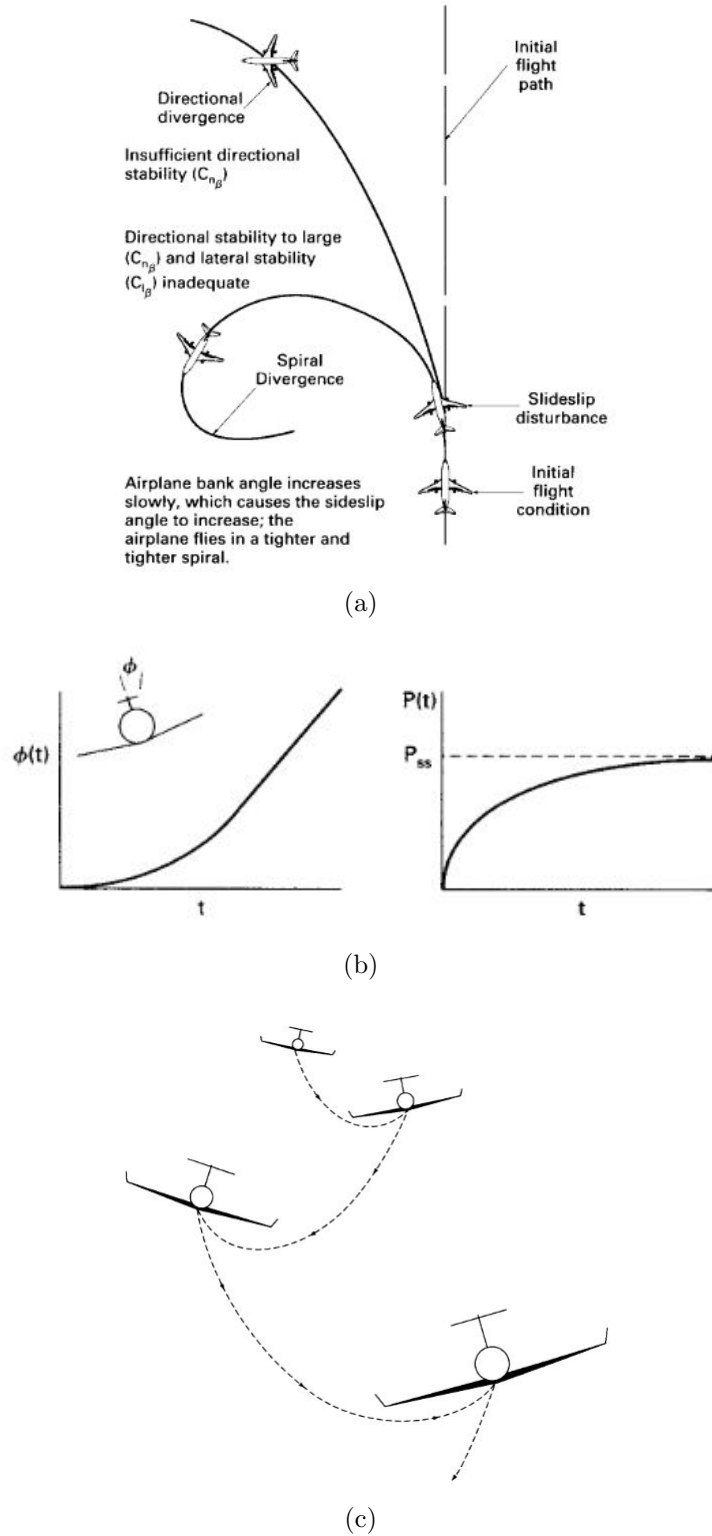


Figure 13: When aircraft become unstable, they are described in three motions: (a) spiral, (b) roll, and (c) dutch roll. Over time, spiral and dutch roll become more unstable. Roll reaches stability over time.

trol, the aircraft will not fly successfully. For this thesis, the wing is a new design to control flight maneuvers. Static and dynamic stability are necessary to test the wing control. Once wing control is established, it is vital the controls are capable of maintaining stability. Without stability, the aircraft could sustain damages, resulting in loss time and future efforts on the project.

3.2 Variable Camber Compliant Wing Overview

The variable camber compliant wing (VCCW) is an original design from the Air Force Research Lab (AFRL). The VCCW is described by three components: the design, controller, and flight modes. The design describes the structure of the aircraft and how it will be flown. The controller explains the different parts used to control the wing deflection. The wing is capable of changing deflection in four different modes. As a conjoined project, each group has their own roles. AFRL designs and builds the wing. Utah State University (USU) Aero Lab develops the controller algorithms for all flight modes. Air Force Institute of Technology (AFIT) integrates the controller to the communicate with the ground station and wing.

3.2.1 Design

The fuselage is a big stick XL air frame that has the ability to interchange between the base wing and VCCW. The VCCW has a single, non-stretch, seamless skin. The wing is divided into the left and right side with three flexible ribs (inner, middle, and outer) in each wing. In the wing, the base of the wing structure is a 3D printed carbon fiber spar that are attached to the ribs. Each rib has individual actuators that deflect the wing surface.

The VCCW has a unique design with a specific controller for the wing. The aircraft uses a Pixhawk and Arduio to communicate with the ground station and

remote controller (RC). The Pixhawk is an autopilot hardware [46] that tracks aircraft movement and parameters while in flight. The hardware senses and records flight data from a three axis accelerometer, three axis gyroscope, three axis magnetometer, a digital airspeed sensor, a GPS unit, a barometer, and servo commands (throttle, aileron, elevator, and rudder deflections) [46]. The Pixhawk also provides real-time data streaming down to the ground station. While the Pixhawk is running, the Arduio calculates the wing deflection. The next section describes the Arduio incorporation with the wing.

3.2.2 Controller

The wing controller involves the RC input, sensor, receiver, Pixhawk, Arduio, and the servos. All of the components communicate to convert and calculate the wing deflections.

The RC input goes directly to the receiver then to the Pixhawk. The RC input is in pulse width modulation (PWM). The Pixhawk receives the RC input and simultaneously generates the aircraft states from the sensor. The Pixhawk then sends the RC input and aircraft states to the Arduio and recording log. The Arduio takes the RC input and flight states to calculate the lift coefficient (1) described by:

$$C_L = \frac{W \cos(\gamma)}{1/2 \rho V^2 S \cos(\phi)}, \quad (1)$$

where C_L is the lift coefficient, W is the weight of the aircraft, γ is the climb angle, ρ is the air density, V is the airspeed, S is the wing area, and ϕ is the bank angle. The lift coefficient is passed to the control law, developed by USU Aero Lab, to calculate the deflection angle (in degrees) of each rib. The Arduio calculates the corresponding PWM value to move the deflecting angle in degrees. Then, the Arduio simultaneously sends the deflection (in PWM) to the servo and recording log. Finally,

the servo deflects wing surface accordingly. Figure 14 shows a flow diagram of the controller.

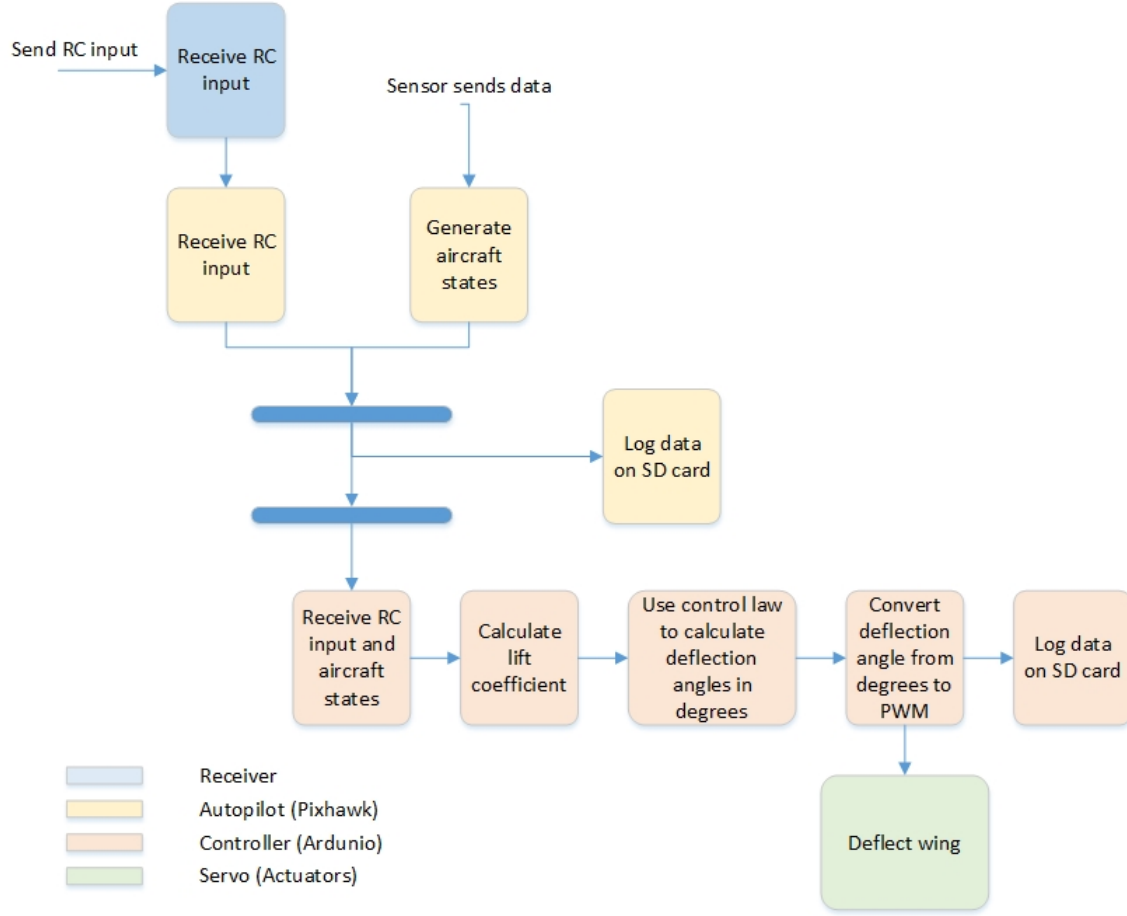


Figure 14: The diagram shows the flow of the wing controller. The wing controller involves the receiver, autopilot, controller, and servo. The controller is capable of computing the lift coefficient and deflection angle using the control law.

3.2.2.1 Control Law

USU Aero Lab derived equations from the lifting theory combined with numerical optimization [47] to create control laws for the VCCW. The angle of deflection for each rib is described by two types of equations: anti-symmetric and symmetric, for roll control and flap levels, respectively. USU Aero Lab developed the roll and yaw control using the equations. The roll and yaw control laws use six polynomial equations to

calculate the deflection at that surface: anti-symmetrical inner, middle, and outer and symmetrical inner, middle, and outer [47].

The roll control law is described in Appendix A in (22)-(24). The roll control law needs the lift coefficient (C_L) and RC aileron input (\bar{p}). However, the equations have bounds for all of the variables because at high levels, the solution can become unrealistic. The lift coefficient is bounded from -1.2 to +1.2 while the RC aileron input is bounded from -0.24 to +0.24.

The yaw control law is described in Appendix B in (25)-(27). The yaw control law needs the lift coefficient (C_L), RC aileron input (\bar{p}), and yawing moment coefficient (C_n). Just like the restrictions of the roll control law, the yaw control law bounds its variables as well. The lift coefficient is bounded from 0 to +1.2, the RC aileron input is bounded from -0.05 to +0.05, and the yaw control law is bounded from -0.005 to +0.005.

3.2.3 Flight Modes

The wing design has four different modes. The surface control of the wing replaces the ailerons and flaps. Mode 1 has full trailing edge deflection. The wing morphs the trailing edge as one big aileron with flap capabilities and there is no variation span wise. Mode 2 has anti-symmetric trailing edge deflection. The wing has flap capabilities and spanwise variation. There is no symmetry deflection in this mode. The roll capabilities are in Mode 3. Mode 3 has anti-symmetric and symmetric trailing edge deflection. The wing takes in the RC input, roll attitude, airspeed, and climb rate to calculate the optimal lift coefficient then morphs the wing appropriately. Mode 4 fixes the rudder at a neutral position and allows the wing to morph and impart yaw control in addition to controlling roll and lift. The yaw control depends on Mode 3 because it has the ability for anti-symmetric and symmetric trailing edges. Since

yaw control isn't normally on the wing, the aircraft relies on the Mode 3 symmetric distribution of lift.

3.3 Bi-filar Pendulum

Aircraft parameters and measurements are important to properly calculate flight states. The aircraft parameters also help explain why the aircraft reacts a certain way. Because this aircraft is one of a kind, the moment of inertia (MOI) is unknown. MOI is needed to understand and calculate some of the flight states. A cost and time efficient method to measure MOI is the bi-filar pendulum. This thesis used the bi-filar pendulum to measure the MOI for the VCCW project.

The purpose of this test was to measure the MOI on an aircraft, about all three axes. Testing involved suspending the aircraft then rotating and recording the time the aircraft took for one oscillation period as shown in Figure 15 [48].

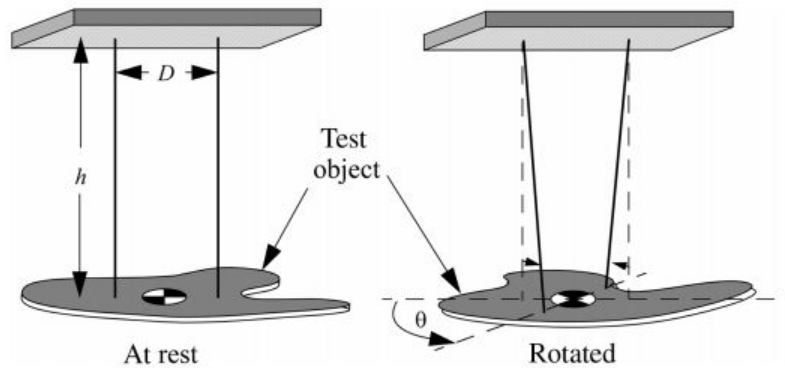


Figure 15: Bi-filar pendulums were used to measure the MOI for complex bodies. The test suspended the object and measured the time the object takes to perform one period.

3.3.1 Procedure

A bi-filar pendulum was composed of two parallel, stretchable filars that were suspended at the same height. The aircraft was leveled and evenly mounted at the

end of the filars. Once mounted, the aircraft was rotated clockwise to a constant angle. Time was recorded while the aircraft was released from its rotated position. The average time for one oscillation served as the time period. There are three trials for each axes (roll, pitch, and yaw).

In order to calculate the MOI, the following measurements were needed:

- Mass (kg) - m
- Distance between filars (m) - d
- Length of filars (m) - l
- Time (s) - T

The MOI calculation is described as

$$I = \frac{mgd^2}{4lw^2} = \frac{mgd^2}{4l\left(\frac{2\pi}{T}\right)^2}, \quad (2)$$

where g is gravity (m/s^2).

3.3.2 Trial Test Improvements

There were two trial tests completed to improve the testing procedure. The tests were completed on a Sig Rascal model and the base wing of the Big Stick XL air frame. The trial tests helped to identify multiple sources of error in the methodology: inaccurate hand timing and excessive drag. The trial test used hand timing methods, which resulted in inaccurate recordings of period lengths. The aircraft's rotation in the bi-filar pendulum was initially set to 45° . Because of the large rotation, there was noticeable drag from the tail and landing gear as the vehicle swung back and forth.

Different procedures were developed to eliminate the known sources of error. The aircraft rotation was decreased to 15° to limit the amount of drag from the tail and

landing gear. Instead of hand timing the oscillation period, the Vicon chamber was used to record the time.

The Vicon chamber recorded the oscillation period by tracking the motion of the aircraft in all axes. The chamber used eight cameras to track the movement of markers on an object for a 360° view. The cameras had tracking abilities in the translational and rotational plane. For the bi-filar testing, the z rotation recorded the aircraft's period and showed exactly when the period began and ended. Figure 16 shows an example of the collected data from the Vicon chamber. Figure 16(b) has trimmed data to find the exact start and end of the period by finding the maximum peak of the data. Vicon chamber measurements provided a more accurate timing method than hand-timed data.

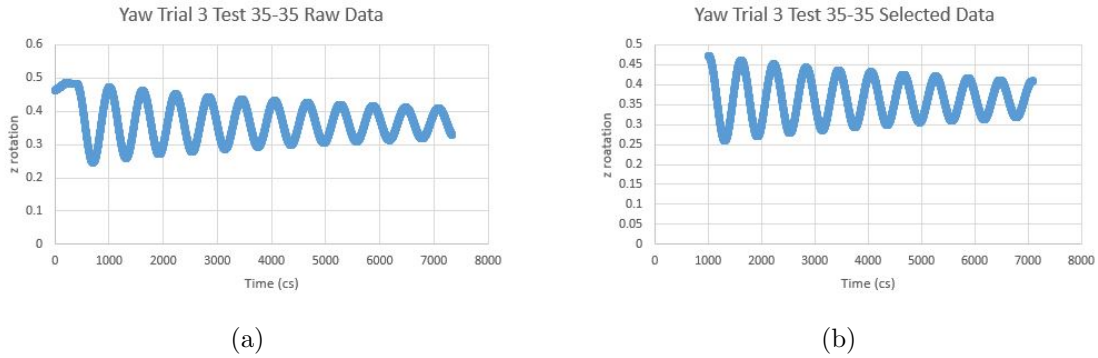


Figure 16: Vicon recorded data of XY axes test of time vs z rotation of aircraft. (a) shows the raw recording. In order to find the most accurate start and end time of the period, the data is trimmed in (b).

The test and results of the bi-filar pendulum test are discussed in Section 4.1.

3.4 High Speed Static Wind Test

There was a high speed static wind test for the 2019 wing design. The test was an alternative to using a wind tunnel. The wing was mounted in the back of a truck without any obstruction. Wind testing involved driving the truck at various speeds

to simulate the wing in flight. The wing underwent a series of tests to check the load factor, drag, and power.

Utah State University (USU) Aero Lab derived the VCCW performance based on the lifting theory and numerical optimization [47]. Figure 17 shows the drag and power at different air speeds. Trends between the drag and power show the potential cruise speed. USU Aero Lab predicted that the VCCW would have a cruise speed of around 45-48 mph.

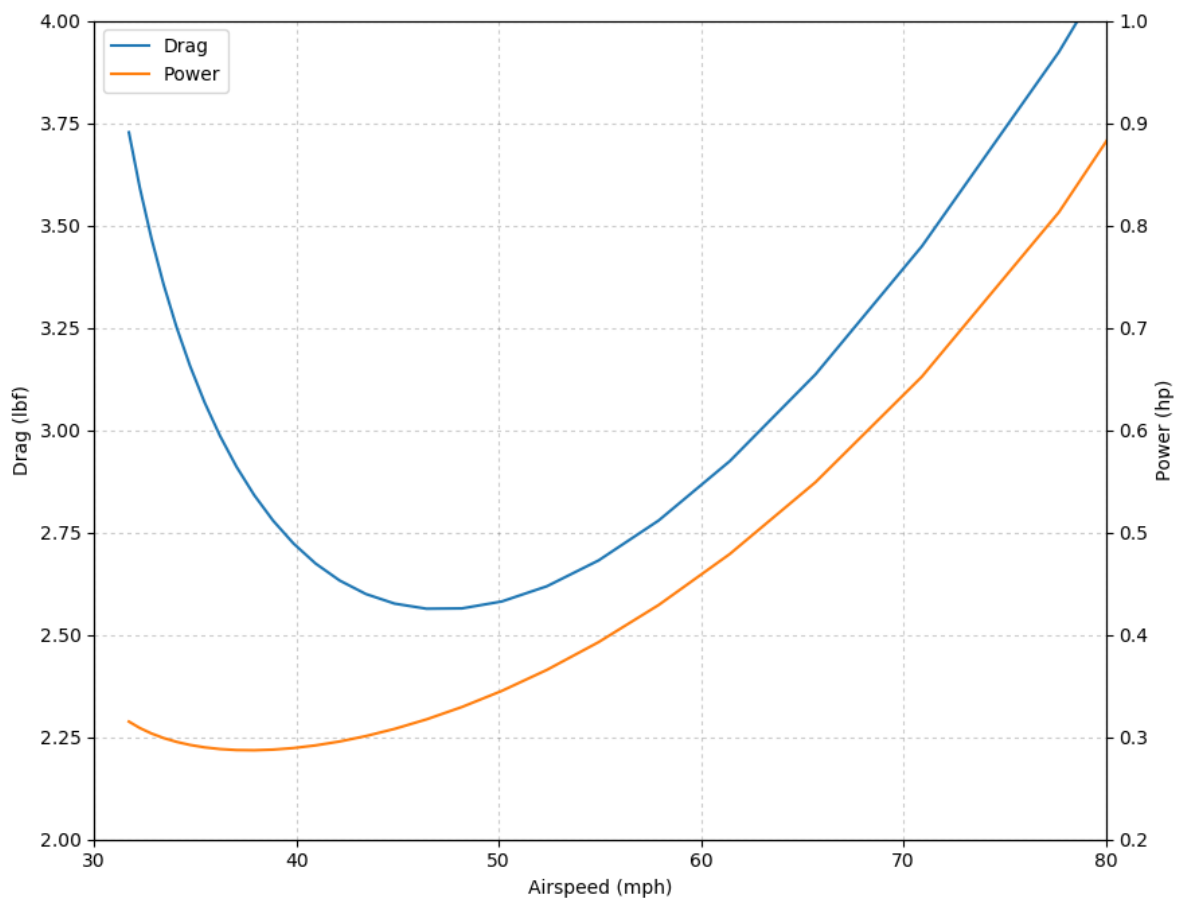


Figure 17: USU Aero Lab created a model to describe the wing's performance. The model shows the drag and power of aircraft at different air speeds. The minimum drag occurs at 45-48 mph cruise speed.

The wind test evaluated the load factor versus the airspeed with various angles of attack and flap deflections. The calculated load factor is shown in Figure 18.

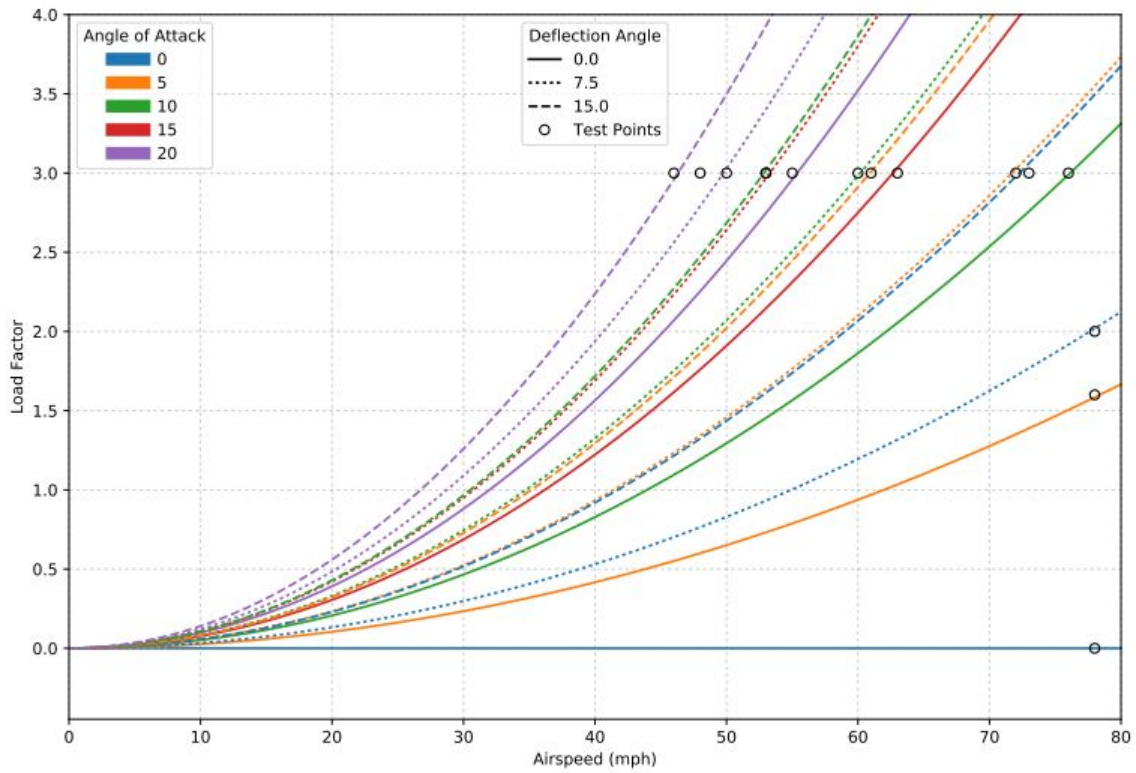


Figure 18: The figure shows USU Aero Lab's model to predict the load factor on the wing. The model is described at five different angle of attacks at various air speeds. The deflection angle changes according to the angle of attack. The suggested test points for the 2019 wind test are defined along the load factor line of 3.0, in black dots.

USU Aero Lab created a chart of the test points based off of Figure 18. The test point chart included optional tests with load factors of 4. The test points are shown in Figure 19.

Load Factor	angle of attack (deg)	Deflection angle (deg)	Airspeed (mph) LF=1	Airspeed (mph) LF=2	Test Pass Airspeed (mph)
0	0	0	-	-	80 or Max
1	0	7.5	55	-	55
2.2	0	7.5	55	78	80 or Max
3	0	15	42	59	73
1.6	5	0	62	-	80 or Max
3	5	7.5	42	58	72
3	5	15	35	50	61
3	10	0	44	62	76
3	10	7.5	35	49	60
3	10	15	31	44	53
3	15	0	37	52	63
3	15	7.5	31	44	53
3	15	15	26?	37?	48?
3	20	0	32	45	55
3	20	7.5	29	41	50
3	20	15	26	37	46
Optional					
4	5	15			70
4	10	7.5			69
4	10	15			61
4	15	0			73
4	15	7.5			62
4	15	15			54?
4	20	0			64
4	20	7.5			57
4	20	15			53

Figure 19: USU Aero Lab created test points to determine the amount of load the VCCW could withstand. The test points changed the angle of attack, deflection angle, and airspeed.

Using the test points, the test showed what load factor the wing could endure. The results are discussed in Section 4.2.

3.5 Flight Test

After conducting the high speed static wind test, actual flight testing confirmed the capabilities of the VCCW. The flight test team encompassed individuals from AFIT, AFRL and USU Aero Lab. Flight testing required objectives to drive the types of test points. The objectives demonstrated the capabilities of the aircraft and provided flight data for analysis.

Prior to flight testing, the flight test team underwent a technical and safety review board (TRB/SRB). The board discussed the test objectives, safety hazards, and mishap responsibilities. The team described all of the hardware and software used for the VCCW and the manufacturing parameters. Each component was analyzed for mishap mitigation to ensure a successful flight testing. Based on the capabilities of the wing, the team also determined a safety limit on flight conditions: altitude, visual line of sight, and wind speed.

There were three major test hazards: loss of wing control authority due to mechanical failure, controller failure, and servo failure. The review board required analysis of the test hazards. The team analyzed each hazard's cause, effect, minimizing procedures, and corrective actions. After thorough evaluation and precaution measures, all three hazards were considered catastrophic to the project but unlikely to occur during the test. The precaution measures made the hazards unlikely to occur but losing wing control could cause damage to personnel, buildings and/or the environment.

3.5.1 Flight Test Objectives

Each flight had an objective to demonstrate the capabilities of the aircraft. Flight testing involved the base wing and the VCCW. The base wing provided checkout and data collection on the aircraft to be applied to the VCCW.

3.5.1.1 Base Wing: July 2019

The first flight testing was scheduled for the end of July 2019 for the base wing only. Base wing testing provided a full run through of flight procedures and testing in preparation for the VCCW. There were two objectives:

1. Controller checkout and verification
2. Control system identification

Objective 1

Objective 1 was to ensure the Arduino control was working properly. The controller received the telemetry from the Pixhawk (autopilot) and the RC input from the ground controller. Then, the controller calculated the outputs and recorded real time data on an SD card. During this test, the controller was disconnected from the actuators. There were success and evaluation criteria.

Success Criteria:

1. Desired data saved onto the autopilot SD card
2. Desired data saved onto the Arduino SD card
3. Potential code or hardware failures identified

Evaluation Criteria:

1. Power loss, identified by creation of multiple logs on Arduino.
2. Code failure, identified by lack of serial output on ground after flight.

The expected result was to have the Arduino run as planned or have minor controller errors. There were no expected vehicle operation issues.

Objective 2

Objective 2 was to collect data to build an analytical model of the aircraft performance. The data collection was required for control development of the VCCW. There were four success criteria and the evaluation criteria was satisfactory if the success criteria was met.

Success Criteria:

1. Desired data saved onto the autopilot SD card
2. Desired data saved onto the Arduio SD card
3. Battery consumption noted to calculate maximum flight times
4. Data collected for each point on test matrix (minimum criteria is highest priority points are collected)

The expected result was to collect sufficient data for analysis. The objectives were met through different test points. The test cards had all of the test points to observe the aircraft controls. Some of the test points were pulse inputs for roll, pitch and yaw in both directions. There were turns with aileron or rudder control only as well as coordinated turns. Table 2 shows the test card for the base wing flight test.

Table 2: The table shows all the test points for the base wing flight testing. The same maneuvers were performed with different rudder mixing, deflection level, and speed to provide a vast data collection on the flight states.

Test Point	Description	Rudder Mix	Deflection Level	Speed
1	Roll Doublet	Low	Half	Low
2	Roll Doublet	Low	Half	Med
3	Roll Doublet	Low	Half	High
4	Roll Doublet	None	Half	Low
5	Roll Doublet	None	Half	Med
6	Roll Doublet	None	Half	High
7	Roll Doublet	None	Full	Low
8	Roll Doublet	None	Full	Med
9	Roll Doublet	None	Full	High
10	Yaw Doublet	None	Half	Low
11	Yaw Doublet	None	Half	Med
12	Yaw Doublet	None	Half	High
13	Yaw Doublet	None	Full	Low
14	Yaw Doublet	None	Full	Med
15	Yaw Doublet	None	Full	High
16	Aileron Turn	None	~20 deg	Low
17	Aileron Turn	None	~20 deg	Med
18	Aileron Turn	None	~20 deg	High
19	Rudder Turn	None	Half	Low
20	Rudder Turn	None	Half	Med
21	Rudder Turn	None	Half	High
22	Coord. Turn	Low	~20 deg	Low
23	Coord. Turn	Low	~20 deg	Med
24	Coord. Turn	Low	~20 deg	High
25	Pitch Doublet	None	Half	Low
26	Pitch Doublet	None	Half	Med
27	Pitch Doublet	None	Half	High
28	Pitch Att. Hold	None	15-20 deg climb	Low
29	Pitch Att. Hold	None	15-20 deg climb	Med
30	Pitch Att. Hold	None	15-20 deg climb	High
31	Step Aileron opposing rudder	None	Half	Low
32	Step Aileron opposing rudder	None	Half	Med
33	Step Aileron opposing rudder	None	Half	High
34	Step Aileron opposing rudder	None	Half	Low
35	Step Aileron opposing rudder	None	Half	Med
36	Step Aileron opposing rudder	None	Half	High

3.5.1.2 VCCW Modes 1-3: September 2019

The second flight test was the VCCW's first flight. Flight testing focused on the aircraft's performance in Modes 1-3. Like the base wing, the VCCW had objectives and criteria to meet to demonstrate the capabilities of the wing.

The VCCW had the ability to receive inputs from the remote controller and environment to calculate the most efficient lift coefficient. The autonomous system constantly calculated and updated the lift coefficient throughout the flight while morphing the wing to the appropriate surface deflection.

VCCW's first flight was scheduled for September 2019. Because the test was the wing's first flight, the aircraft had to be flown at Camp Atterbury, IN. The airfield was in an isolated area to accommodate potential mishaps and limit safety concerns. There were five objectives:

1. Mode 1 maiden flight
2. Mode 1 and 2 training and verification
3. Mode 3 maiden flight and tuning
4. Mode 3 training and verification
5. Mode 3 system ID

Objective 1

Objective 1 was to verify the VCCW design being controlled by the new controller design. There was also data collections to analyze for controller development. Because it was the maiden flight, the safety pilot trimmed the aircraft and performed a stall to understand the stall characteristics. There were seven success criteria and three evaluation criteria.

Success Criteria:

1. Vehicle flown and recovered without damage
2. Ability to maintain positive control during benign flights demonstrated in Mode 1
3. Desired data saved onto the autopilot SD card
4. Desired data saved onto the Arduio SD card
5. Video of wing recorded on cameras recovered
6. Video revealed any in flight abnormalities

Evaluation Criteria:

1. Safety pilot assessment of sufficient control authority (takeoff, fly, and recover)
2. Visual inspection and ground check for damage and abnormalities
3. Visual inspection of tail cameras for abnormalities

The expected results were to have the wing provide sufficient lift at cruise, Mode 1 had more sensitive controls, no structural failures, and the controller operated as expected.

Objective 2

Objective 2 was to verify the functionality of Mode 1 and 2. The flight test allowed for the safety pilot to have more flight time on Mode 1 and 2 to become more familiar with the controls. There were five success criteria and five evaluation criteria.

Success Criteria:

1. Vehicle flown and recovered without damage
2. Ability to maintain positive control during benign flights demonstrated in Mode 1 and 2

3. Refined estimate of max flight time
4. Desired data collection
5. Pilot has sufficient time in each mode

Evaluation Criteria:

1. Safety pilot assessment of sufficient control authority (takeoff, fly, and recover)
2. Visual inspection and ground check for damage and abnormalities
3. Visual inspection of tail cameras for abnormalities
4. Pilot self-assessment of aptitude in Mode 1 and 2
5. Tail video inspected for an wing abnormalities

The expected results were that the wing would provide sufficient lift at cruise and would stall similar to the base wing and Mode 1. Mode 1 would have had more sensitive controls and Mode 2 would have had sufficient amount of control authority. There should have been no structural failures and the controller should have operated as expected.

Objective 3

Objective 3 was to maiden Mode 3 and tune symmetric controller. The symmetric parameters were the lift coefficient moving average integration time and the symmetric control lift coefficient limit value. Takeoff and landing were to be accomplished in Mode 1 or 2. There were five success criteria and five evaluation criteria.

Success Criteria:

1. Vehicle flown and recovered without damage
2. Ability to maintain positive control during benign flights demonstrated in Mode

3. Refined estimate of max flight time
4. Desired data collection
5. Pilot has sufficient time in each mode

Evaluation Criteria:

1. Safety pilot assessment of sufficient control authority (takeoff, fly, and recover)
2. Visual inspection and ground check for damage and abnormalities
3. Visual inspection of tail cameras for abnormalities
4. Pilot self-assessment of aptitude in Mode 1 and 2
5. Tail video inspected for an wing abnormalities

The expected result was the lift coefficient limit decreased no more than 25% during controller tuning. The wing should have provided sufficient cruise and stalled similar to the base wing and Mode 1 stall. There should have been no structural failures and the controller should have operate as expected.

Objective 4

Objective 4 was to become more familiar controlling with Mode 3. The test provided verification of Mode 3's functionality. The test focused more on maneuvers and the capabilities of Mode 3 control. There were five success criteria and four evaluation criteria.

Success Criteria:

1. Vehicle flown and recovered without damage
2. Ability to maintain positive control during benign flights demonstrated in Mode 1 and 2

3. Refined estimate of max flight time in Mode 3
4. Desired data collection
5. Pilot has sufficient time in each mode

Evaluation Criteria:

1. Safety pilot assessment of sufficient control authority (takeoff, fly, and recover)
2. Visual inspection and ground check for damage and abnormalities
3. Visual inspection of tail cameras for abnormalities
4. Pilot self-assessment of aptitude in Mode 3

The expected result was that Mode 3 should have similar control authority to Mode 2. The wing should have provided sufficient cruise and stalled similar to the base wing, Mode 1, and Mode 2. There should have been no structural failures and the controller should have operated as expected.

Objective 5

Objective 5 was to collect data to enable building an analytical model of the aircraft performance. There were five success criteria and if the success criteria was met, the evaluation criteria was satisfactory.

Success Criteria:

1. Desired data saved onto the autopilot SD card
2. Desired data saved onto the Arduio SD card
3. Battery consumption noted to calculate max flight time
4. Data collection for each point on test matrix
5. Aircraft flying as expected based off previous objectives

The test cards for the VCCW (refer to Table 2) were to same as the base wing. The same test points were needed to complete flight analysis and compare the capability of the VCCW. The flight test focused on getting training on Modes 1-3 to demonstrate the wing's capabilities as well as prepare for flights on Mode 4.

3.5.1.3 VCCW Mode 4: October 2019

The last flight test focused on the VCCW's performance while in Mode 4. Testing had new objectives and criteria to demonstrate the capabilities of the wing. The test checked the performance on Mode 4 but relied on Mode 1 and 3 for safety controls.

Mode 4 flight testing was scheduled for October 2019. Because Mode 4 had new technology, there was a possible higher risk for mishap. Therefore, the wing had to be tested at Camp Atterbury, IN again. There were four objectives for this set of flight testing:

1. Warm-up and checkout
2. Mode 4 maiden flight and tuning
3. Mode 4 training and verification
4. Mode 4 system ID

Objective 1

Objective 1 was to perform checkouts with the new configurations and provide the safety pilot with sufficient flying time. The flight used all three modes to familiarize the safety pilot before the next objective. There were four success criteria and five evaluation criteria.

Success Criteria:

1. Vehicle flown and recovered without damage

2. Ability to maintain positive control during benign flights demonstrated in Mode 1 and 3
3. Desired data collection
4. Pilot has sufficient time in each mode

Evaluation Criteria:

1. Safety pilot assessment of sufficient control authority (takeoff, fly, and recover)
2. Visual inspection and ground check for damage and abnormalities
3. Visual inspection of tail cameras for abnormalities
4. Pilot self-assessment of aptitude in Mode 1 and 3
5. Tail video inspected for an wing abnormalities

The expected result of the flight was that there were no noticeable changes from the previous flight configuration. There should have been no structural failures and the controller should have operated as expected. The safety pilot should have felt comfortable moving to the next objective.

Objective 2

Objective 2 was to maiden the yaw controller (Mode 4). Mode 1 or 3 acted as the safety modes. The pilot attempted coordinate, aileron only, and rudder only turns. There were five success criteria and five evaluation criteria.

Success Criteria:

1. Wing controller tuned
2. Vehicle flown and recovered without damage

3. Ability to maintain positive control during benign flights demonstrated in Mode 4
4. Desired data collection
5. Pilot has sufficient time in each mode

Evaluation Criteria:

1. Safety pilot assessment of sufficient control authority (takeoff, fly, and recover)
2. Visual inspection and ground check for damage and abnormalities
3. Visual inspection of tail cameras for abnormalities
4. Pilot self-assessment of aptitude in Mode 1 and 3
5. Tail video inspected for an wing abnormalities

The expected result was that the wing controller tuning was similar to the starting tuning. The wing should have provided sufficient lift. There should have been no structural failures and the controller operated as expected.

Objective 3

Objective 3 was to provide the safety pilot with more flying time in Mode 4. The test verified Mode 4 functionality. There were five success criteria and four evaluation criteria.

Success Criteria:

1. Vehicle flown and recovered without damage
2. Ability to maintain positive control during benign flights demonstrated in Mode 4
3. Refined estimate of max flight time in Mode 4

4. Desired data collection
5. Pilot has sufficient time in each mode

Evaluation Criteria:

1. Safety pilot assessment of sufficient control authority (takeoff, fly, and recover)
2. Visual inspection and ground check for damage and abnormalities
3. Visual inspection of tail cameras for abnormalities
4. Pilot self-assessment of aptitude in Mode 3

The expected result was that Mode 4 should have sufficient but significantly less roll authority than Mode 3 because of the higher allocation to controlling yaw. The wing should have provided sufficient lift with no structural failures and the controller operated as expected.

Objective 4

Objective 4 was to collect data to enable building an analytical model of the aircraft performance. There were five success criteria and if the success criteria was met, the evaluation criteria was satisfactory.

Success Criteria:

1. Desired data saved onto the autopilot SD card
2. Desired data saved onto the Ardunio SD card
3. Battery consumption noted to calculate max flight time
4. Data collection for each point on test matrix
5. Aircraft flying as expected based off previous objectives

The expected result was that the vehicle flew as it did in previous objectives. There should have been sufficient amount of time to collect data. The controller was expected to operate for the full duration of flight and with no structural failures.

The test card for the flight test had all the same maneuvers as the previous test, but with one addition. Crabbing was added to the test card to test yaw control. Crabbing maneuver had the aircraft nose pointed toward the wind while the aircraft flies along a desired flight path.

3.6 Variable Camber Compliant Wing Simulation

USU Aero Lab developed a python simulator to attempt to replicate the flight of the VCCW. The simulator takes in real-time aircraft controls and states to compute the corresponding flight states. The computation is an integrator function that uses software called MachUp [7]. MachUp finds the aerodynamic characteristics based on the wing parameters [7]. Then, the simulation provides visuals of the flight. There is a real-time flight visual from the cockpit or rear view and a plot of the flight states over the flight duration. This thesis develops improvement to the simulation to more closely match the actual performance of the VCCW flight test data. The simulation is configured to use input from the actual flight test data. The objective is to have the simulation procedure a flight path similar to that actual flight test based on the test input.

3.6.1 MachUp

MachUp is an open-source tool to find aerodynamic characteristics on finite wings [7]. The tool is an algorithm based of Phillips and Snyder's lifting line algorithm as well as Prandtl's lifting line theory [49][50]. MachUp is used to determine the proper wing shape for a given amount of lift and minimal drag [7][8]. The simulation uses

MachUp to evaluate and optimize the geometric shape of the wing to improve flight performance.

Although MachUp is based on Prandtl's lifting line theory, the algorithm can be used on a sweep and dihedral systems [7]. MachUp is also based on Phillips and Snyder's lifting line algorithm, which is embedded in inviscid theory, but has the ability to include viscous effects [7]. MachUp equates the 3D vortex theory to the 2D section lift at the spanwise location to solve for the bound vortex strength at that location [7]. The algorithm is an iterated non-linear systems of equations. The initial solution is an approximation and Newton's method is used to iterate the system until it converges to the user specifications are met [7]. MachUp assumes the bound vortex follows quarter chord of the wing. The tool has multiple features that make the tool compatible for a wide range of wing designs and analysis: ability to model ground effect, trim an aircraft in pitch, locate the aerodynamic center, and compute stability, control, and damping derivatives [7].

The simulation uses MachUp to update the flight states. For each flight input, the simulation computes the states in an integrator function. The integrator function runs the data through a fourth order Runge-Kutta method. The Runge-Kutta embeds MachUp. MachUp solves for three force (X, Y, Z) and three moments (l, m, n) that are applied to the derivative functions. Finally, the simulation stores the updated flight states and loops back to compute the next set of inputs.

3.6.2 Original Simulation

USU Aero Lab's simulation has two main parts: flight visual and data logs with plots. The simulation receives real-time input then computes the corresponding flight states. The flight visual updates the display to show the aircraft in flight with the exact flight of the given input. When the flight is complete, the simulation creates a

data log and plot of the flight states. Figure 20 shows a flowchart of the simulation process.

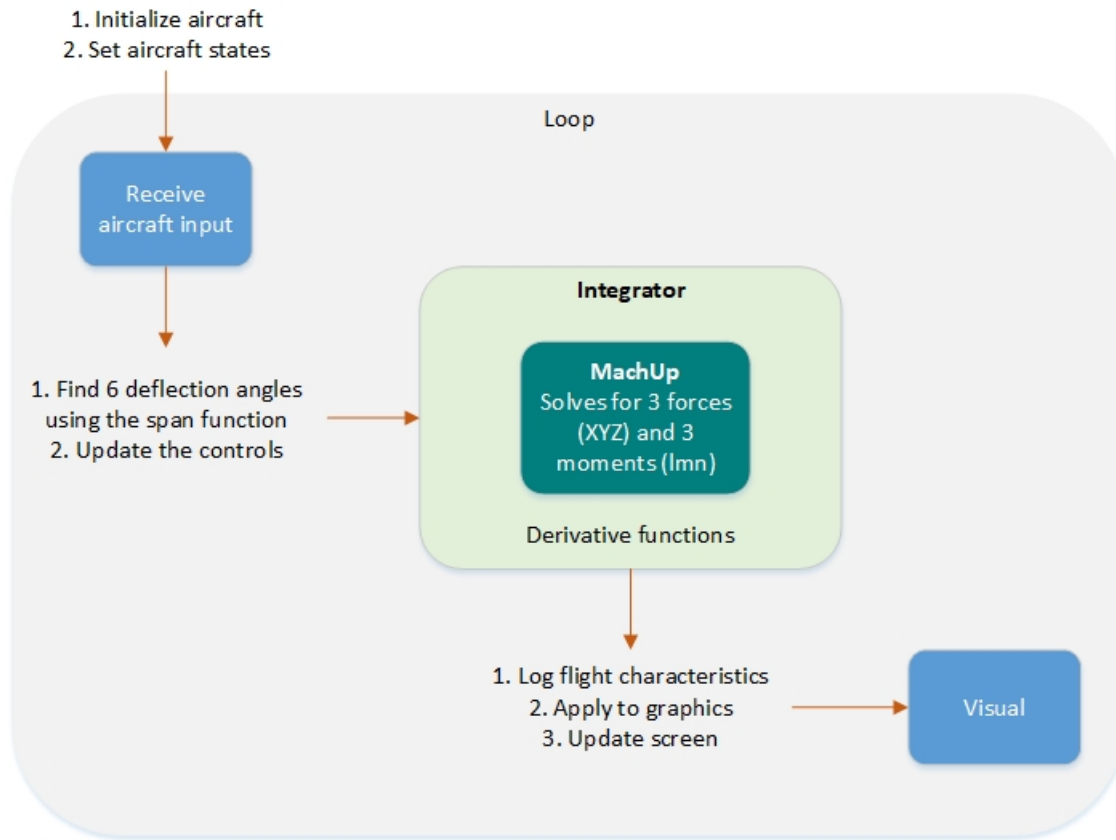


Figure 20: The simulation initializes the aircraft then enters a loop that computes the flight states. The simulation provides a visual of the aircraft with real-time inputs.

The simulation first needs to initialize the flight visual and the aircraft. The simulator initializes the flight visual window, aircraft graphics, flight data overlay, camera, and environment graphics. Then, the simulator initializes the aircraft of all the parameters, forces, moments, and flight conditions. All of the aircraft values can be changes to fit the measurements of aircraft. Once the simulation is done initializing, it enters a loop to receive input, compute the system, and provide the output through visuals.

The original simulation operates very similar to playing a video game. The simulator receives real-time aircraft control inputs from a computer keyboard or external

joystick. Control inputs include the throttle, aileron, elevator, and rudder. The simulation receives the aircraft input and finds the six deflection angles for the VCCW. The deflection angles are calculated using a span function. All of the controls are updated with the new deflection angles. The simulation then enters into the integrator. The integrator uses a fourth order Runge-Kutta method to solve the system. MachUp is embedded in the Runge-Kutta iteration to solve for the X , Y , and Z force and the l , m , and n moments. Then, the integrator passes the system through derivative functions to compute the flight states. The simulation logs all of the current flight states, applies the update to the graphics, and updates the visual flight. The simulation continues through the loop until the aircraft is at ground level (simulating a crash) or the user quits the simulation. The flight visual shows the real-time flight states of the aircraft from a cockpit or rear view. The software updates the display textual annotations six times a second. Figure 21 shows a running simulation.

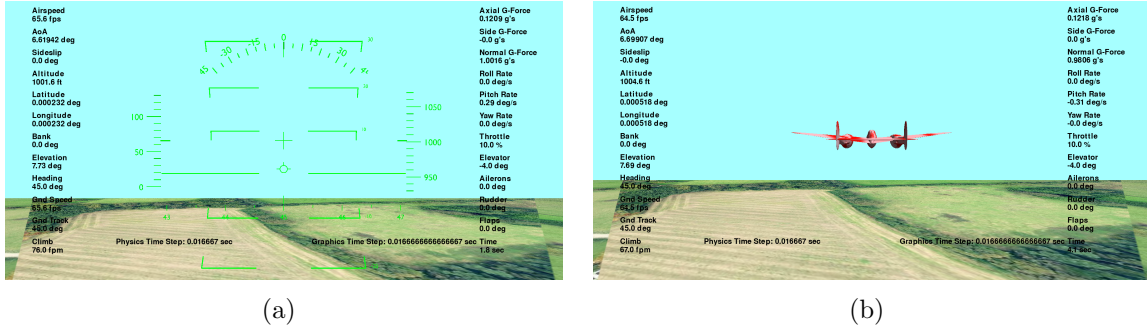


Figure 21: The simulation has graphics to give the user awareness of the aircraft's orientation. a) shows the user in the cockpit and b) shows the user a backside view of the aircraft. All of the flight states are shown along the left and right side of the screen with the corresponding time step and flight time at the bottom of the screen.

At the conclusion of the flight, the simulation outputs plots of the recorded flight data. The plot displays $[u, v, w, p, q, r, \phi, \theta, \psi, \dot{p}, \dot{r}, \delta_e, \delta_r, l_o, l_m, l_i, r_o, r_m, r_i]$. $[u, v, w]$ are the airspeeds in ft/s, $[p, q, r]$ are the angular velocities in rad/s, $[\phi, \theta, \psi]$ are the Euler angles of the aircraft, $[\dot{p}, \dot{r}]$ are the angular accelerations in degrees, $[\delta_e, \delta_r]$ are

the elevator and rudder deflections, and $[lo, lm, li, ro, rm, ri]$ are the VCCW angles of deflection in degrees. Figure 22 shows an example of the plot after a nominal flight.

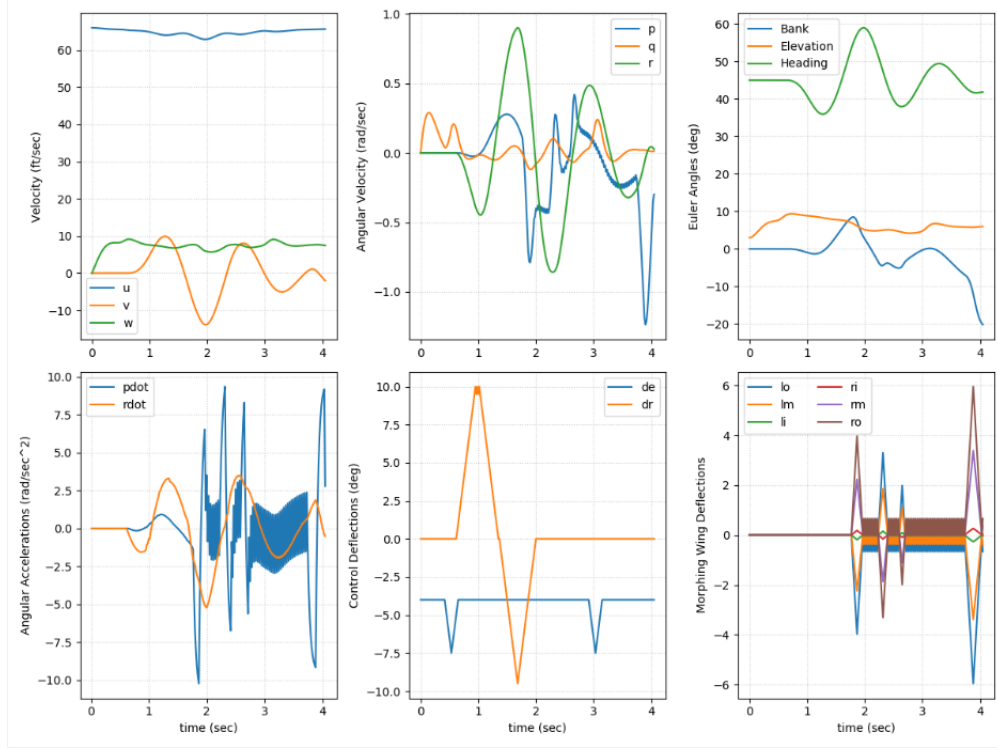


Figure 22: The plot displays all of the flight states. The figure shows $[u, v, w, p, q, r, \phi, \theta, \psi, \dot{p}, \dot{r}, \delta_e, \delta_r, lo, lm, li, ro, rm, ri]$. This was a nominal flight of four seconds to use all control inputs.

3.6.3 Research Simulation Refinement

This thesis builds on the original simulation. The purpose of the simulation refinement is to closely recreate the actual flight of the VCCW in the simulator. Developing and tuning of the simulation come from comparing the simulation flight results and actual flight data. The simulation reflects the actual aircraft parameters used during flight testing.

The simulation process changes the way it receives the flight input. The original simulation receives real-time input from the user. For this research simulation, the input needs to come directly from the flight data. All of the initial aircraft states

come directly from the flight data and the MOI will come from the bi-filar pendulum results. The simulation code needs to be modified to store the flight data log, read the first time stamp for initialization, and sequentially loop through the data to calculate the simulation flight states. The original plot of flight data needs to be modified to closely compare the flights. The plot will be modified to show the comparison between the actual flight data and the simulation data in $[u, v, w, p, q, r, \phi, \theta, \psi]$. $[u, v, w]$ are the airspeeds in ft/s, $[p, q, r]$ are the angular velocities in rad/s, and $[\phi, \theta, \psi]$ are the Euler angles of the aircraft. Figure 23 shows an example flight segment comparing the actual flight data and the calculated simulation data.

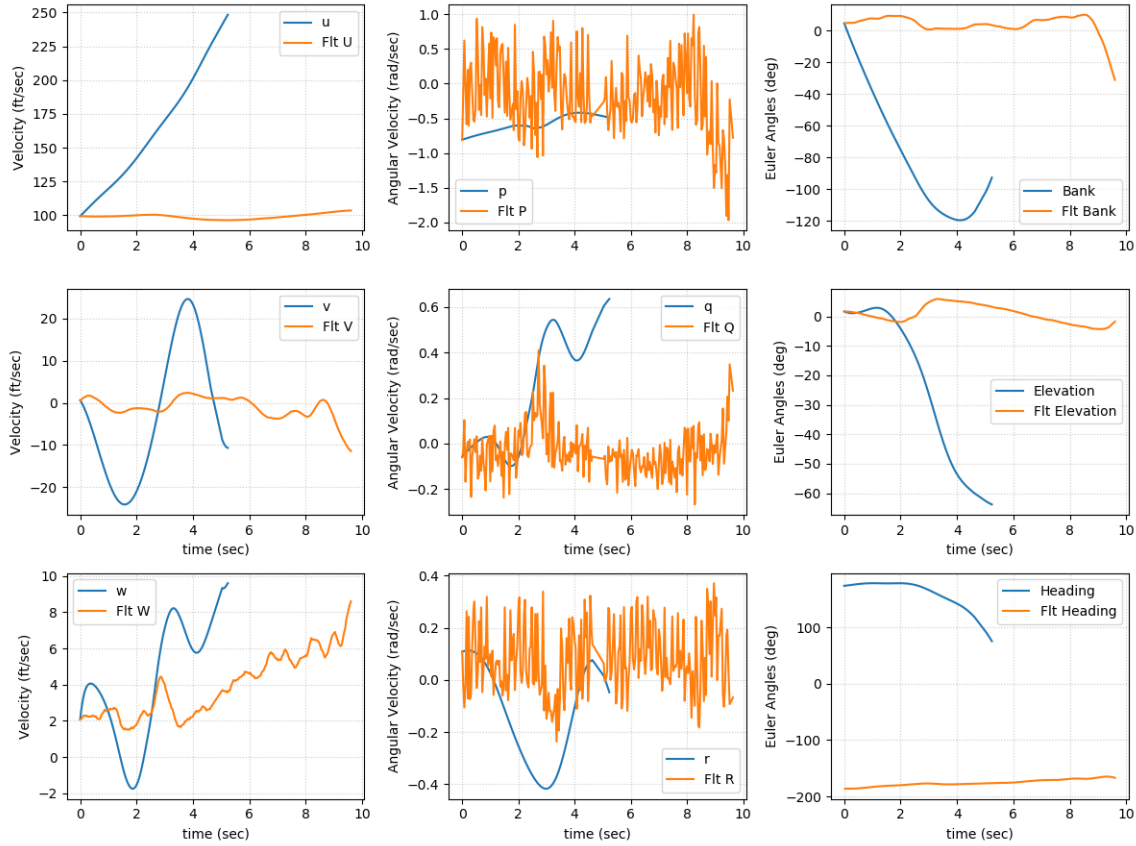


Figure 23: The plot displays the comparison between the actual flight data and the calculated simulation data. The simulation flight is in blue and the actual flight data is in orange. The data is a nine second snippet of a flight. The simulation data stops around five seconds because the aircraft's altitude was zero.

3.7 Methodology Summary

Chapter III discussed the methodology of this thesis. The chapter was broken into six sections: aircraft dynamics, VCCW overview, bi-filar pendulum, high speed static wind test, flight testing, and simulation refinement. Aircraft dynamics provided a high level explanation of aerodynamic components and stability which is essential to know before understand this thesis. The next section described the VCCW. The VCCW overview explained the design, the controller, and the different flight modes. The next three sections were testing procedures. The bi-filar pendulum test set up how the MOI measurement was completed. The high speed static wind test examined the capabilities of the prototype wing under various loads. Flight testing demonstrated the capabilities of the VCCW. The chapter closed with simulation refinement. The simulation will be tuned to closely match the actual flight data as a tool for future VCCW development. This chapter set up the research work described in Chapter IV.

IV. Results and Analysis

Chapter IV is an overview of all of the results from testing and analyzing the data. There are results for the bi-filar pendulum test and flight tests. After reviewing the results, the data is used in the simulator. Chapter IV then dives deep into tuning the simulation to perform as close to the actual flight test as possible.

4.1 Bi-filar Pendulum

This section describes the bi-filar pendulum test and results. The test measures the moment of inertia (MOI) of complex bodies. The bi-filar pendulum test was completed on the base wing and variable camber compliant wing (VCCW). The results shows the MOI measurement and standard deviations.

4.1.1 Bi-filar Pendulum Test

Bi-filar pendulum test section provides an overview of how the test was conducted. Bi-filar pendulum testing measured the MOI for the aircraft. There were tests for the different wings: base wing and VCCW. Each wing had three configurations (roll, pitch, and yaw), of three filar lengths, and three replications of each filar length. There were a total of 27 test completed on each wing. Each test measurement was the MOI at the suspension point. The CG MOI was found using the parallel-axis theorem (3).

The mass of the base wing aircraft was 15.25 kg and the VCCW was 16.95 kg. The distance between the filars was 0.7620 (consistent distance throughout testing). With each trial, the length of the filars changed. There were three different lengths of filars. In order to get the most accurate data, the test was repeated three times at each filar length (total of nine data collection for each axis) and averaged.

The aircraft could not be mounted directly through the center of gravity (CG) because the aircraft needed to be used in the future. Mounting the aircraft at the CG required drilling holes into the fuselage and on-board hardware, decommissioning the aircraft. However, the aircraft was part of a developing VCCW project. Therefore, MOI measurements were from the suspension point. The parallel axis theorem (3) calculated the MOI at the CG using the length difference between suspension point and the CG described as:

$$I_{CG} = I_{suspension} + md^2. \quad (3)$$

In (3), d was the distance between the CG and the filar length, m was the mass (kg) of the aircraft, I_{CG} was the MOI (kg m²) at the CG, and $I_{suspension}$ was the test measurement MOI (kg m²). Figure 24 shows the different configurations during testing. Figure 24(b) and 24(c) show the filar suspended from the fuselage and then from the wing and landing gear in Figure 24(a).



(a)



(b)



(c)

Figure 24: Bi-filar pendulum testing configurations shown in (a) roll, (b) pitch, and (c) yaw. The aircraft could not be suspended directly through the CG as holes could not be made in the aircraft. The difference between the suspension point and CG provided the calculated MOI at the CG.

Figure 25 shows the VCCW in one configuration. The bottom of the VCCW is For Official Use Only (FOUO). The majority of bi-filar pendulum testing pictures display the bottom of the wing and therefore cannot be shown like Figure 24.



Figure 25: Testing on the VCCW occurred after all the flight test were completed. The aircraft is in the roll configuration and suspended by the fuselage to prevent damage to the wing. One of the Vicon cameras is shown in the top right corner. The 15° rotation marker is shown below the aircraft.

4.1.2 Bi-filar Pendulum Results

This section will discuss the results of the bi-filar pendulum test on the base wing and VCCW. There were notable difference between the results due to the structure of the wings. Because the wings were complex bodies and had no previous MOI measurement, a validation test on a known object was completed to compare the results.

The base wing had MOIs of 2.077 kg m^2 , 1.9532 kg m^2 , and 3.2904 kg m^2 in the roll, pitch, and yaw configuration, respectively. The VCCW had MOIs of 4.6745 kg m^2 , 1.7489 kg m^2 , and 5.4744 kg m^2 in the roll, pitch, and yaw configuration, respectively. The standard deviations for all configurations were less than 0.14. The roll and yaw MOI were higher while the pitch MOI was slightly lower in the the VCCW.

The results for the base wing and VCCW are shown in Tables 3 and 4. In Table 3, the pitch and yaw configurations only show two trials. The third trial demonstrated large outliers and was eliminated. Removing the outliers improved the standard deviation for the pitch and yaw configurations substantially, from 0.428 to 0.0152 and 0.5515 to 0.1369, respectively.

In Table 4, there were extra data points for the roll configuration. During testing, there was uncertainty if the Vicon chamber was collecting data so an additional collection was made. The additional collection was added to provide a better statistic.

The standard deviations for the VCCW were much better than the base wing. The VCCW weighed almost 1 kg more than the base wing and was evenly distributed. Therefore, the VCCW was expected to have a different roll MOI. Because the VCCW weighed more, the base wing had weights added to it. The best way to emulate the wing was to place the weights farthest from the fuselage. However, the structure of the base wing was not built for additional weight. There was one spar that spanned $3/4$

Table 3: Bi-Filar Pendulum Base Wing Results. Average MOI and standard deviation are calculated from the all of the MOI from each configuration. Roll MOI = 2.08 kg m², pitch MOI = 1.95 kg m², and yaw MOI = 3.29 kg m².

Configuration	Filar Length (m)	MOI (kg m ²)	Avg MOI (kg m ²)	Std Dev
Roll	3.8481	2.0933	2.0777	0.0133
		2.0893		
		2.0845		
	3.4798	2.0536		
		2.0901		
		2.0630		
	3.1623	2.0730		
		2.0735		
		2.0791		
Pitch	4.6419	1.9768	1.9532	0.0152
		1.9320		
		1.9481		
	4.1815	1.9469		
		1.9624		
		1.9531		
Yaw	5.4483	3.1808	3.2904	0.1369
		3.1544		
		3.1626		
	5.0451	3.4027		
		3.4118		
		3.4302		

Table 4: Bi-Filar Pendulum Variable Camber Compliant Wing Results. Roll MOI = 4.67 kg m², pitch MOI = 1.75 kg m², and yaw MOI = 5.47 kg m². The standard deviations are better as a whole than the base wing testing.

Configuration	Filar Length (m)	MOI (kg m ²)	Avg MOI (kg m ²)	Std Dev
Roll	3.7851	4.5995	4.6745	0.0930
		4.5615		
		4.7840		
		4.7628		
	3.6561	4.5963		
		4.5961		
		4.6339		
		4.6270		
	3.4476	4.7589		
		4.6671		
		4.8325		
Pitch	4.5091	1.8229	1.7489	0.0468
		1.7698		
		1.8277		
	4.2871	1.7107		
		1.7133		
		1.7255		
	4.0761	1.7159		
		1.7336		
		1.7208		
Yaw	5.4871	5.5070	5.4744	0.0518
		5.5000		
		5.5173		
	5.2821	5.4478		
		5.4579		
		5.4488		
	5.0381	5.5656		
		5.4248		
		5.4005		

of the wing on each side from the fuselage. For safety reason and damage prevention to the base wing, the weights were added at the ends of each spar to get the weight as far away from the fuselage without causing the wing to break during flight. The added weight simulated the same thrust and power depletion on the base wing.

After comparing the bi-filar results, the base wing yaw standard deviation was significantly higher than the rest of the data. Table 4 removed one of the yaw filar lengths to improve the standard deviation. However, the standard deviation was not as low as the rest of the configurations. The test should be completed again to verify the collected data.

Although the base wing MOI results were important, the VCCW MOI measurements were more pertinent to this thesis. The VCCW results showed measurements with standard deviations less than 0.01.

For the purpose of the thesis research, only the VCCW results were used in the simulation. The base wing results can be used in future simulation development. The average MOI shown in Table 4 were used in the simulation as the best reflection of the aircraft.

4.1.3 Verification Test

To verify the bi-filar pendulum test, an object with a known MOI was also tested. The object was a 80/20 metal rod that was 4.96 kg. The 80/20 metal rod measured 2.469 m in length and 0.0381 m in width and height. Using Solidworks, the CAD model was created to find the MOI. The length of the filars was 4.9911 m and the distance between the filars and CG was 0.0381 m. Verification testing used the exact procedure from the aircraft testing. Table 5 shows the comparison from the bi-filar pendulum test results with the 80/20 rod.

There was a 0.7315% error between the bi-filar pendulum MOI and actual MOI.

Table 5: 80/20 Rod Verification Test Results on Bi-Filar Pendulum. The test was completed to compare how accurate the method was to the actual MOI measurement. The test had a 0.7315% error.

Method	MOI (kg m ²)
Vicon	2.49
	2.51
Solidworks	2.52

Therefore, the verification test showed there was high confidence in the data accuracy of the bi-filar pendulum measurements.

4.2 High Speed Static Wind Test Results

The high speed static wind test ensured the VCCW could withstand flight loads. Testing took place on 10 Apr 2019 around 1000. The test increased the load factor from 0 to 4 by changing the angle of attack, deflection angle, and airspeed. The test points had the angle of attack range from 0-20°, deflection angles ranged from 0-15°, and the airspeed ranged from 0-80 mph.

Although the test points (found in Figure 19) show the maximum airspeed of 80 mph, the truck maximum speed was 70 mph for safety reasons. There were cameras mounted on the truck to record the leading and trailing edge of the wing.

The test performed all of the 0-3 load factor test points. Only some of the 4 load factor test point were completed due to time constraints. The wing was also mounted with a -15° angle of attack to test for any damages. At the end of each test, there were no visible damages to the wing. However, the cameras showed that at 3-4 load factors, the leading edge deflected about 1/8 inch in between the ribs due to the load. To prevent that deflection from high loads, the wing structure changed to add a stringer between the ribs to thicken the leading edge.

4.3 Flight Test

The flight test section describes the flight test process. There were procedures for every test day and every flight. The base wing and VCCW had different objectives. All the objectives were tested through multiple flights to gather data for wing capability analysis and this thesis simulation.

During flight testing, every team member had a role to ensure time efficiency. As a person gaining information from the project, I was the one of the test directors with another AFIT (Air Force Institute of Technology) person. The test director led and executed the flight test. AFIT provided the personnel for the ground control station and safety pilots. AFIT, AFRL (Air Force Research Laboratory), and USU (Utah State University) Aero Lab provided ground operations and observers.

At the beginning of every flight test day, the test director conducted a range and safety brief. The brief went through general minimizing procedures and considerations, operation risk management (ORM) checklist, weather conditions and safety hazards, role assignment, flight specific risk, and the objectives. All of the test team needed situational awareness during every flight to ensure the safety of the team, aircraft, and environment. The ORM checklist confirmed the team was conducting the test under good conditions and awareness of any additional risk. The flight risk and objectives discussed in Section 3.5 were reiterated to the team at the start of every flight test day.

Prior to every flight, the test team ran through an aircraft checklist. The checklist ensured the proper order to power on the aircraft. The order of the checklist was essential because there were hardware and software parts that affected other parts during powering on. The test team ensured the aircraft was properly calibrated, recorded data, had working signals to the ground control station, and had working signals to the remote controller (RC).

Each flight had set maneuvers from the test card. Not all the test points could be met in one flight. There were about 5-6 flights per day over the course of 1-3 days. Due to battery consumption, the longest allowed flight time was 15 minutes. The batteries were replaced at the end every flight to ensure the aircraft was flying with the highest potential power.

The weather was recorded before every flight for data analysis. The quality of the wind speed measurements need additional work to validate. The anemometer was the only means of wind measurements and did not update real-time.

4.3.1 Base Wing

Base wing flight testing took one day with six flights at the Wright-Patterson airfield. The winds did not exceed 12.3 mph and temperatures ranged between 70-89°F. The purpose of the base wing flight was to prepare for flight with the VCCW and to gather data and insight into how it might behave beforehand.

Base wing flight testing focused on specific RC input. The flight test data points had aileron, elevator and rudder pulse inputs in both directions (right/left and up/-down). The flight also included right and left coordinated turns to observe the RC input of more than one controller. The Pixhawk recorded all of the flight data. The RC input was recorded in pulse width modulation (PWM) values. The aircraft's states were recorded in metric system units. The base wing is shown in Figure 26.

With the base wing flight data, the test team had the opportunity to compare the flight states and determined what aspects of the VCCW is more efficient. The simulation will use the flight data to verify the accuracy between virtual and actual flight test data.



Figure 26: Base wing during take off. The base wing has all of the standard control capabilities: aileron, elevator, and rudder. The fuselage is designed to use either the base wing or VCCW.

4.3.2 Variable Camber Compliant Wing Flight Test

All VCCW flight tests were at Camp Atturbery, IN. For flight safety, the test was conducted in a “restricted airspace” flight environment. The intent was to fly two sets of flight test: one to focus on roll control and the other to focus on yaw control.

The roll control test was in mid-September 2019. Flight testing took three days for seven flights. The temperature varied from 75-92°F, with winds up to 15 mph. The wind limit set in the training safety board was 15.725 mph. However, the team decided not to fly with winds over 12 mph for the first flight of for the aircraft’s safety.

The VCCW test repeated many of the base wing test objectives as it is necessary to have similar conditions to compare data. The recorded data had right/left and up/down pulse input for all three controls (aileron, elevator, and rudder). For the purpose of the simulation, the recorded flight data focused on the aircraft output from a single pulse input.

The yaw control test was in mid-October 2019. Flight testing took two days for eight flights. The temperature ranged between 60-78°F, with winds up to 12 mph. Figure 27 show the VCCW during flight.



Figure 27: The VCCW shows anti-symmetric trailing edge deflection. The right ribs are deflecting the edge down. The deflection changes cause the wind to blow over the wing creating lift on the wing to control the aircraft.

The yaw control flight test had all the same flight objectives as the base wing and roll control. However, the Mode 4 (yaw control) flight did not go as predicted. The wing control of the yaw moment was not sufficient and the aircraft climbed during yaw maneuvers.

Although Mode 4 did not produce sufficient yawing moments, all the test objectives were met. The objectives were to fly the aircraft and verify the functionality. The VCCW was able to demonstrate minimal yaw authority. The aircraft maintained positive control while in Mode 4 and all the desired data was collected.

At the completion of Mode 4 testing, the wing's limits were tested during an aerobatic flight. The wing endured aileron rolls, loops, wing overs and inversions successfully. There was no damage to the wing on the plane after these maneuvers.

The overall objective for flying the VCCW was to demonstrate the viability of the roll and yaw control. The objectives were met through all of the flight testing. There were no damages to the aircraft and all of the capabilities of the wing were documented.

4.3.3 Flight Analysis

The VCCW had successful flights without damages but what kind of capabilities did it have? The next section compares the base wing flight to the VCCW flights.

The Pixhawk data was used to compare the control capabilities. The Pixhawk recorded the RC input and the states of the aircraft. Matching the input and attitude for specific maneuvers showed the capabilities of the aircraft. Because Mode 4 did not produce sufficient yawing moments, only Mode 3 was analyzed for roll authority.

The base wing data analysis was from the fourth base wing flight test. The flight test points were to perform aileron and rudder only turns. Figure 28 shows the aileron states of the base wing. The figure shows aileron and rudder inputs as well as roll and yaw attitudes. The yaw was included to help determine the orientation of the aircraft and when the aircraft was on a straight pass for flight maneuvers.

Looking at the aileron and roll plots, the aircraft alternated between left and right aileron turns. The rudder plot shows there was close to no rudder input during the turns. The spikes on the rudder plot were during a turn to reorient the aircraft. The roll plot shows roll angles from about -50 to 10° . The mean of data in the plot is -22.41° . Therefore, the base wing provided about $\pm 30^\circ$ roll control.

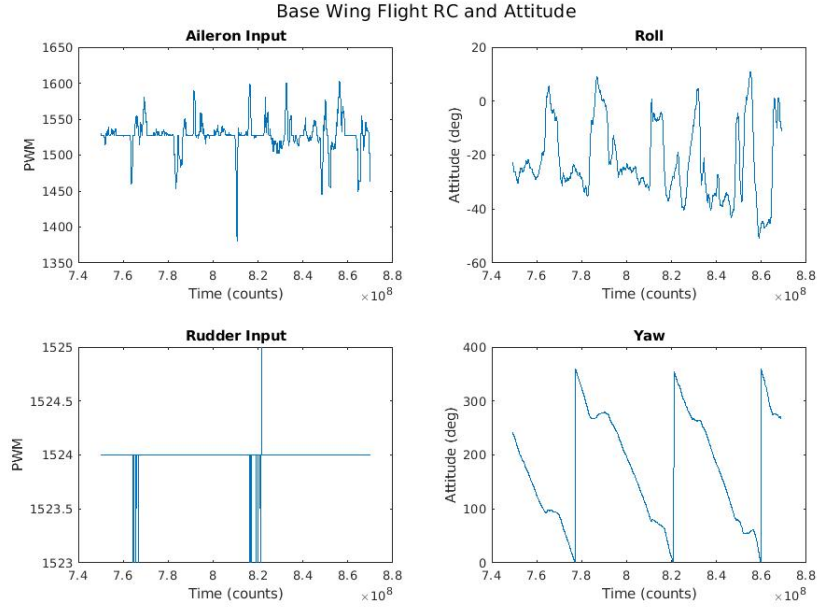


Figure 28: The plot shows the RC input for aileron and rudder and the attitude for roll and yaw. The aileron and roll plots shows the roll capabilities of the aircraft. The yaw plot helps determine the orientation of flight. The roll attitude ranges from about -50 to 10°.

The VCCW data was from its first flight test. The data was from flight seven of the flight testing. The test points were to perform right and left aileron only turns. Figure 29 shows the aileron states of the VCCW.

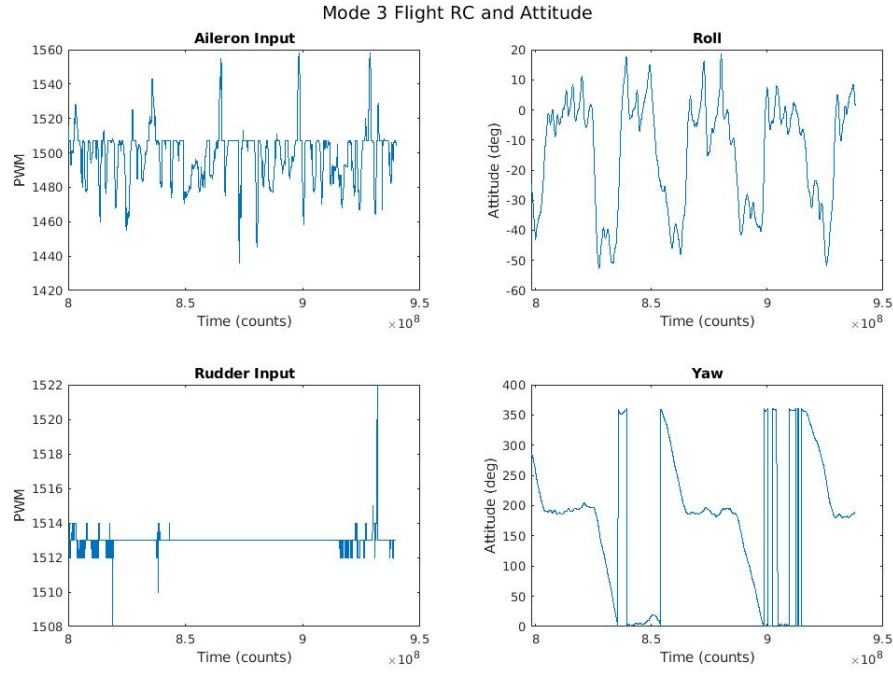


Figure 29: The plot shows the RC input for aileron and rudder and the attitude for roll and yaw. The aileron and roll plots shows the roll capabilities of the aircraft. The roll attitude ranges from about -52 to 18° .

Figure 29 shows the aircraft alternated between left and right aileron only turns. The roll angles for the plot data ranges from about -52 to 18° . The mean of data in the plot is -14° . Therefore, the VCCW provided about $\pm 35^\circ$ roll control. The rudder input shows some input but it was when the aircraft was performing a coordinated turn.

Because some of the data in Figure 29 contains some rudder input, the plot was zoomed in on. Figure 30 shows a zoomed plot where there is no rudder input to observe the pure capabilities of the aileron control of the VCCW.

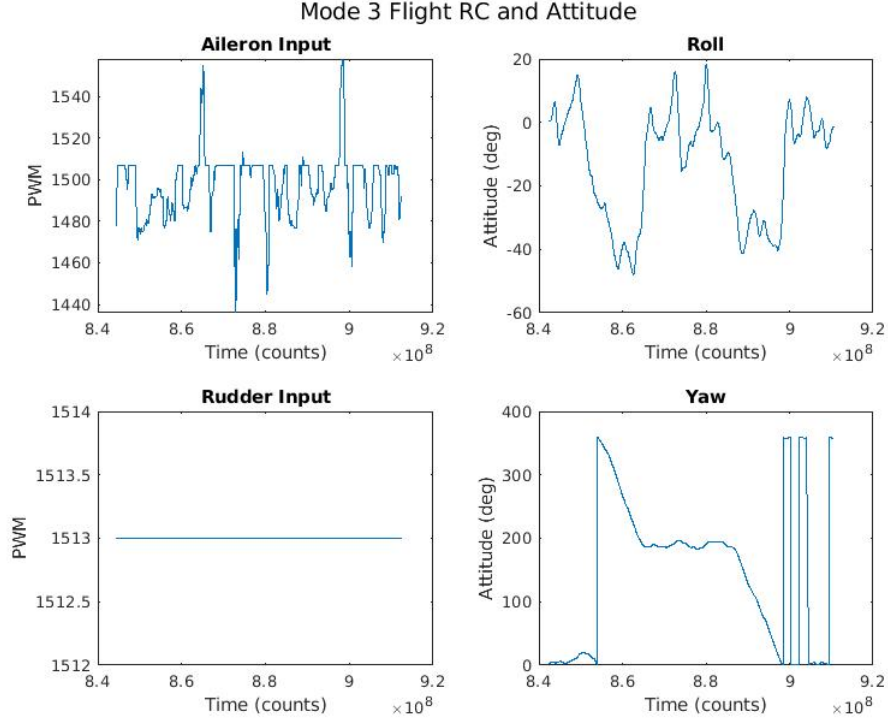


Figure 30: The plot shows zoomed version of Figure 29. There is no rudder input in this plot with one pass of left and right aileron turns.

With the pure aileron control, the roll attitude ranges from about -48° to 18° . The mean of the data is -13.23° . Therefore, the pure roll capability of the VCCW provided about $\pm 33^\circ$ roll control. Based on the data analysis, the VCCW roll control provided more roll authority than the base wing.

This analysis is not a conclusive, qualitative complete demonstration of the VCCW. The VCCW capabilities are more than this section describes.

4.4 Data Collection Analysis

Data collection analysis discusses the analysis of the recorded flight data. The data had to be analyzed and converted to be compatible with the simulation. The Pixhawk recorded all of the flight parameters and states during flight test. The RC input, airspeed parameters, and data alignment were converted for simulation use.

The simulation uses Python and Matlab®. USU Aero Lab’s simulation is in Python and the flight test data was mostly plotted in Matlab®.

The Python simulator needed flight states to run the simulation. The initial conditions were airspeed, time, altitude, inertial position, inertial velocity, attitude, and body fixed frame rate. The actual RC controller input of throttle, aileron, elevator, and rudder were the input for the simulation. However, the flight data had to be trimmed and converted to be compatible with the simulator.

4.4.1 RC Input

The Pixhawk recorded the RC input in PWM values. The simulation required a conversion from PWM to degrees. The conversion procedure used a PWM servo tester and protractor. The PWM servo tester sent PWM values to the aircraft servos just like the RC controller did. Because the VCCW replaced the ailerons and flaps, only the rudder and elevator required deflection measurements. Deflection was found by using a protractor to measure the deflection angle between 1100-1900 PWM rates at every 100 value. There was an expected linear relationship between PWM and degree measurements. The relationship and calculated conversion is shown in Figure 31.

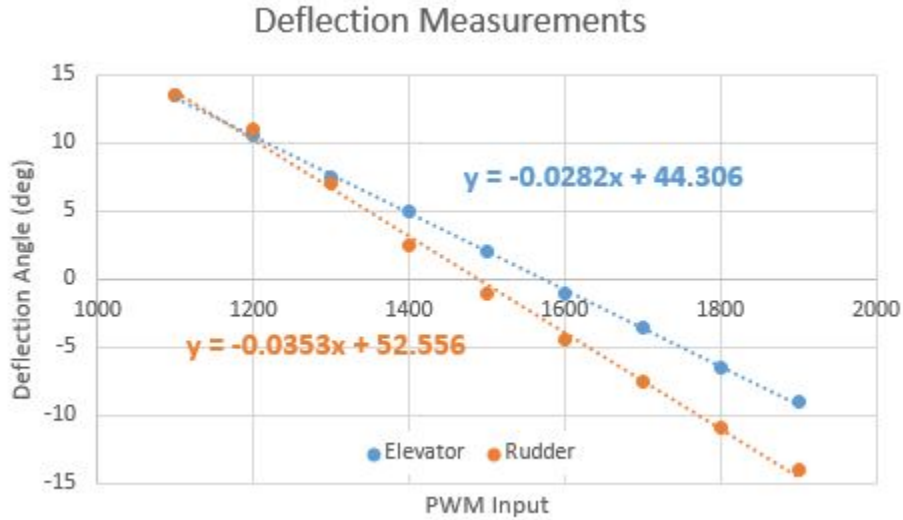


Figure 31: The relationship between PWM and degree measurements are linear. The elevator and rudder equations were used to convert the PWM values into degrees of deflection. The elevator relationship is $y = -0.0282x + 44.306$ and the rudder relationship is $y = -0.0353x + 52.556$ where x is the PWM value and y is the corresponding degree value.

The equations found from the relationship shown in Figure 31 converted the RC input in PWM to RC input in degrees.

The throttle input was also recorded in PWM values. However, the simulation needed the throttle input as percentage values between 0-1. The PWM throttle range was 1187-1769 and was normalized to a 0-1 range to work with the simulation. The throttle input controlled the propeller rotation rate that affected the thrust of the aircraft. As battery capacity depleted, the aircraft required more throttle to provide the same amount of thrust. However, during flight testing, the test team was careful not to overdraw the batteries with long flights. Therefore, the throttle normalization relationship was valid.

4.4.2 Airspeed Parameters

The Pixhawk measured the aircraft's velocity in the local navigation north, east, down (NED) frame, as ground speed. The NED frame is also referred to as the vehicle frame. The aircraft's velocity in the simulation is expressed as airspeed in the body fixed frame. To convert the ground speed into airspeed, the wind speed was needed. The Pixhawk recorded the wind speed in the north and east direction. (4) [44] shows the conversion from ground speed to airspeed. The velocity with respect to the surrounding air is (V_a). The ground speed is (V_g) and the wind speed is (V_w). The relationship between the velocities are

$$V_a = V_g - V_w = \begin{bmatrix} u_g - u_w \\ v_g - v_w \\ w_g - w_w \end{bmatrix}, \quad (4)$$

where u , v , and w are north, east, and down, respectively. (4) calculated the airspeed of the aircraft in the NED/vehicle frame. To transform from the NED frame to the body fixed frame, the frame transformation (5) [44] is

$$R_v^b(\phi, \theta, \psi) = \begin{bmatrix} 1 & 0 & 0 \\ 0 & \cos\phi & \sin\phi \\ 0 & -\sin\phi & \cos\phi \end{bmatrix} \begin{bmatrix} \cos\theta & 0 & -\sin\theta \\ 0 & 1 & 0 \\ \sin\theta & 0 & \cos\theta \end{bmatrix} \begin{bmatrix} \cos\psi & \sin\psi & 0 \\ -\sin\psi & \cos\psi & 0 \\ 0 & 0 & 1 \end{bmatrix}. \quad (5)$$

Using the results from (4) and (5), the airspeed in the body fixed frame calculation is shown in (6).

$$V_a^b(\phi, \theta, \psi) = R_v^b(\phi, \theta, \psi) \cdot V_a = R_v^b(\phi, \theta, \psi) \cdot \begin{bmatrix} u_a \\ v_a \\ w_a \end{bmatrix} \quad (6)$$

4.4.3 Sample and Hold

The Pixhawk recorded all the flight parameters in different categories. The categories had different time stamps and frequencies of recorded data. The time was recorded in microseconds at a rate of about 25 messages per second with all the categories of data having slightly different time stamps. To line up all the data with the same time stamp, the data was processed in a “sample and hold.” Sample and hold passed all the data through loops to match the same time stamps while keeping its respective data.

1. Trimmed the data points with the same overall range
2. Processed time stamps to get samples at matching time steps
3. Processed the updated data to have the same amount of time steps

The sample and hold process trimmed the data for the same time stamp range, aligned the time steps, and adjusted each flight parameter to have the same data array size. From there, the data was ready to be passed to the Python simulation.

4.5 Simulation Refinement

The simulation refinement tuned USU Aero Lab’s original simulation to closely match the flight test. The simulation analysis was performed on four different segments of a flight test to look at various parts of a flight. Tuning required data conditioning including filtering and bias removal. Most of the simulation tuning was

on the thrust model. There were two types of thrust approaches: least square and static. Least square approach had two different designs that calculated multiple models. The static approach had two different models. All of the tuning analysis was to improve the simulation results to closely reflect the flight data.

The simulation received real flight control input to attempt to recreate the flight test in simulation outputs. This process demonstrated how accurately the simulator could model the VCCW. As discussed in Chapter III Section 4.4, Matlab®scripts processed the data to be compatible with the original simulation by:

1. Trimming the data to smaller time segments
2. Lining up the time stamps for all Pixhawk data
3. Matching time stamp occurrences, as described in Section 4.4.3
4. Converting RC PWM inputs to degrees
5. Normalizing the throttle input, and
6. Converting NED frame ground speed to body frame wind speed,

The simulation used the initial flight states $[u, v, w, p, q, r, N, E, D, \phi, \theta, \psi]$ to calculate the current flight states. $[u, v, w]$ are the airspeeds in ft/s, $[p, q, r]$ are the angular velocities in rad/s, $[N, E, D]$ is the position in ft, and $[\phi, \theta, \psi]$ are the Euler angles of the aircraft. The simulation took the current flight states and processed them through the integrator to update the flight states. This process was repeated along the entirety of the actual RC control data log.

The analysis was on a Mode 2 (anti-symmetric and symmetric trailing edge deflection) flight completed during the roll control testing. The flight was on 10 September 2019 at 1237 with temperatures in the low 90°Fs with winds south south west at two mph.

The research analysis focused on the comparison of the airspeed (u, v, w) , angular velocity (p, q, r) and Euler angles (ϕ, θ, ψ) . The simulation used the actual RC control data (aileron, elevator, rudder and throttle) as input for the MachUp iteration.

4.5.1 Flight Segments

The research analyzed segments of the flight due to the constraints and availability of appropriate data. There was an assumption that the wind measurement was accurate. Wind did not impact the simulation if the wind was accurately measured and reflected in the flight data. To look different parts of the flight and effects of the tuning, the flight was analyzed at specific segments. There were four analyzed flight segments (shown in Figure 32):

1. Segment A (4.6 second flight segment in wind direction)
2. Segment B (9.6 second flight segment in wind direction)
3. Segment C (8.4 second flight segment in crosswinds)
4. Segment D (3.8 second flight segment in crosswinds)

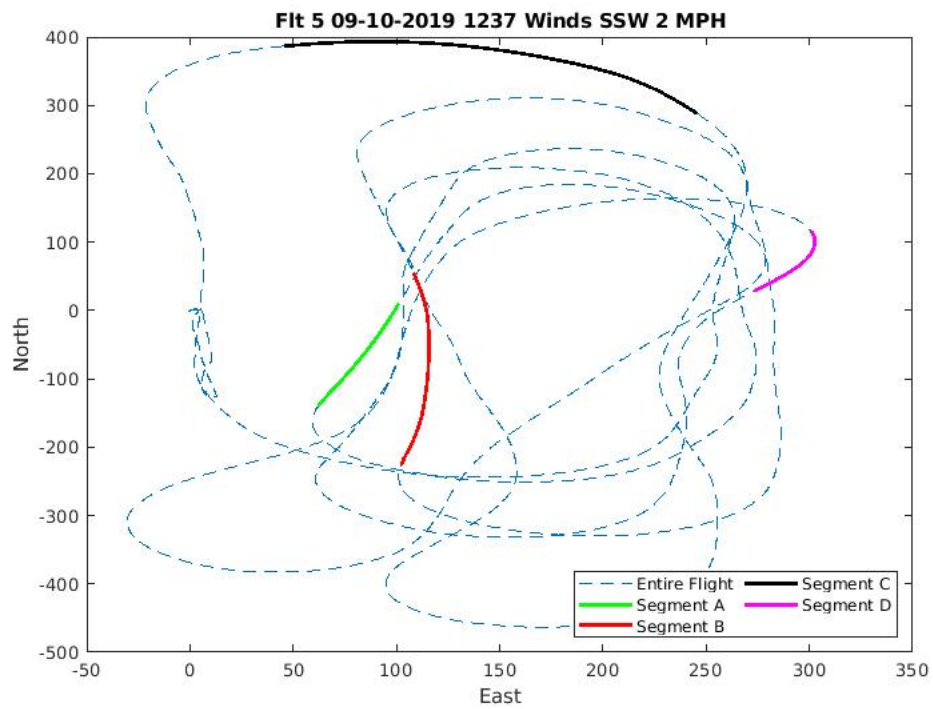


Figure 32: The figure shows flight path of the entire flight and each segment. Take off and landing are the origin. The winds for this flight was two mph SSW. The entire flight is in a blue dashed line, Segment A is a solid green line, Segment B is a solid red line, Segment C is a solid black line, and Segment D is a solid magenta line.

Prior to any simulation refinement, the four flight segments ran in the original simulation but did not perform the same as the flight test. Figure 33 shows the original simulation of Segment B.

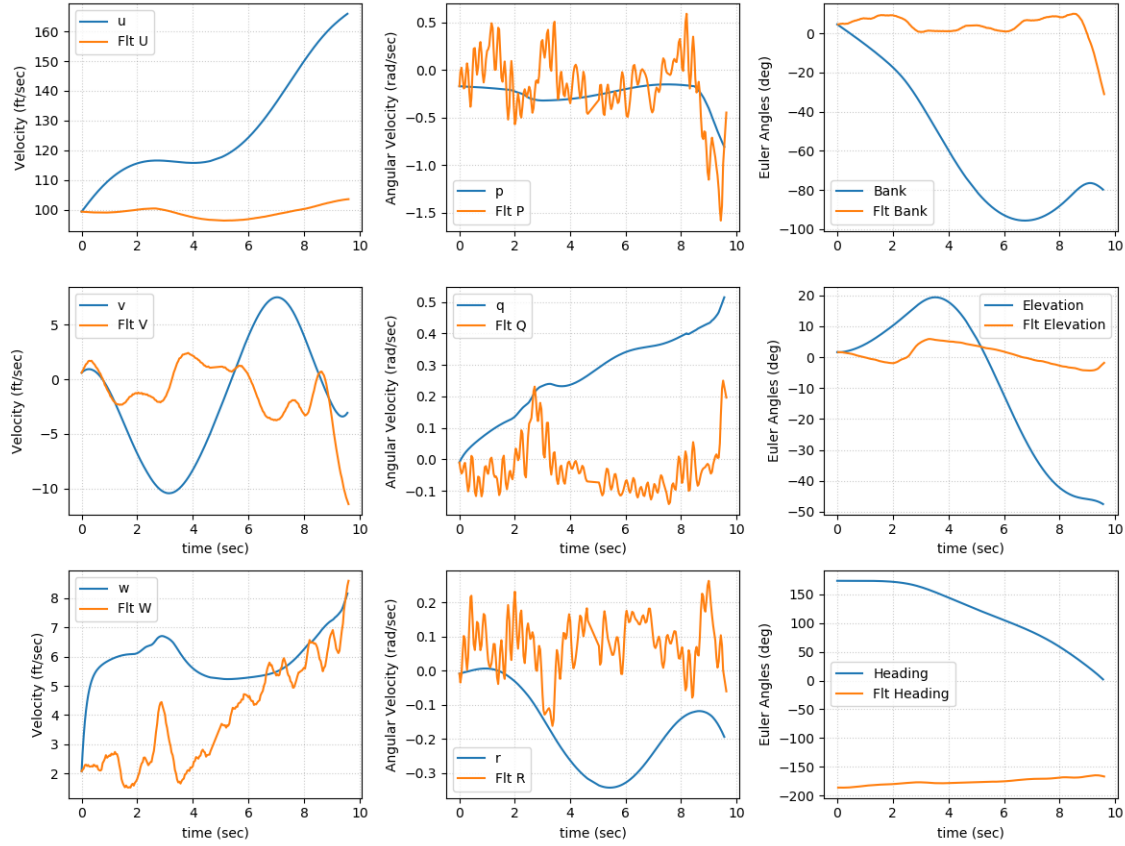


Figure 33: The figure shows the original output of the simulation for the Segment B. Blue shows the simulation data and orange shows the actual flight data. Flight states of u , v , w , p , q , r , ϕ , θ , and ψ are compared.

4.5.2 Data Conditioning: Filtering

The angular rates (p, q, r) were recorded from the gyroscope during flight. The data collection contained noise. To find more accurate data, the angular rates were filtered. The filtered data is shown in Figure 34.

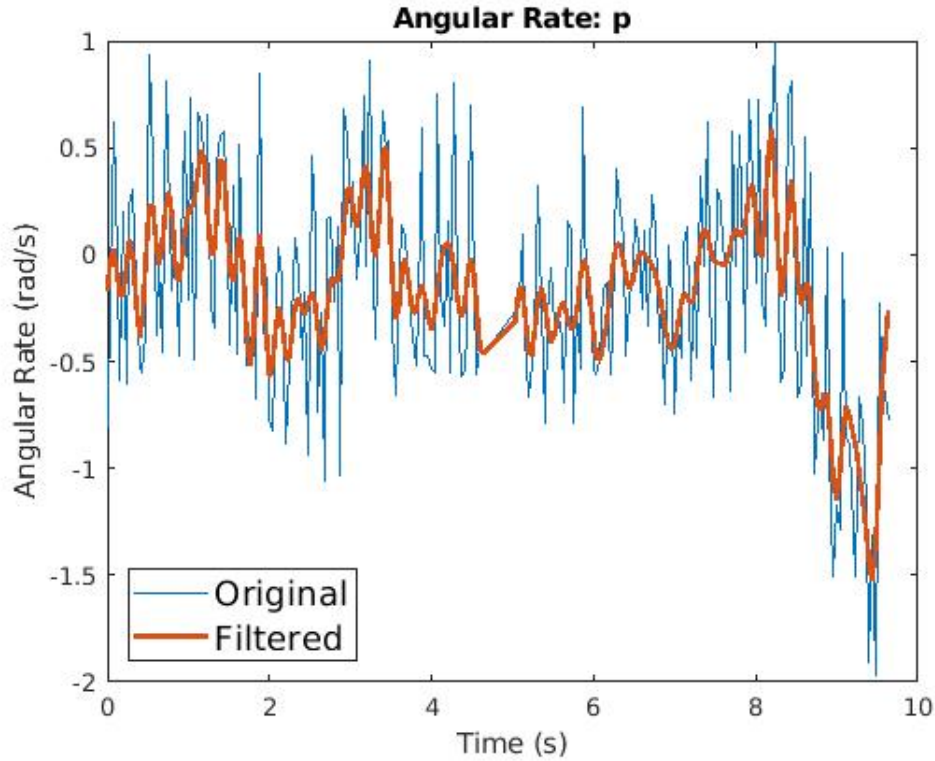


Figure 34: The plot contains the original angular rate p data and filtered data. The data was processed through a lowpass filter with a bandpass frequency of 0.3. The simulation took the first data point and calculated the rest of the aircraft's flight. Filtering the noise provided more accurate data for the simulation.

The application of a low pass filter on the data provided less noisy readings of the rates. The filter used a passband frequency of 0.3. Through iteration testing, 0.3 passband frequency provided a filter that did not cause too much delay or filter out important signal characteristics. In Figure 34, the original data starts at -0.8082 rad/s and the filtered data starts at -0.1704 rad.s. The original p value caused the aircraft to start in an uncontrollable roll. Since the simulation only used the first data point as input, filtering the data was necessary to eliminate noise and get a more accurate and representative starting point.

4.5.3 Data Conditioning: Aircraft Control Bias

The aircraft had inherent bias in the RC controls (aileron, elevator and rudder). With every aircraft, there are abnormalities to the controls from the structure. The controls had biases to compensate for abnormalities.

To eliminate the bias, the average values of the RC controls were statistically estimated. The bias calculation included multiple sections of the same flight to get the best estimate: all Pixhawk data from the flight, take off to landing, and three straight passes. All of the additional flight sections were included in the averaged bias for each segment. Table 6 show the biases of each control for all the segments. Table 7 shows the averaged bias of all the additional flight sections and its corresponding segment.

Table 6: The aircraft had a bias on the RC input. All of the average RC input for the aileron, elevator and rudder controls were calculated. The table shows the bias values for each segment.

Individual Averaged Bias			
	Aileron (deg)	Elevator (deg)	Rudder (deg)
Entire Flight	-0.6741	9.9128	-0.8475
Take Off to Landing	-0.7283	10.3882	-0.8547
Straight #1	-0.4971	10.0827	-0.8529
Straight #2	-0.124	9.9217	-0.8529
Straight #3	-0.4547	9.8639	-0.8384
Segment A	-1.070	9.8996	-0.8310
Segment B	-0.8925	9.8841	-0.8527
Segment C	-0.5945	10.3275	-0.8392
Segment D	-1.6747	10.6208	-0.8529

Table 7: The table shows the average of all of the additional flight sections with its respective segment from Table 6 for the aileron, elevator, and rudder. The average uses flight data outside of the Segments A-D to give a variety of controls in addition to the actual flight.

	Analyzed Flight Segments		
	Aileron (deg)	Elevator (deg)	Rudder (deg)
Segment A	-0.5915	10.0015	-0.8462
Segment B	-0.5618	10.0089	-0.8499
Segment C	-0.5121	10.0828	-0.8476
Segment D	-0.6922	10.1317	-0.8499

Tables 6 and 7 show a significant difference between the elevator bias compared to the aileron and rudder bias. To observe the bias effects, the bias of Segment C from Table 7 was removed and tested in the simulation. In the flight visual, the elevator bias caused the aircraft to pitch up/down too drastically and the flight became unstable. The flights were stable when only the aileron and rudder bias were removed.

Removing the bias changed all of the control input. The input could be different but needed to be similar enough where the new input did no harm to the original control input. To determine if the bias removal made a significant difference, there was statistical analysis completed. The statistical analysis was between the original control input and the control input without the bias. The original control input is the data directly from the Pixhawk. The control input without the bias removed the Segment C bias at each recorded time stamp.

The statistical analysis used the t-Test. The t-Test showed if the difference between means of the data sets was significant. There are three types of t-Test: independent samples, paired sample, and one sample. This thesis used independent samples because the test compares the means for two groups, original control input and the control input without the bias. However, the t-Test assumes that the variances of the data sets are equal.

To determine the variances for the data sets, the definitions of discrete random

variables were used [51]. The control input without the bias was found with

$$Y = X + C, \quad (7)$$

where Y is the control input without the bias, X is the original control input, and C is the bias which is constant. The data sets were stipulated to be independent even though they were linearly dependent. The expected value of Y provided the relationship

$$E[Y] = E[X] + E[C] \quad (8)$$

$$VAR[Y] = VAR[X] + VAR[C] \quad (9)$$

$$VAR[Y] = VAR[X] \quad (10)$$

because the variance of a constant is zero. The definitions of discrete random variables showed the variances of the two data sets were the same [51]. Because the variance of the original control input and control input without bias were the same, the t-Test could be used to test for differences between the means.

The test was only completed on the aileron and rudder data because the elevator bias caused unstable flight. Segment C data was analyzed for significant differences. The next section (t-Test) only have statistically analysis on Segment C.

4.5.3.1 t-Test

The t-Test showed how significant the differences were between the means of two data sets [51]. Segment C data was used for this analysis. The null (or hypothesis) was the mean of the original control input and control input with out bias were the same. To test if the means were the same, the t-Test calculated the t statistic to compare to the P value [51]. The P value is the actual probability that the t statistic falls within a certain percent of the data set. The test required the mean, standard

deviation, and number of data points to calculate the t statistic.

The average mean for the aileron and aileron without the bias were -0.5945 and -0.0824, respectively. The standard deviation was 0.3422 with 211 data points for both data sets.

The average mean for the rudder and rudder without the bias were -0.8392 and 0.0084, respectively. The standard deviation was 0.0218 with 211 data points for both data sets.

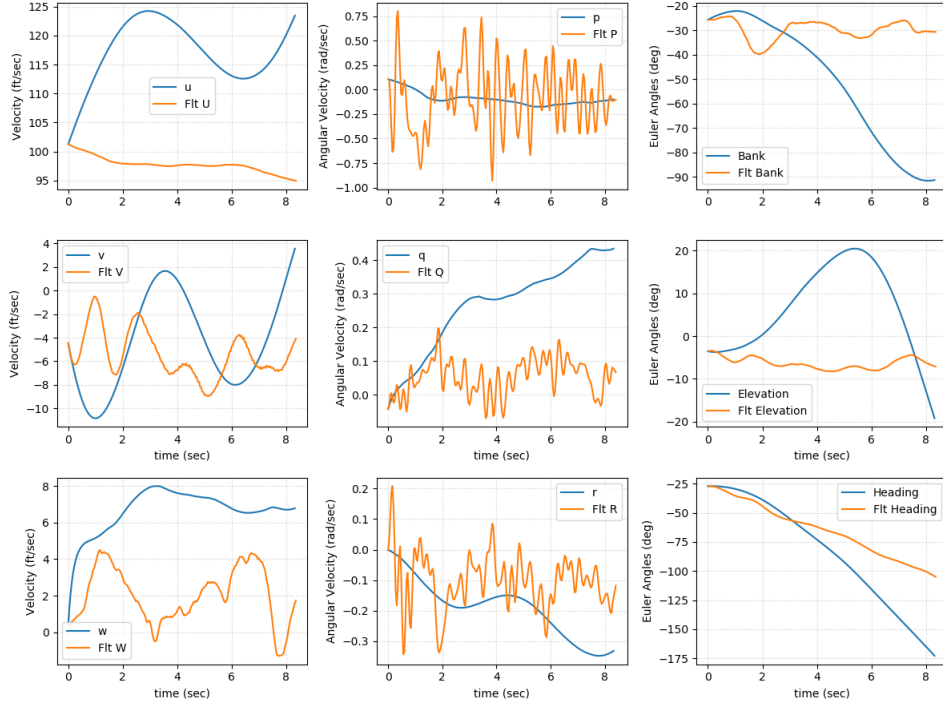
The t-Stat was calculated by [51]

$$t - Stat = \frac{\bar{x}_1 - \bar{x}_2}{\sqrt{\frac{\sigma_1^2}{n_1} + \frac{\sigma_2^2}{n_2}}} \quad (11)$$

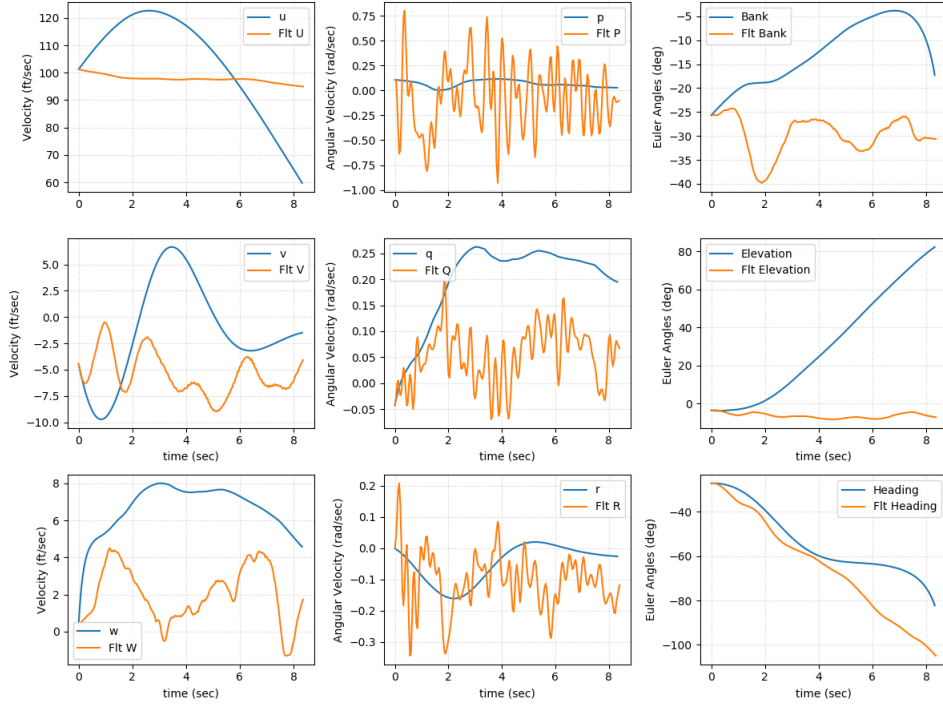
with a significance level of 0.05 ($\alpha = 0.05$). The calculation showed the T statistic was less than the P value. If the calculated t-Stat was less than the P value, then we fail to reject the null. Failing to reject the null means the hypothesis, the means of the original control input and control input without the bias were the same, was true. Therefore, the original data and the data without the bias had no significant difference. Because of these results, the other segments were analyzed. The t-stat was less than the P value across all the segment data.

t-Test proved there was no significant difference of the means of the two data sets. The control input without the bias could be used as an accurate reflection of the raw data because there was no significant difference. The input without bias would not harm the results of the true data. Because of the statistic results, the bias was removed in future analysis.

The simulation results were plotted to compare the difference with and without the bias. Figure 35 shows the comparison between the simulation results with original control input and the input without the bias.



(a)



(b)

Figure 35: Segment C data (blue = simulation, orange = actual flight). (a) shows the original RC input and (b) shows the bias removed from the RC control input. (b) shows closer trends in v , w , q , r , and ψ . Although the bias was less than 1° , the bias changed all of the flight states.

4.5.4 Thrust Model

In the original simulation, the thrust model caused u to increase drastically, and go well beyond the airspeed that was actually flown in flight testing. The fastest the aircraft flew during flight testing was about 100 ft/s and the simulation reached peaks of almost 200 ft/s. The original thrust model was incorrect. This section will discuss the original thrust model and how the simulation responded to the new thrust models.

The original thrust model was described as

$$T_{xb} = \tau \cdot \left(\frac{\rho}{\rho_{sealevel}} \right)^a \cdot (T_0 + T_1 V + T_2 V^2), \quad (12)$$

where $a = 1$, V is the normalized airspeed vector (ft/s), ρ is the density (slugs/ft³) at a given altitude, ρ_{SL} is the density (slugs/ft³) at a sea level, and τ is the throttle (unitless). T_0 , T_1 , and T_2 are constant values. The T constants directly affect the simulation through the following derivatives:

$$\dot{u} = \left(2 \cdot (e_x e_z - e_y e_\theta) + \frac{X + T_{xb}}{W} \right) \cdot g + r - qw, \quad (13)$$

where \dot{u} is the airspeed (ft/s), X is the forward motion coefficient, W is the weight (lbs) of the aircraft, g is gravity (ft/s²), w is a velocity (ft/s), r , and q are angular velocities (rad/s), and e_x , e_y , e_z and e_θ are the quaternions (rad).

There were three thrust models tested in the simulation. One model was derived from the least squares approach [52] and two models were from a static approach. The least squares approach manipulated the thrust model from (20) and (13) in the original simulation. There were two designs from the least squares approach. The static approach used the relationship between the throttle and thrust from the MotorCalc program [53] and actual test data.

4.5.4.1 Least Squares Approach: Design I

The first thrust design focused on changing the constant T values using the least squares approach. The least squares approach is described by (14) [52].

$$Y = \Phi\theta. \quad (14)$$

Because time and order does not matter, weighted least squares was used. In this case, $\theta = [T_0; T_1; T_2]$. Therefore, Y would be an $nx1$ matrix and $\Phi = [1VV2; \dots]$ was an $nx3$ matrix. Airspeed \dot{u} is proportional to T_{xb} . \dot{u} was described as

$$\dot{u} \sim \frac{X + Txb}{W} \cdot g. \quad (15)$$

Therefore, Txb can be written as

$$Txb \sim \frac{\dot{u} \cdot W}{g} - X. \quad (16)$$

We assumed that X is small for the purposes of estimating T_{xb} . In the original thrust model, X was the forward motion coefficient. (17) shows the modified version for the Design I.

$$Y = \left(\frac{Txb}{\tau} \right) \left(\frac{\rho_{SL}}{\rho} \right) = \left(\frac{uW}{g\tau} \right) \left(\frac{\rho_{SL}}{\rho} \right) \quad (17)$$

After calculating Y , θ can be found using [52]

$$\theta = (\Phi^T \Phi)^{-1} \Phi^T Y. \quad (18)$$

4.5.4.2 Least Squares Approach: Design II

Throttle inputs of zero caused an issue with Design I. τ was in the denominator of Design I and therefore forced Y to infinity. Another model was created using the least squares approach: Design II. In Design II, the constants in (17) were transferred to (14). Design II is described as:

$$Y = \Phi\theta \cdot \left(\frac{\tau g \rho}{W \rho_{sl}} \right). \quad (19)$$

The variables in Equation 19 are the same as described in Section 4.5.4.1. Design II eliminated the issue of having τ in the denominator.

4.5.4.3 Least Squares Approach: Design I vs Design II

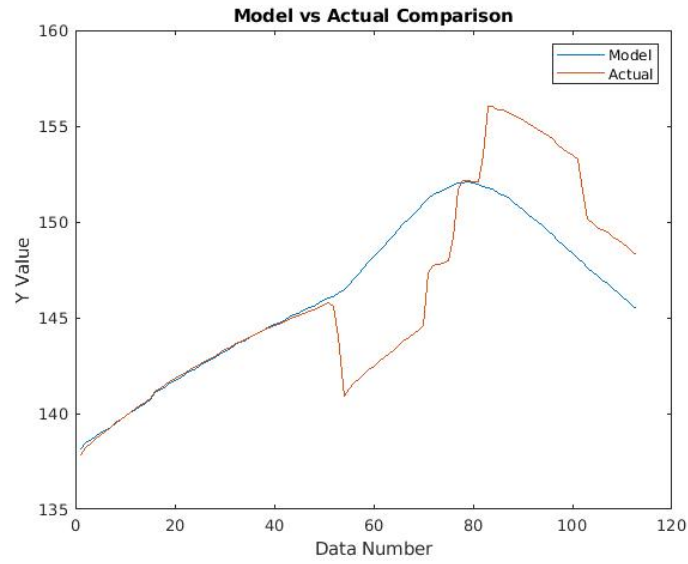
Design I and II were tested on all of the flight segments. The simulation results were compared to the flight test results to find the best model. The results are shown in Table 8.

Table 8: Design I and II produced different T constants. The highlighted constants were the best performing thrust models. The rest of the models had unstable flights in the simulation.

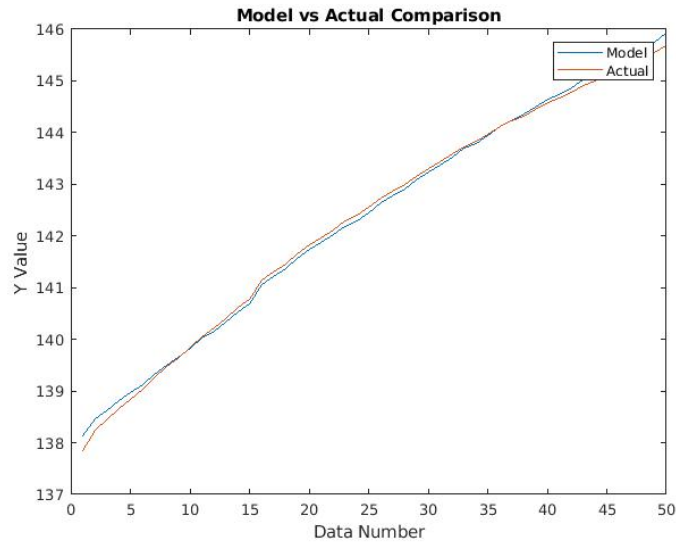
		Take Off to Landing	Segment A	Segment B	Segment C	Segment D
Design I	T0	-0.2781	489.8835	-205.1880	7190.9687	33.5422
	T1	1.3091	-7.4637	5.4134	-140.4885	0.3845
	T2	-0.0018	0.0388	-0.0211	0.7000	0.0060
Design II	T0	0.0227	6.3030	40.7336	118.2083	-27.6476
	T1	0.0002	0.2653	-0.0505	-0.3771	0.0492
	T2	0.0000	0.0087	0.0082	0.0082	0.0224

The highlighted models in Table 8 resulted in a stable performing flight on the flight visual. Regardless of the model performance, each of the flight segments were analyzed further for Y relationships, described in (14) and (17). The thrust model was analyzed between the actual (14) and model (17) design. The analysis showed

that there are parts of the model that work better at specific times. Figure 36 shows the relationship between the actual data and the simulated model performance.



(a)



(b)

Figure 36: The figure shows the Design I: Segment A's thrust model. (a) shows the entire flight segment data. (b) shows the trimmed data from 0 to 50. The trimmed data can produce another thrust model of T constants that will be more closely correlated.

After reviewing the correlations of the models, all of the coefficients computed with Design II were proven to be invalid. However, Design I had three closely matched Y relationships. Because of this, another iteration of the model was done on the closely related Y segments of flight shown in Table 9.

Table 9: The models that had closely matched Y relationships were put through another iteration of the least squares thrust approach. The model and actual data were compared through the entire data set. The highlighted model shows the best performing model. However, the simulation performed best when the values were inverted.

		Take Off to Landing: Trimmed(8700:end)	Segment A: Trimmed(1:50)	Segment C: Trimmed(1:100)
Design I	T0	94.4014	-17.0633	-6193.8251
	T1	-0.7880	1.5393	127.0050
	T2	0.0096	-0.0011	-0.6364

Table 9 highlights the only working model from trimmed data. While testing the highlighted model, the aircraft behaved opposite than expected. To counteract the behavior, the T values were inverted. The inverted model displayed a flight closer to the actual flight in the flight visual.

To find the best least squares approach, all of the highlighted models were tested on the flight segments. The highlighted models were also compared against the original model that USU Aero Lab created. Although Design I: Segment C had a working performance, the trimmed Y relationship provided a better performance. Design I: Segment C (trimmed) was used for further analysis. The working models are shown in Table 10.

Table 10: There were three least square models that performed well against the respective flight. To find the best model, each of the models was simulated with all of four segments.

	Original	Design I: Segment A	Design I: Segment C (1:100)
T0	28.8000	-205.1880	6193.8251
T1	0.1263	5.4134	-127.0050
T2	-0.0022	-0.0211	0.6364

The best least squares approach was found by comparing the three models on each segment. The best model was the one that had the closest simulation output to the actual flight data. Some of the comparisons are shown in Figures 37-39. All of the figures show the results against Segment C.

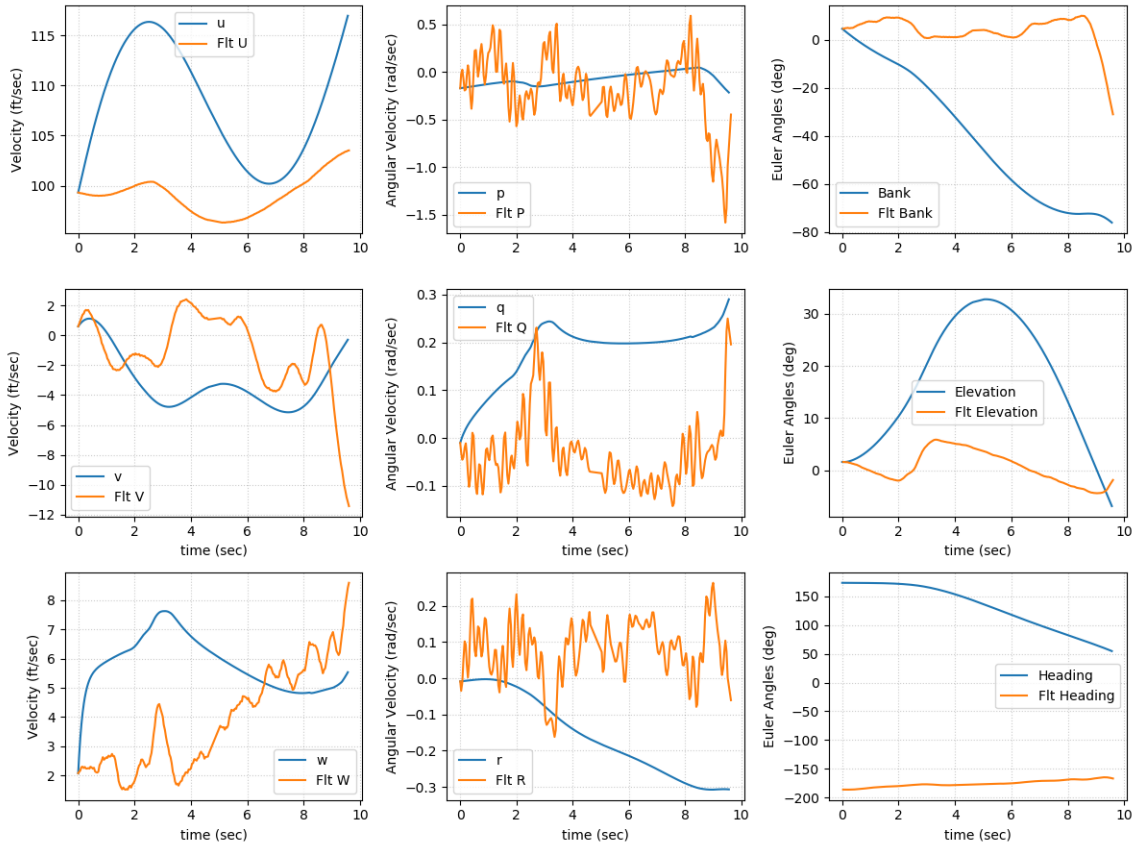


Figure 37: The simulation results used the original T constants ($T0 = 28.8$, $T1 = 0.1263$, $T2 = -0.0022$) on the Segment C flight. There are trends for p , q and some of ψ .

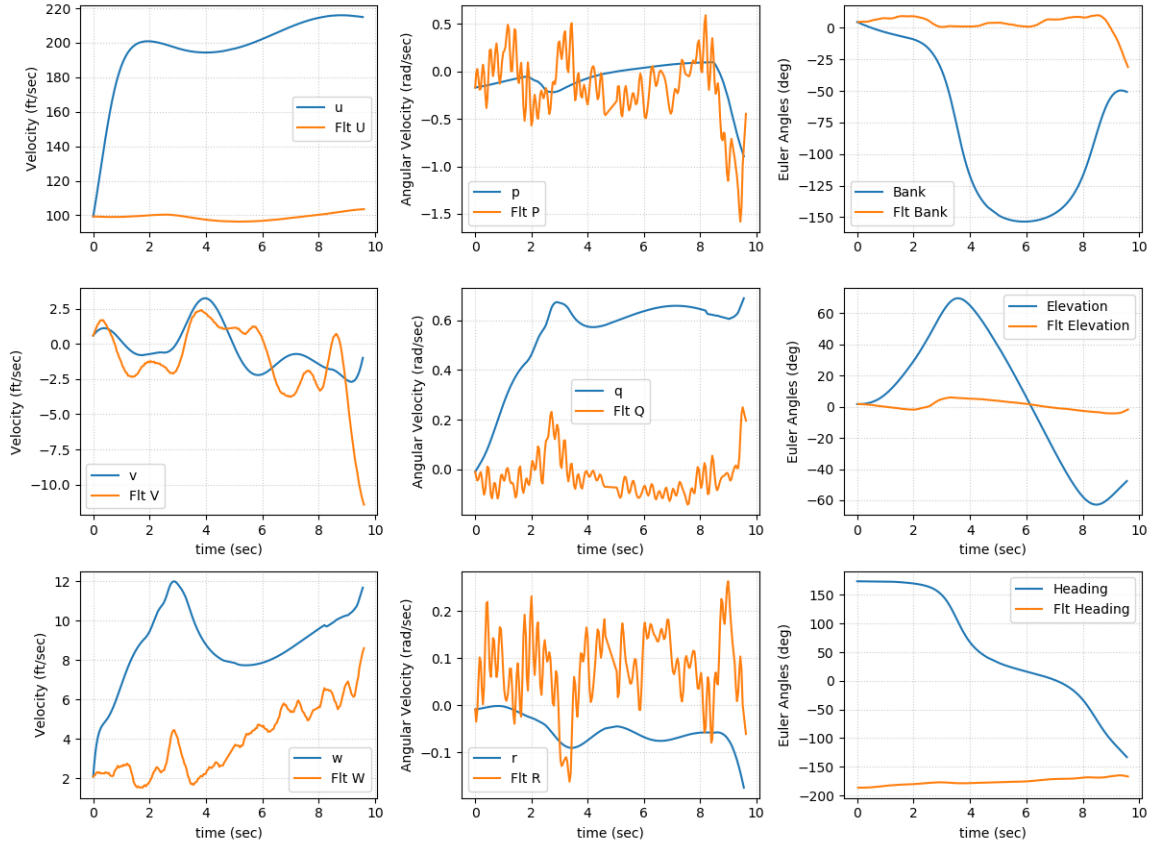


Figure 38: The simulation results used the trimmed Segment A (1:50) T constants ($T0 = -205.1880$, $T1 = 5.4134$, $T2 = -0.0211$). The model was used on the Segment C flight. There are trends in v , p , and r .

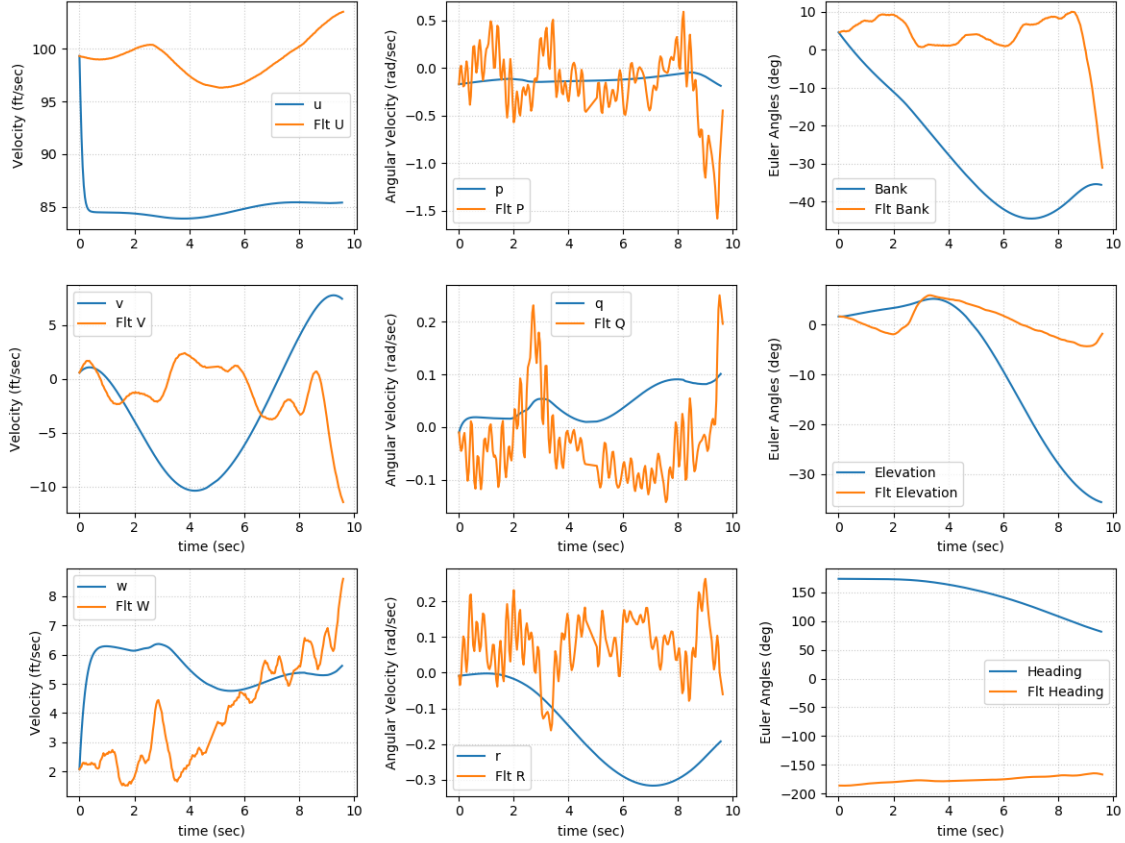


Figure 39: The simulation results used the trimmed Segment C (1:100) T constants ($T0 = 6193.8251$, $T1 = -127.0050$, $T2 = 0.6364$). The model was used on the Segment C flight. There are trends in w , q , and r . There are similar trends on half of the data for the θ and ψ .

After all comparisons, the best performing least squares approach was the Design I: Segment C (1:100) model (refer to Figure 39). However, the models in general, did not fit the data well. This thesis needed other methods to find an appropriate thrust model.

4.5.4.4 Static Approach: MotorCalc Model

This thesis attempted to develop a thrust model using static thrust data. It is important to note that the static data is not a great fit for a moving vehicle but the approach provided more insight to the throttle vs thrust relationship. The static test

used the MotorCalc program [53].

MotorCalc used the propeller dimensions, wing dimensions, weight of the aircraft, and motor specifications to return flight performance. The flight performance had data points for the throttle input at every 10% from 0-100%. Figure 40 shows the given relationship between the throttle, propeller rotation rate and thrust.

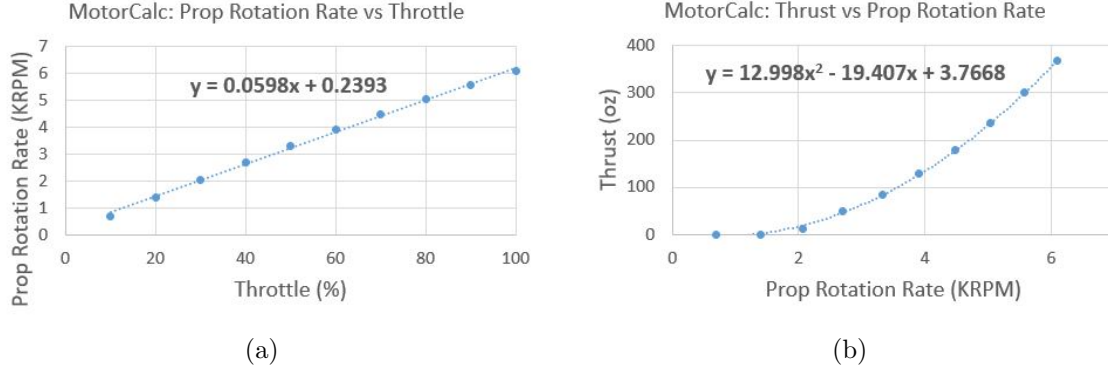


Figure 40: The graphs show the relationship between the throttle, propeller rotation rate and thrust. With these two equations, there was a direct relationship between the throttle and thrust. The simulation provided the throttle input and this model provides one value for the thrust found in (20).

Figure 40 illustrates the MotorCalc thrust model in (20) described as:

$$T = 465.00024\tau^2 - 78.86904\tau - 0.13297, \quad (20)$$

where T = thrust (oz) and τ = throttle (%). The model did not convert the units to lbs-force to work with the simulation. The conversion was calculated in the simulation itself.

4.5.4.5 Static Approach: VCCW Model

The MotorCalc website is based on theoretical and tabular data. To validate the data, additional test were performed. The test gathered thrust data from the vehicle itself.

The aircraft was connected to a push-pull gauge to measure the thrust force exerted from the aircraft. The test was able to provide a direct relationship between the throttle and thrust.

The recorded throttle PWM values from the flight ranged between 1187-1769. To get a good range of data, there were 11 data points to approximate 0-100% throttle in 10% increments. Figure 41 shows the data collection and relationship between the throttle and thrust.

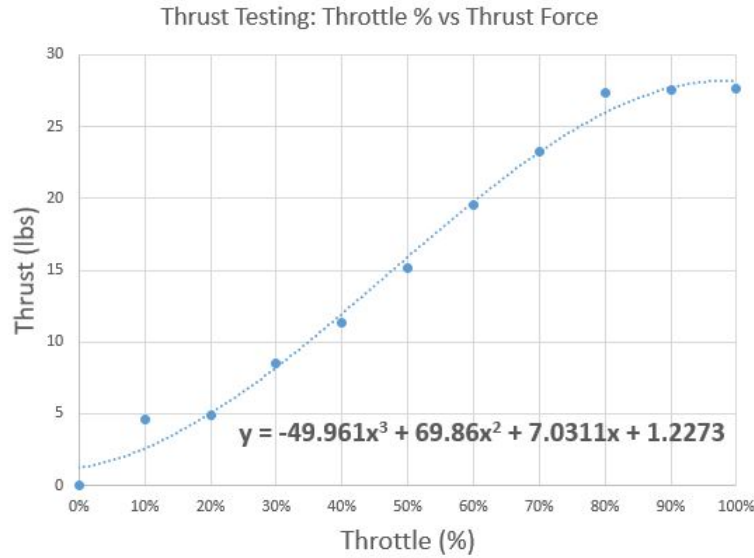


Figure 41: The graph shows the relationship between the throttle and the thrust of the VCCW aircraft. The thrust peaks around 80-100% throttle.

The VCCW thrust model is

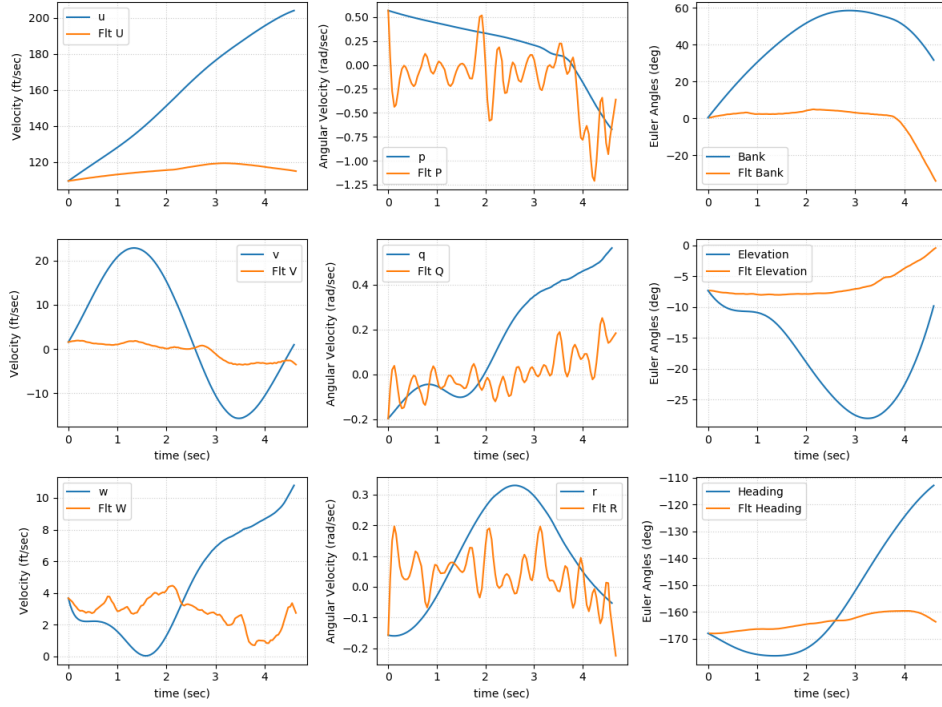
$$T = -49.961\tau^3 + 69.86\tau^2 + 7.0311\tau + 1.2273, \quad (21)$$

where T = thrust (lbs) and τ = throttle (%).

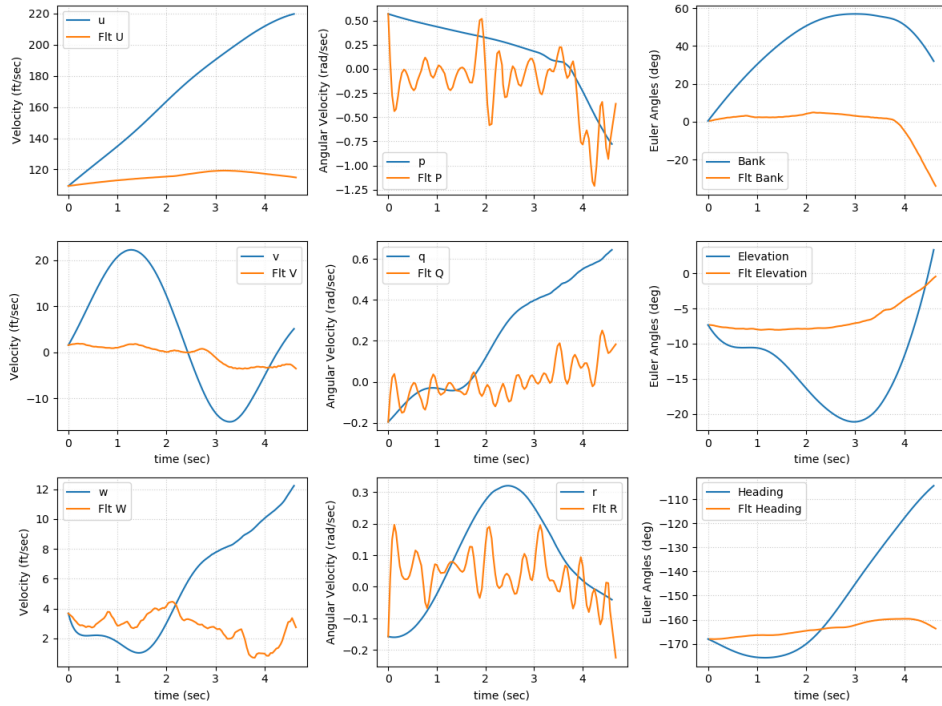
4.5.4.6 Static Approach: MotorCalc vs VCCW

The two static models were compared. Figures 40 and 41 show a difference in the shape of the trend line. Figure 40 (MotorCalc) shows a slow increase at minimal throttle input then increases as with more throttle input. The VCCW model has the same trend at minimal throttle input but then peaks around 80% throttle and remains around the same thrust.

Despite the small difference, the two models were expected to have similar results. The MotoCalc model was created from the same parameters as the actual flight test. Figures 42-45 show the comparison between the two static models.

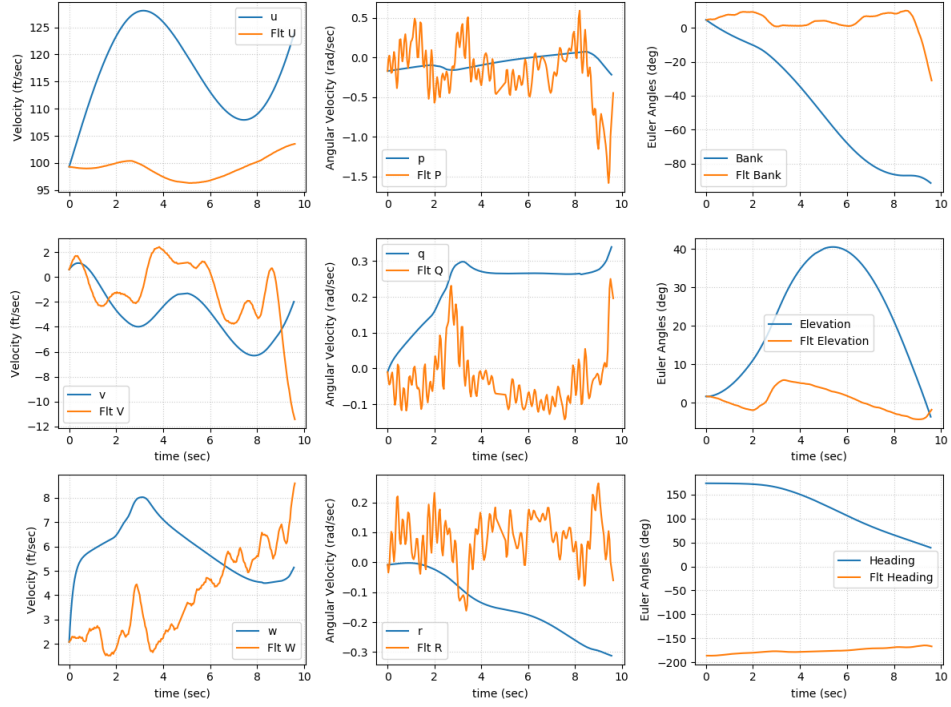


(a)

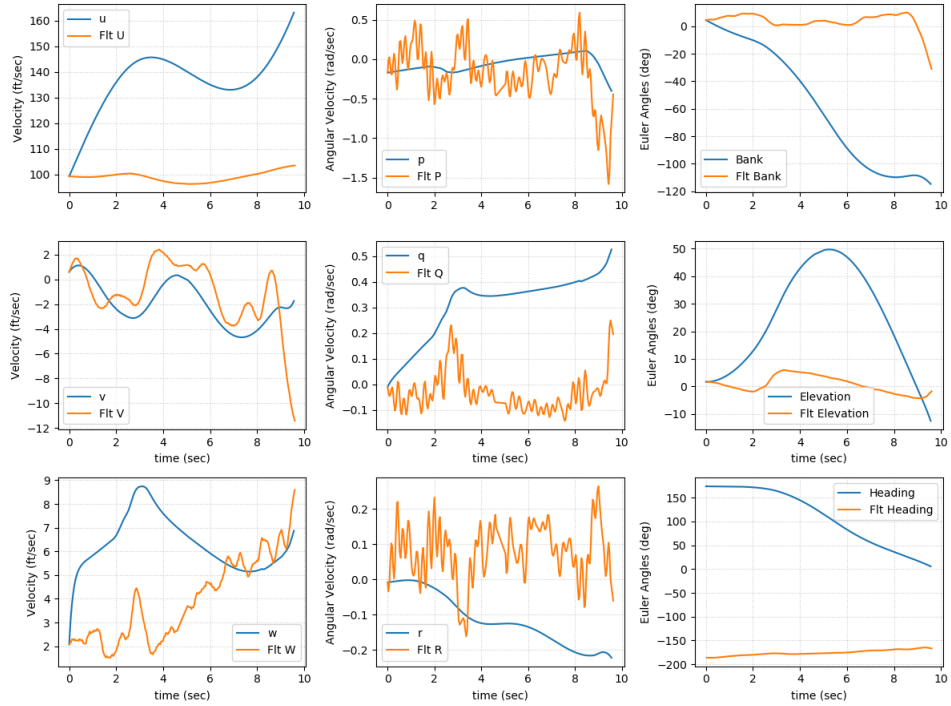


(b)

Figure 42: (a) shows the MotorCalc model and (b) shows the VCCW model on Segment A. The results are almost identical. In the VCCW model, the u and w velocity is a little faster.

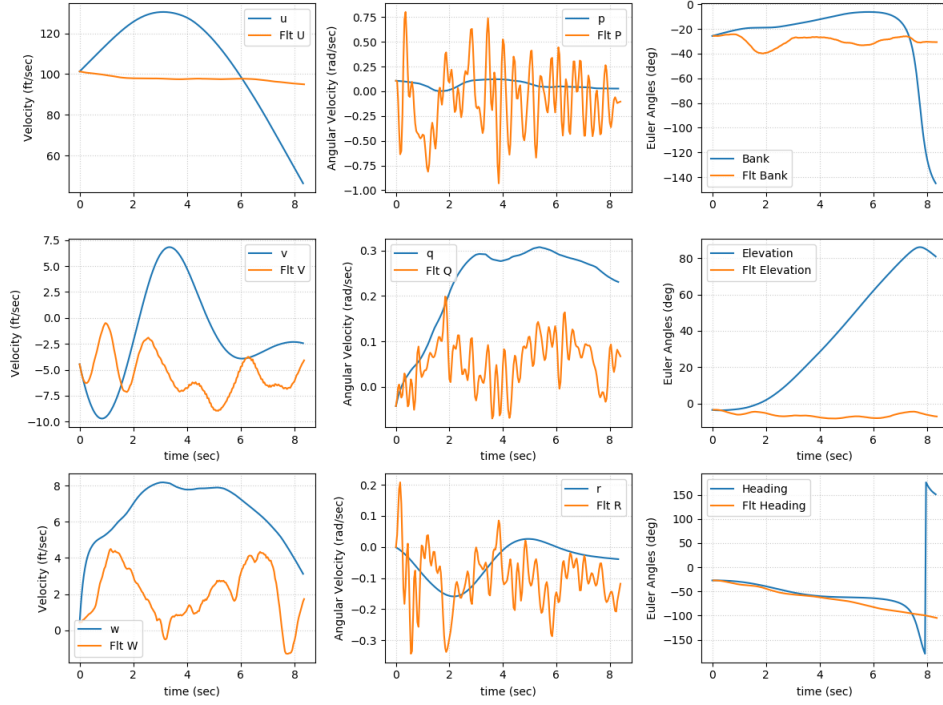


(a)

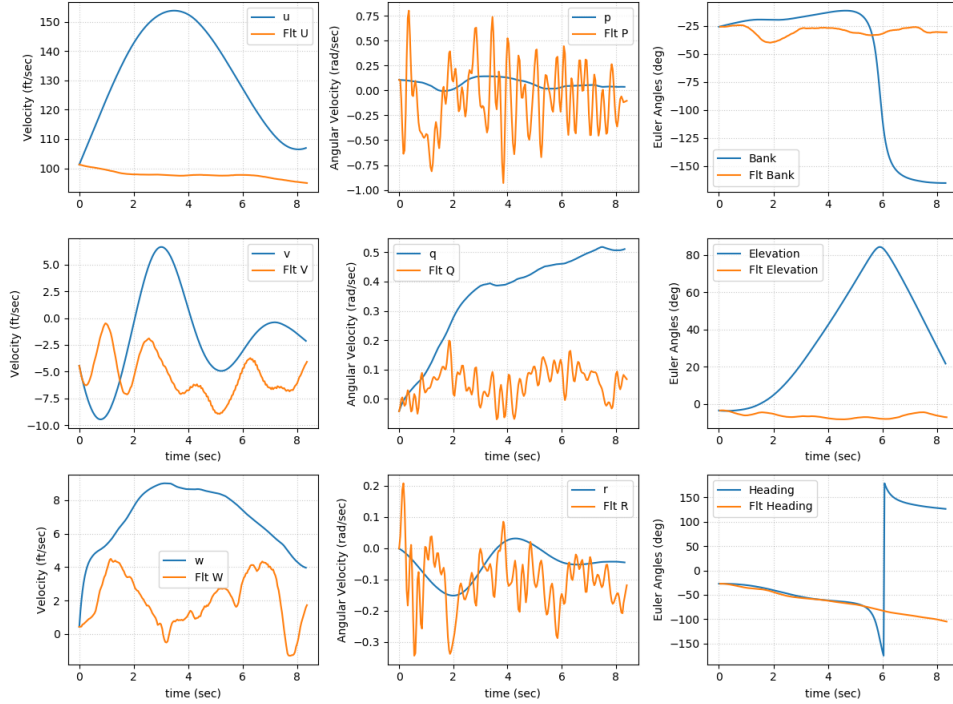


(b)

Figure 43: (a) shows the MotorCalc model and (b) shows the VCCW model on Segment B. The results are almost identical. The VCCW model is a little faster and the Euler angles are more drastic.

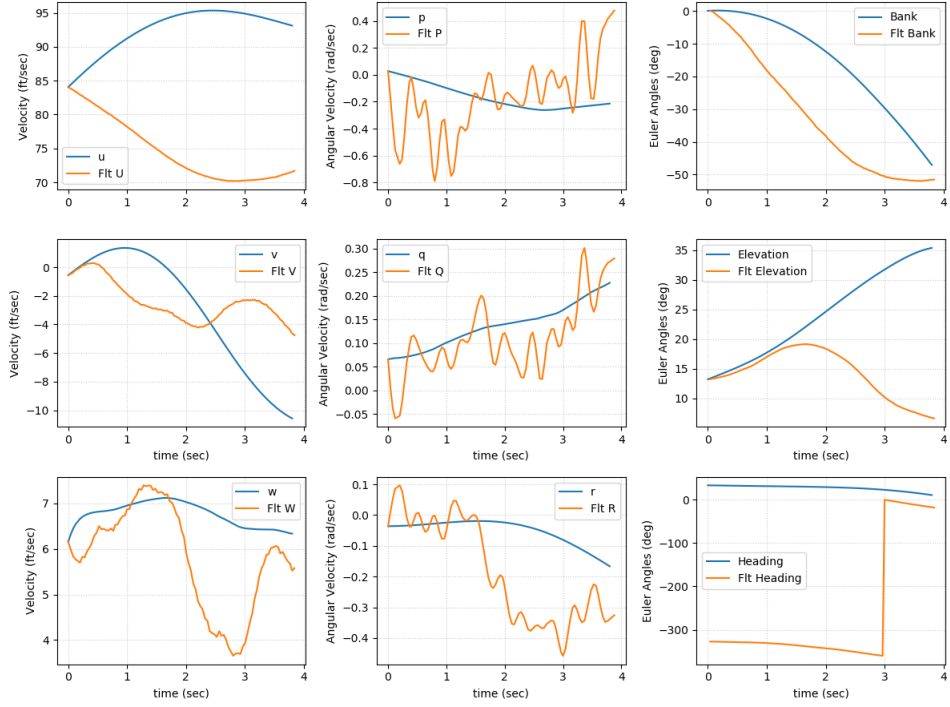


(a)

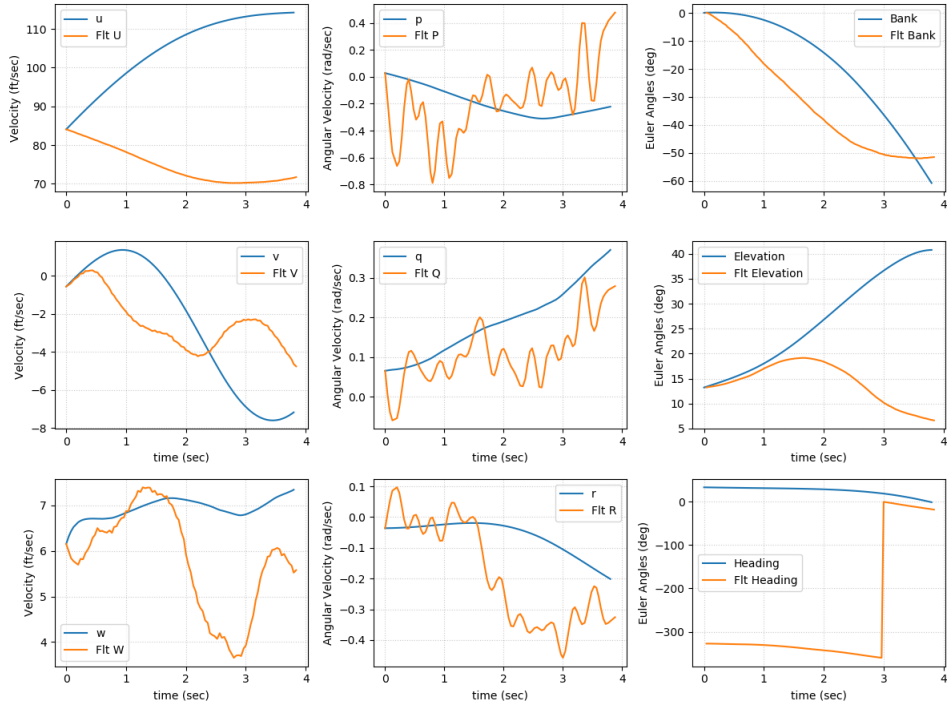


(b)

Figure 44: (a) shows the MotorCalc model and (b) shows the VCCW model on Segment C. There are a lot of the same trends. However, the VCCW model has results closer to the actual flight test.



(a)



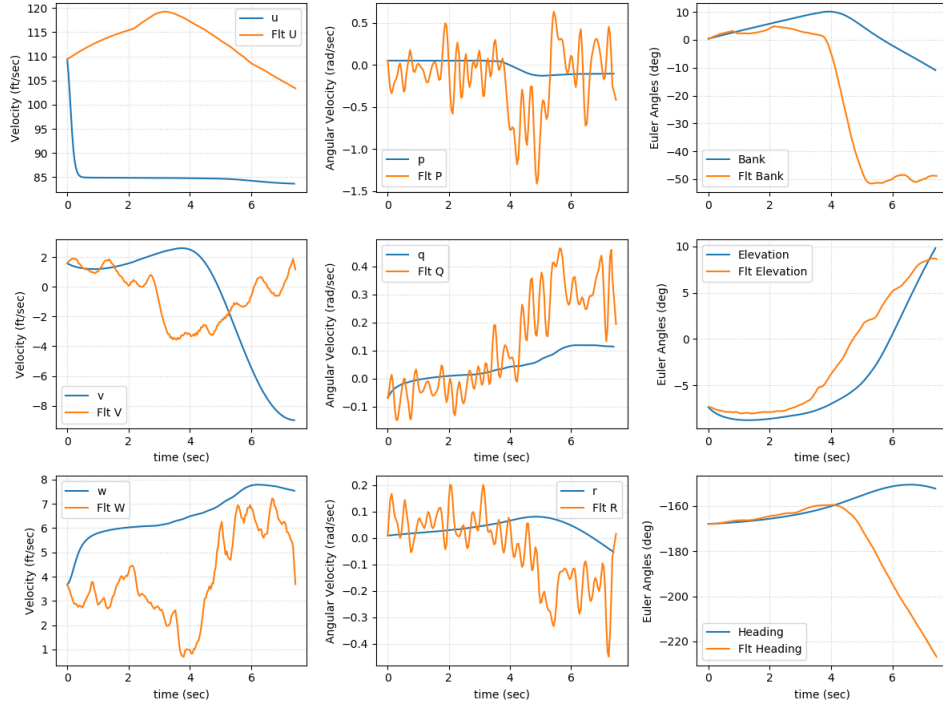
(b)

Figure 45: (a) shows the MotorCalc model and (b) shows the VCCW model on Segment D. The results are almost identical. The u and w velocity are faster in the VCCW model.

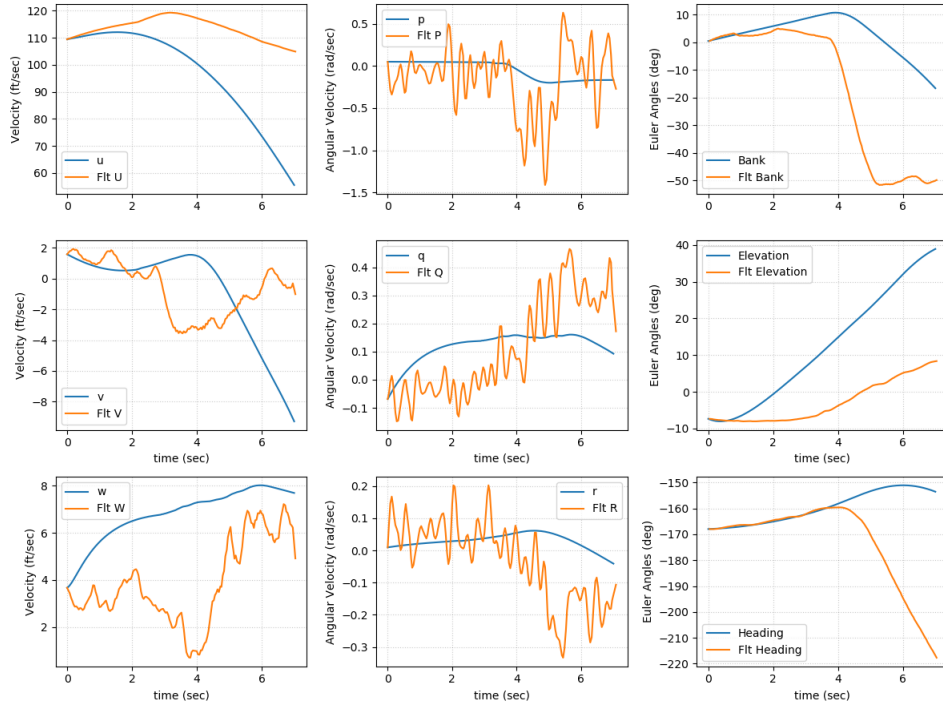
As expected, the results for the MotorCalc and VCCW models were very similar. The VCCW model results also provided verification that the MotoCalc model was close to the actual hardware. Looking at the model comparison, the most noticeable difference was the velocity range. The velocity range in the MotoCalc model was closer than the VCCW model. Therefore, the MotorCalc model was the better static thrust model.

4.5.4.7 Final Thrust Model Comparisons

Design I: Segment C was the best thrust model from the least squares approach. MotorCalc model was the best thrust model from the static approach. The flight segments were lengthen to give a better comparison of trends. All of the comparisons included the angular rate filtering and aileron and rudder bias removal. Figures 46-49 show the flight states results of the simulation and actual flight data.

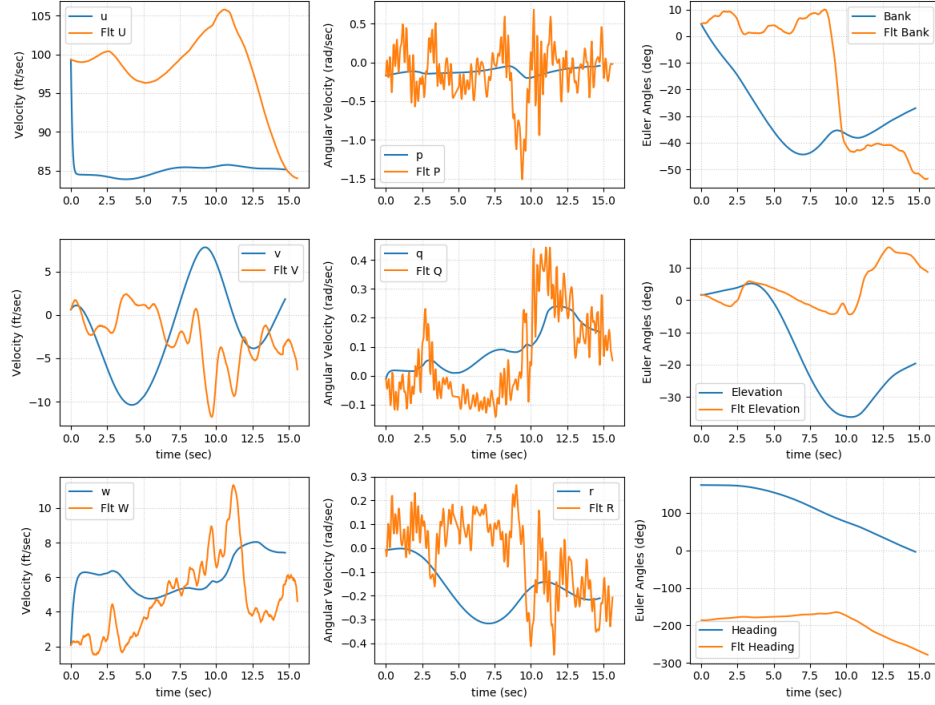


(a)

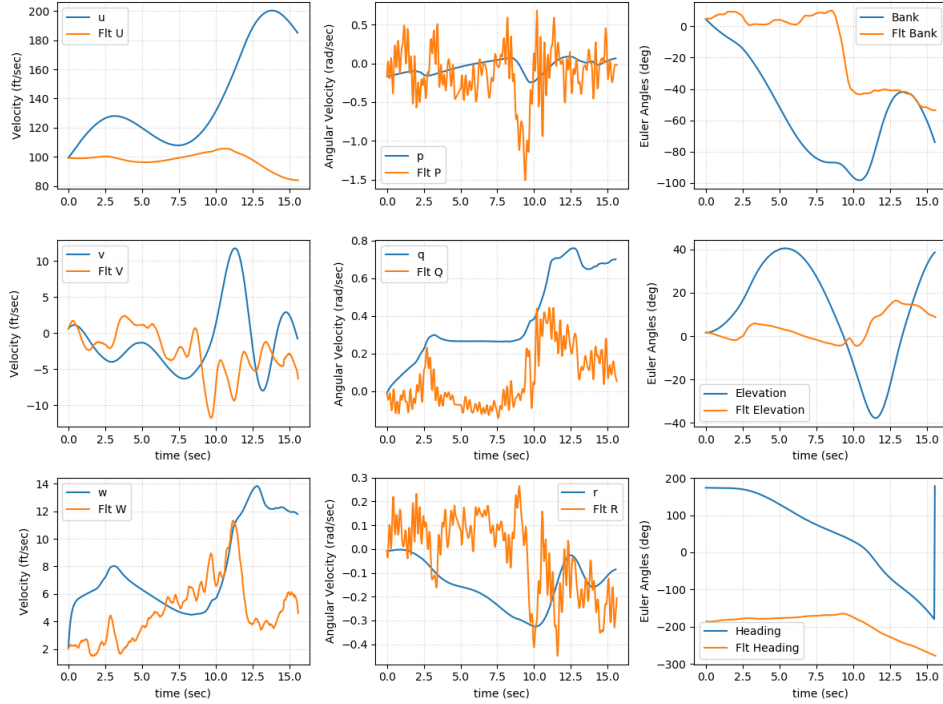


(b)

Figure 46: (a) shows the least squares model and (b) shows the static model on Segment A. There are similar characteristic trends for v , w , p , q , r , ϕ and ψ .

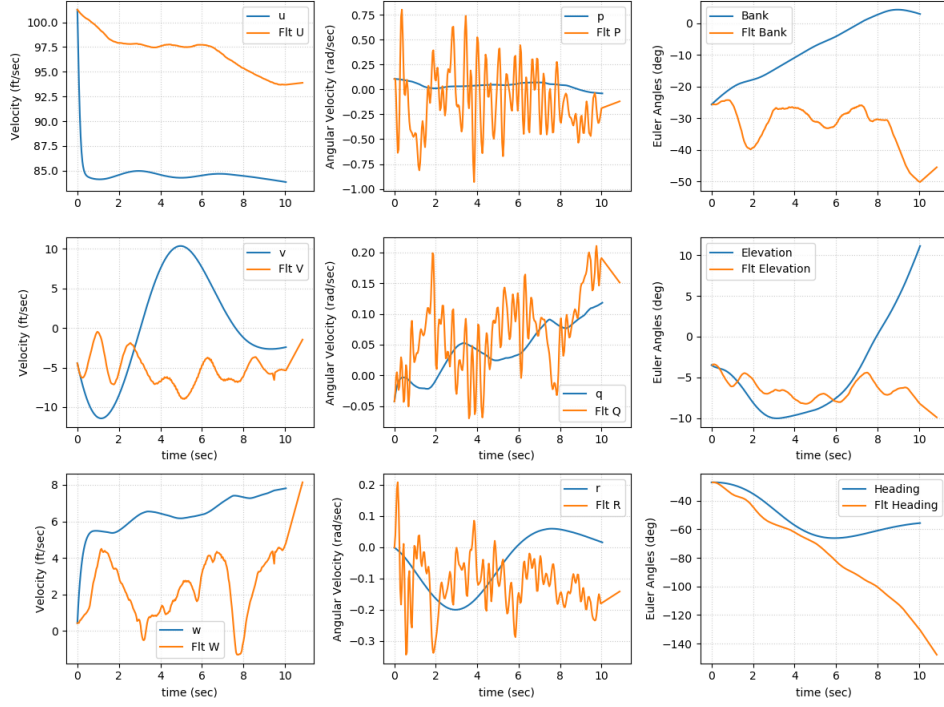


(a)

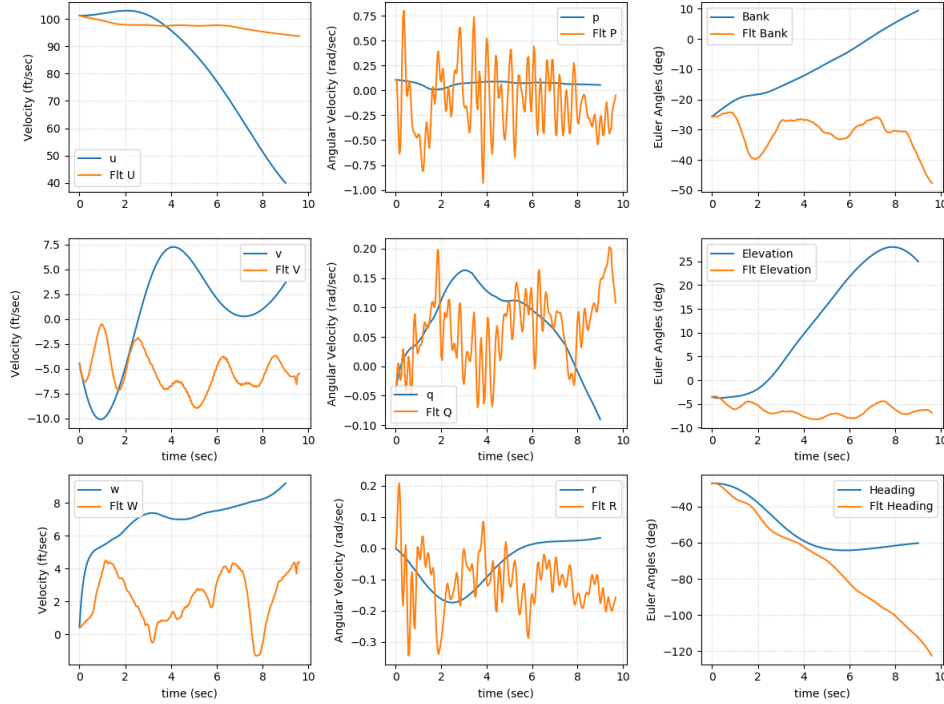


(b)

Figure 47: (a) shows the least squares model and (b) shows the static model on Segment B. There are similar characteristic trends for p and r .

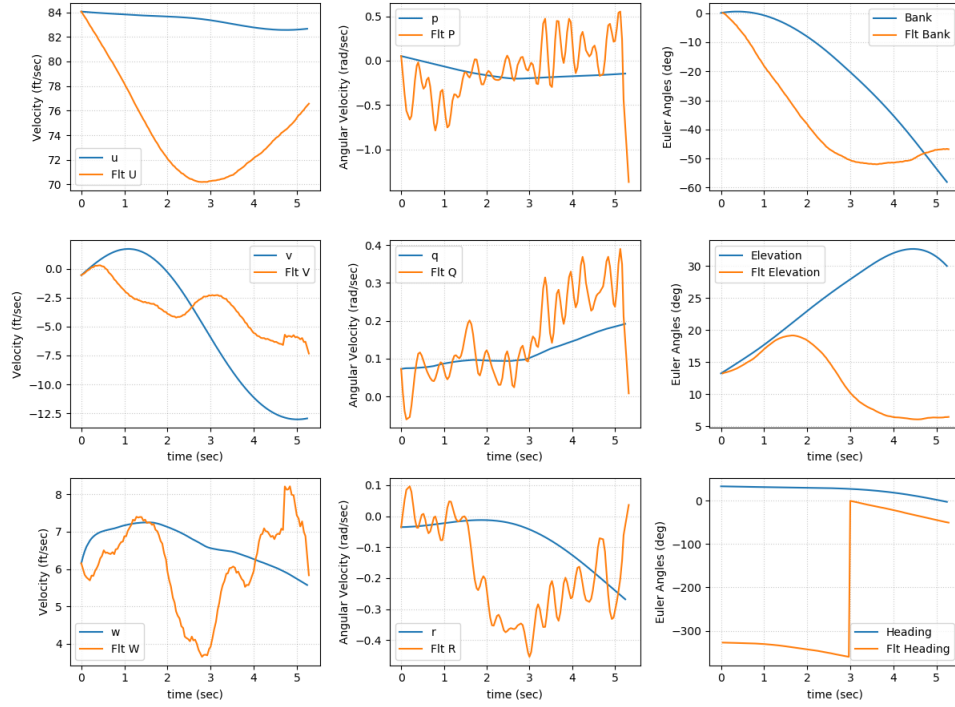


(a)

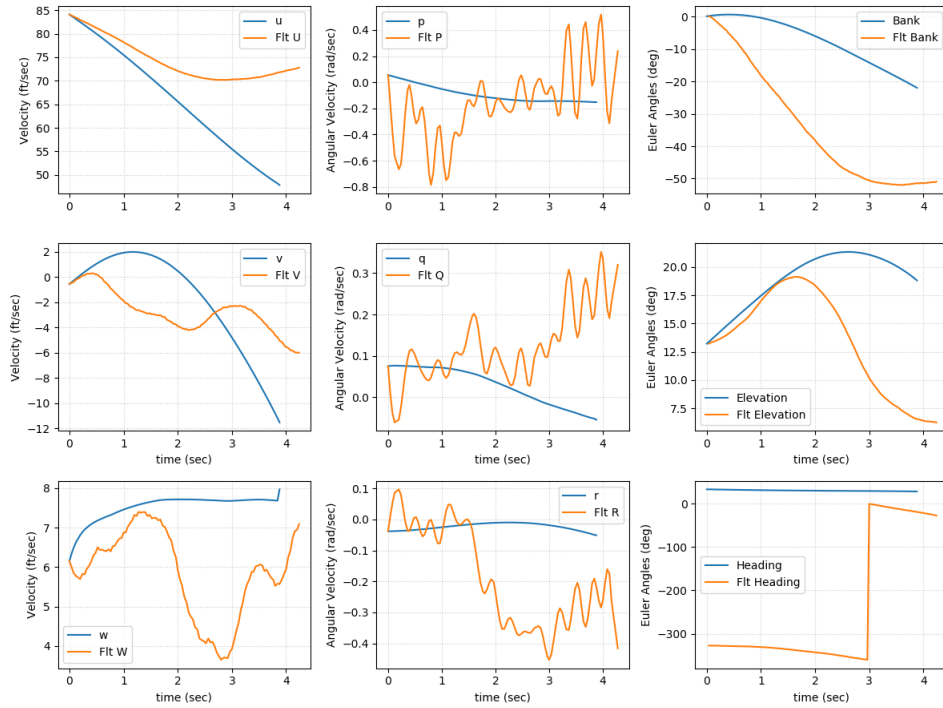


(b)

Figure 48: (a) shows the least squares model and (b) shows the static model on Segment C. There are similar characteristic trends for v , w , p , r , ϕ and ψ .



(a)



(b)

Figure 49: (a) shows the least squares model and (b) shows the static model on Segment D. There are similar characteristic trends for v , θ , and ψ .

In this comparison, the least squares thrust model and the static thrust model each performed to some degree in two of the four segments. The static thrust model was better in Segment A and D, while the least squares thrust model was better in Segments B and C. The heavily weighed flight states are u and θ . The simulation was most closely trending in the static models for Segment A and D (Figures 46(b) and 49(b)). Therefore, the static model was the best thrust model for the simulation. The overall best performing model was the MotorCalc static thrust model. However, it was still an inadequate model to completely describe what is going on.

4.5.4.8 Simulation Conclusion

The flight data was analyzed in four segments with the wind and along the cross-wind. To improve the performance, the simulation tuned the filtering, bias removal and thrust model.

Data filtering for the angular rates was necessary for the simulation. Angular rate collections were very noisy. Filtering helped smooth the data and provide improved rates. Since the simulation relied on an accurate initial state, it was vital that this data was as accurate as possible.

According to the statistical test on the control bias, there was no significant difference in the mean of the control sets. Therefore, the bias removal would not harm the results from the raw data. The simulation performance improved without the bias (refer to Figure 35). Removing the bias changed all of the flight states and improved the simulation performance. The bias was removed from the control input for the rest of the analysis.

The thrust model improved all of the flight states compared to the original model. The MotorCalc static thrust model was the best performer. u and θ states were weighted heavier than the others. These were the states most difficult to match and

affected the flight the most. In the end, the implementation of the static model, the filtering of the data, and making appropriate bias corrections demonstrated an improvement to the simulator (refer to Appendix C Figures 62 - 65). However, it is clear that more work is needed to provide a thrust model that is accurate. A more complicated, nonlinear estimation approach will be required to find a model that is ultimately, satisfactory.

4.6 Results and Analysis Summary

Chapter IV discussed the results of the bi-filar testing, flight testing, and simulation performance. The bi-filar test results showed the MOI measurement was likely near only 1% error, based off the validation test. The flight testing was successful! Flight analysis showed that the VCCW had more roll authority than the base wing. The VCCW was a successful design that demonstrated the possibility of morphing flight.

The simulation results were analyzed and compared to the flight data then the parameters were tuned to get the simulator performing closer to the actual flight test. The best simulation results came from filtering the angular rates, removing the aileron and rudder bias, and using the MotorCalc static thrust model. However, it is clear that a linear or second order polynomial model is insufficient to accurately modeling the effects of the motor-propeller relationship. More work is needed to identify an adequate model to improve the simulation.

V. Conclusions

This chapter will discuss the research conclusion and significance of the work. There are suggestions for future work based on what was completed and for new directions. The chapter closes with an overall conclusion of this thesis.

5.1 Research Conclusion

The problem statements for this research were 1) Is the variable camber compliant wing (VCCW) capable of equilibrium flight involving various maneuvers without sustaining damage? and 2) Is it possible to create a flight simulation that aligns with the actual flight test data?

This thesis answered both problem statements. The flight test demonstrated that the VCCW was capable of performing various maneuvers and to maintain stable flight. There was no damage to the wing after all of the flight testing. Aligning the flight test data and the simulation proved to be a challenge. The simulation will need further work, as is discussed in Section 5.2.

To answer the problem statements, this thesis incorporated various testing and analysis of data. Bi-filar pendulum testing, flight tests, data analysis, and simulation refinement were key aspects of the research.

The first part of the research was the bi-filar pendulum test. The bi-filar pendulum test results provided the only known moment of inertia (MOI) measurement for the base wing and the VCCW. The test had less than a 1% error and therefore, had high confidence of accuracy.

The second part of the research was flight testing. Flight testing for the base wing and VCCW provided data collection on the aircraft's performance. The VCCW completed successful flights that demonstrated the roll and yaw capabilities of the

wing. The research benefited from my role as co-test director. The test director led all operations of flight test to include safety, flight missions, flight execution, and data collection. This role was essential for the data collection for this research, AFRL and USU Aero Lab's work.

The third part of the research was analyzing the flight test data. Data analysis helped understand the morphing capabilities and provided the proper conversions of data for the simulation input. The analysis showed the VCCW roll control had more authority than the base wing!

The last part of the research was simulation refinement. Data analysis tuning was essential to provide the best input for the simulation. The simulator underwent tuning of the input parameters and thrust models. There were two types thrust approaches tested in the simulation and compared to the output: least squares approach and static thrust approach. The simulation work did improve the comparison of the simulation and flight test data, however it was insufficient to closely match the flight data. The current work could be used to establish a baseline for prototypes prior to flight test.

5.2 Future Work

There are many parts of the thesis that can be improved to provide better results and expand other possible research opportunities. The bi-filar pendulum test, flight testing, and simulation refinement are all considered for future work.

5.2.1 Bi-Filar Pendulum Test Improvement

The bi-filar pendulum test provided the MOI measurement for the base wing and VCCW. The base wing yaw MOI could be remeasured to provide a more accurate measurement. The entire test could also be redone with a different mounting process

to improve the measurement.

A more accurate MOI could improve the simulation performance. The base wing yaw data collection had a high standard deviation with the three filar length measurements. The base wing yaw MOI should be measured again to get a more accurate measurement.

Remeasuring the MOI using different methods can improve the output of the simulation. When the fuselage is no longer needed, the filar from the bi-filar pendulum experiment can be mounted directly through the CG. Mounting the aircraft through the CG would eliminate the need for the parallel-axis theorem. Although the test result error is low, the procedure change could make the results more accurate.

5.2.2 Flight Test Improvement

Flight testing demonstrated the capabilities of the VCCW. Testing could be improved with more thorough data collections and scheduling.

Flight testing could be improved by having a more thorough data collection. Wind data collection only happened at the beginning of the flight. The test team had the resources and tools to provide wind readings throughout the flight. Having wind data provides better insight when analyzing the flight test data.

Although time is difficult to control, scheduling could be improve the control of time. Flight test data changes with temperature. Scheduling the flight tests around the same time of the year would make the flight test data more consistent. There was about a 10-20°F difference from the VCCW testing.

As one of the test directors, I would change the flight test crew assignments. I had to verbally call out all of the test data points while recording the time of flight and maneuver. I had to look at the next data point, call out the test point, and record the flight maneuver details simultaneously. There should be an additional data recorder

on the ground to eliminate recording error.

5.2.3 Simulation Improvement

The simulation results in Section 4.5.4.6 show there is room for improvement to match the actual flight data more closely. Many different aspects can be tuned to improve simulation performance.

An accurate wind representation in the simulation would improve the performance. The measurement for wind speed comes from the Pixhawk. The Pixhawk also provides the wind speed in the north and east position. However, the measurement lacks accuracy in direction and actual speed in comparison to online weather sources. Accurate wind speed and heading would improve simulation calculations of airspeed and ground speed and more help to closely match actual flight data.

The thrust model will need to be changed completely. There are many studies on thrust models and different methods to determine the thrust of an aircraft [54][55][56]. Most of these studies use the actual value of the coefficients to find a thrust model. Collecting more data would provide the potential for various thrust models.

Another thrust model could come from a system identification approach. The system ID could also focus on the stability calculations. The work can compare the stability calculations between the simulation and flight test to find the differences.

The simulation can also be developed to work with the base wing and all four modes. This capability would be essential for future flights with Mode 4. Because Mode 4's capabilities did not perform as expected, the simulation could help predicts its capabilities without going to flight test. Having the ability to change through all modes and different wings would make the simulation multi-functional and a vital assets to the VCCW research.

5.3 Thesis Conclusion

Morphing wing technology is changing the way aircraft are controlled. The technology is also providing many different ideas to improve the performance of an aircraft. The VCCW is a non-stretch, single, continuous wing that changes the camber of the wing to control roll and eliminates ailerons and flaps.

The VCCW was successful in demonstrating roll and yaw control capabilities. The VCCW flight test provided data for many different venues. The data benefited this thesis work, AFRL, and the USU Aero Lab. This thesis attempted to use the data to help improve USU Aero Lab's simulation.

This thesis work contributed to the camber morphing development through flight testing and data collection. All of the work provided more insight in camber morphing wings. Future research can use this work to develop the VCCW further and improve the simulation performance.

Appendix A. Roll Control Law

$$\begin{aligned}
\delta_{si-roll} = & ((1.64051^1 C_L - 4.93528^1 C_L^3 + 1.00612^2 C_L^5 - 8.33207^1 C_L^7 + 2.49045^1 C_L^9) \\
& + \bar{p}^2 (5.29980^1 C_L - 1.34964^3 C_L^3 + 4.31988^3 C_L^5 - 4.59661^3 C_L^7 + 1.56246^3 C_L^9) \\
& + \bar{p}^4 (-4.31142^1 C_L + 6.90137^4 C_L^3 - 2.20185^5 C_L^5 + 2.15008^5 C_L^7 - 5.92639^4 C_L^9) \\
& + \bar{p}^6 (-3.22745^4 C_L - 4.06622^5 C_L^3 + 7.16521^5 C_L^5 + 8.67792^5 C_L^7 - 1.33983^6 C_L^9))
\end{aligned} \tag{22}$$

$$\begin{aligned}
\delta_{sm-roll} = & ((3.73097^0 C_L - 1.87413^0 C_L^3 + 5.86335^0 C_L^5 - 1.95850^0 C_L^7) \\
& + \bar{p}^2 (-6.87701^1 C_L - 7.28837^1 C_L^3 + 2.10628^2 C_L^5 - 8.69048^1 C_L^7) \\
& + \bar{p}^4 (5.56926^3 C_L - 7.70709^3 C_L^3 + 1.17872^4 C_L^5 - 9.10452^3 C_L^7) \\
& + \bar{p}^6 (-7.20282^4 C_L + 1.82524^5 C_L^3 - 3.69341^5 C_L^5 + 2.45277^5 C_L^7))
\end{aligned} \tag{23}$$

$$\begin{aligned}
\delta_{so-roll} = & ((-3.39430^0 C_L - 6.47540^0 C_L^3 + 1.04183^1 C_L^5 - 3.97142^0 C_L^7) \\
& + \bar{p}^2 (3.36586^1 C_L - 1.84458^2 C_L^3 + 3.36282^2 C_L^5 - 1.18118^2 C_L^7) \\
& + \bar{p}^4 (4.74982^3 C_L - 5.72255^3 C_L^3 + 1.63670^4 C_L^5 - 1.59902^4 C_L^7) \\
& + \bar{p}^6 ((-8.14587^4 C_L + 1.76223^5 C_L^3 - 4.80796^5 C_L^5 + 3.73887^5 C_L^7))
\end{aligned} \tag{24}$$

Appendix B. Yaw Control Law

$$\begin{aligned}
\delta_{si-yaw} = & C_L((1.70865^1 + 9.69228^4 C_n^2 + -7.5908^9 C_n^4) + \bar{p}(-2.51603^3 C_n + -1.187028^9 C_n^3) + \bar{p}^2(1.48562^2 + -3.47766^8 C_n^2 + 1.25941^{13} C_n^4) \\
& + \bar{p}^3(-1.21139^7 C_n + 8.46599^{11} C_n^3) + \bar{p}^4(-4.46467^5 + 1.49338^{11} C_n^2 + -4.38075^{15} C_n^4) \\
& + C_L^3((-2.48885^1 + -9.44152^5 C_n^2 + 8.28197^{10} C_n^4) + \bar{p}(2.45271^5 C_n + 9.38941^9 C_n^3) + \bar{p}^2(4.81781^3 + 3.37789^9 C_n^2 + -1.34695^{14} C_n^4) \\
& + \bar{p}^3(8.46154^7 C_n + -8.15568^{12} C_n^3) + \bar{p}^4(4.61909^6 + -1.71144^{12} C_n^2 + 5.25847^{16} C_n^4) \\
& + C_L^5((-2.53978^1 + 6.26998^6 C_n^2 + -3.78185^{11} C_n^4) + \bar{p}(-9.78579^5 C_n + -3.98435^{10} C_n^3) + \bar{p}^2(-8.59350^3 + -1.73146^{10} C_n^2 + 6.78079^{14} C_n^4) \\
& + \bar{p}^3(-2.88831^8 C_n + 3.39093^{13} C_n^3) + \bar{p}^4(-2.02873^7 + 8.32103^{12} C_n^2 + -2.66169^{17} C_n^4) \\
& + C_L^7((1.18946^2 + -1.26318^7 C_n^2 + 6.56141^{11} C_n^4) + \bar{p}(1.45716^6 C_n + 6.93017^{10} C_n^3) + \bar{p}^2(2.35380^3 + 3.26043^{10} C_n^2 + -1.25906^{15} C_n^4) \\
& + \bar{p}^3(4.32023^8 C_n + -5.72841^{13} C_n^3) + \bar{p}^4(3.40589^7 + -1.50512^{13} C_n^2 + 4.89077^{17} C_n^4) \\
& + C_L^9((-8.12512^1 + 7.70792^6 C_n^2 + -3.73924^{11} C_n^4) + \bar{p}(-7.37298^5 C_n + -4.04955^{10} C_n^3) + \bar{p}^2(2.75479^3 + -1.95832^{10} C_n^2 + 7.47484^{14} C_n^4) \\
& + \bar{p}^3(-2.33398^8 C_n + -3.26071^{13} C_n^3) + \bar{p}^4(-1.90606^7 + 8.79879^{12} C_n^2 + -2.87363^{17} C_n^4))
\end{aligned} \tag{25}$$

$$\begin{aligned}
\delta_{sm-yaw} = & C_L((6.13642^0 + -9.12170^4 C_n^2 + 1.58958^{10} C_n^4) + \bar{p}(2.89186^4 C_n + 1.70122^9 C_n^3) + \bar{p}^2(5.36334^2 + 2.16058^8 C_n^2 + -1.33713^{13} C_n^4) \\
& + \bar{p}^3(4.16349^5 C_n + -5.60674^{11} C_n^3) + \bar{p}^4(3.77238^4 + -1.33679^{10} C_n^2 + 2.21141^{15} C_n^4) \\
& + C_L^3((-8.35018^0 + 9.89728^5 C_n^2 + -1.59648^{11} C_n^4) + \bar{p}(-2.57115^5 C_n + -1.32071^{10} C_n^3) + \bar{p}^2(-6.67989^3 + -1.42462^9 C_n^2 + 1.17578^{14} C_n^4) \\
& + \bar{p}^3(1.90131^7 C_n + 3.81404^{12} C_n^3) + \bar{p}^4(2.72784^6 + -4.39288^{11} C_n^2 + -4.00261^{15} C_n^4) \\
& + C_L^5((5.33261^0 + -1.64120^6 C_n^2 + 5.05571^{11} C_n^4) + \bar{p}(9.41845^5 C_n + 3.17590^{10} C_n^3) + \bar{p}^2(3.59257^4 + -5.41239^8 C_n^2 + -2.30960^{14} C_n^4) \\
& + \bar{p}^3(-1.34689^8 C_n + -4.61538^{12} C_n^3) + \bar{p}^4(-1.94260^7 + 4.41947^{12} C_n^2 + -8.01470^{16} C_n^4) \\
& + C_L^7((9.96452^0 + 3.70000^5 C_n^2 + -6.55388^{11} C_n^4) + \bar{p}(-1.29754^6 C_n + -3.20693^{10} C_n^3) + \bar{p}^2(-6.20669^4 + 8.03399^9 C_n^2 + 6.60876^{13} C_n^4) \\
& + \bar{p}^3(2.29318^8 C_n + -4.08356^{12} C_n^3) + \bar{p}^4(3.89566^7 + -1.02935^{13} C_n^2 + 2.47355^{17} C_n^4) \\
& + C_L^9((-7.47992^0 + 5.83174^5 C_n^2 + 2.99759^{11} C_n^4) + \bar{p}(6.15337^5 C_n + 1.15264^{10} C_n^3) + \bar{p}^2(3.59158^4 + -7.28570^9 C_n^2 + 9.28253^{13} C_n^4) \\
& + \bar{p}^3(-1.19694^8 C_n + 6.85814^{12} C_n^3) + \bar{p}^4(-2.42868^7 + 7.01384^{12} C_n^2 + -1.86098^{17} C_n^4))
\end{aligned}
\tag{26}$$

$$\begin{aligned}
\delta_{so-yaw} = & C_L((1.46900^{-1} + -2.18055^5 C_n^2 + -1.80409^{10} C_n^4) + \bar{p}(-1.42996^3 C_n + -4.73865^9 C_n^3) \\
& + \bar{p}^2(-6.33501^2 + 9.33952^6 C_n^2 + -1.75070^{12} C_n^4) + \bar{p}^3(-2.29563^7 C_n + 1.40551^{12} C_n^3) + \bar{p}^4(-8.65025^4 + -6.13896^{10} C_n^2 + 2.36505^{15} C_n^4) \\
& + C_L^3((-1.59180^1 + 9.54656^5 C_n^2 + 1.85100^{11} C_n^4) + \bar{p}(-9.60569^4 C_n + 4.47779^{10} C_n^3) \\
& + \bar{p}^2(-2.29255^3 + 2.05018^8 C_n^2 + 1.59350^{12} C_n^4) + \bar{p}^3(2.21239^8 C_n + -1.44641^{13} C_n^3) + \bar{p}^4(2.79156^6 + 3.27549^{11} C_n^2 + -1.62603^{16} C_n^4) \\
& + C_L^5((1.46884^1 + 5.07624^5 C_n^2 + -7.07257^{11} C_n^4) + \bar{p}(4.42391^5 C_n + -1.56377^{11} C_n^3) \\
& + \bar{p}^2(2.45539^4 + -5.83236^9 C_n^2 + 1.63018^{14} C_n^4) + \bar{p}^3(-8.08105^8 C_n + 5.41729^{13} C_n^3) + \bar{p}^4(-1.69306^7 + 7.25160^{11} C_n^2 + -8.63529^{14} C_n^4) \\
& + C_L^7((9.12996^0 + -4.61203^6 C_n^2 + 1.09526^{12} C_n^4) + \bar{p}(-6.22479^5 C_n + 2.27058^{11} C_n^3) \\
& + \bar{p}^2(-4.92575^4 + 1.55504^{10} C_n^2 + -4.60919^{14} C_n^4) + \bar{p}^3(1.2135^9 C_n + -8.36926^{13} C_n^3) + \bar{p}^4(3.23882^7 + -3.52713^{12} C_n^2 + 7.46294^{16} C_n^4) \\
& + C_L^9((-1.18559^1 + 3.66892^6 C_n^2 + -5.84549^{11} C_n^4) + \bar{p}(2.65838^5 C_n + -1.16304^{11} C_n^3) \\
& + \bar{p}^2(2.80631^4 + -1.09541^{10} C_n^2 + 3.24987^{14} C_n^4) + \bar{p}^3(-6.40641^8 C_n + 4.50987^{13} C_n^3) + \bar{p}^4(-1.96449^7 + 2.83475^{12} C_n^2 + -6.67346^{16} C_n^4))
\end{aligned}
\tag{27}$$

$$\begin{aligned}
\delta_{ai} = & ((-3.36061^3 C_n^1 + 2.20900^7 C_n^3 + \bar{p}(-5.27670^1 + 3.46539^6 C_n^2) + \bar{p}^2(9.08464^4 C_n^1 + 8.09983^9 C_n^3 + \bar{p}^3(-4.38828^3 + -2.77171^8 C_n^2) \\
& + C_L^2((2.10560^4 C_n^1 + -4.12837^8 C_n^3 + \bar{p}(-2.71589^2 + -4.14402^7 C_n^2) + \bar{p}^2(-1.72430^6 C_n^1 + -1.63126^{10} C_n^3 + \bar{p}^3(9.02694^4 + 6.68667^9 C_n^2) \\
& + C_L^4((-7.63649^4 C_n^1 + 1.71782^9 C_n^3 + \bar{p}(6.21203^2 + 1.17634^8 C_n^2) + \bar{p}^2(3.39923^6 C_n^1 + 1.21924^{11} C_n^3 + \bar{p}^3(-5.04764^5 + -2.04750^{10} C_n^2) \\
& + C_L^6((1.12453^5 C_n^1 + -2.47512^9 C_n^3 + \bar{p}(-1.07662^3 + -7.11858^7 C_n^2) + \bar{p}^2(4.76624^6 C_n^1 + -5.32951^{11} C_n^3 + \bar{p}^3(1.11786^6 + 1.95445^9 C_n^2) \\
& + C_L^8((-5.79657^4 C_n^1 + 1.16354^9 C_n^3 + \bar{p}(6.00295^2 + -2.17730^7 C_n^2) + \bar{p}^2(-7.99752^6 C_n^1 + 4.97879^{11} C_n^3 + \bar{p}^3(-7.66977^5 + 1.77036^{10} C_n^2)
\end{aligned}
\tag{28}$$

120

$$\begin{aligned}
\delta_{am} = & ((7.26447^2 C_n^1 + -2.20840^7 C_n^3 + \bar{p}(5.1883^1 + -3.28040^6 C_n^2) + \bar{p}^2(-9.00917^4 C_n^1 + 2.19924^8 C_n^3 + \bar{p}^3(-1.52822^3 + 4.06123^8 C_n^2) \\
& + C_L^2((-5.42031^3 C_n^1 + 2.31708^8 C_n^3 + \bar{p}(-2.34106^1 + 2.94233^7 C_n^2) + \bar{p}^2(8.62804^5 C_n^1 + -1.24263^{10} C_n^3 + \bar{p}^3(8.03026^2 + -4.02522^9 C_n^2) \\
& + C_L^4((1.94253^4 C_n^1 + -8.54412^8 C_n^3 + \bar{p}(9.83085^1 + -1.01121^8 C_n^2) + \bar{p}^2(-3.51849^6 C_n^1 + 3.29313^{10} C_n^3 + \bar{p}^3(1.35384^4 + 1.11893^{10} C_n^2) \\
& + C_L^6((-2.88489^4 C_n^1 + 1.25931^9 C_n^3 + \bar{p}(-1.21576^2 + 1.40890^8 C_n^2) + \bar{p}^2(5.33231^6 C_n^1 + 3.04826^9 C_n^3 + \bar{p}^3(-4.20052^4 + -9.50602^9 C_n^2) \\
& + C_L^8((1.48122^4 C_n^1 + -6.43755^8 C_n^3 + \bar{p}(3.50549^1 + -7.00531^7 C_n^2) + \bar{p}^2(-2.91939^6 C_n^1 + -3.55626^{10} C_n^3 + \bar{p}^3(2.20100^4 + 1.05180^9 C_n^2)
\end{aligned}
\tag{29}$$

$$\begin{aligned}
\delta_{ao} = & ((-1.18879^2 C_n^1 + 2.98344^7 C_n^3 + \bar{p}(5.30888^1 + 4.73749^6 C_n^2) + \bar{p}^2(1.25774^4 C_n^1 + -1.92698^9 C_n^3 + \bar{p}^3(4.49047^3 + -6.03426^8 C_n^2) \\
& + C_L^2((2.19296^3 C_n^1 + -2.54577^8 C_n^3 + \bar{p}(1.52276^2 + -4.09369^7 C_n^2) + \bar{p}^2(-8.91898^5 C_n^1 + 1.65574^{10} C_n^3 + \bar{p}^3(-3.30023^4 + 5.30453^9 C_n^2) \\
& + C_L^4((-7.39010^3 C_n^1 + 8.67074^8 C_n^3 + \bar{p}(-4.42766^2 + 1.51480^8 C_n^2) + \bar{p}^2(4.73879^6 C_n^1 + -6.04450^{10} C_n^3 + \bar{p}^3(1.52340^5 + -1.60557^{10} C_n^2) \\
& + C_L^6((1.11439^4 C_n^1 + -1.28885^9 C_n^3 + \bar{p}(6.66100^2 + -2.44366^8 C_n^2) + \bar{p}^2(-1.03216^7 C_n^1 + 1.18609^{11} C_n^3 + \bar{p}^3(-3.08691^5 + 2.24775^{10} C_n^2) \\
& + C_L^8((-5.7056^3 C_n^1 + 6.88366^8 C_n^3 + \bar{p}(-3.21344^2 + 1.40762^8 C_n^2) + \bar{p}^2(7.36354^6 C_n^1 + -7.67605^{10} C_n^3 + \bar{p}^3(2.20067^5 + -1.15720^{10} C_n^2)
\end{aligned}
\tag{30}$$

Appendix C. Flight Simulation Plots

There are five iterations of the simulation:

1. Results from raw control input data
2. Results without bias in control input data
3. Results with Least Squares Approach Design I: Segment C thrust model
4. Results with the Static Approach: MotorCalc thrust model
5. Results with the Static Approach: VCCW thrust model

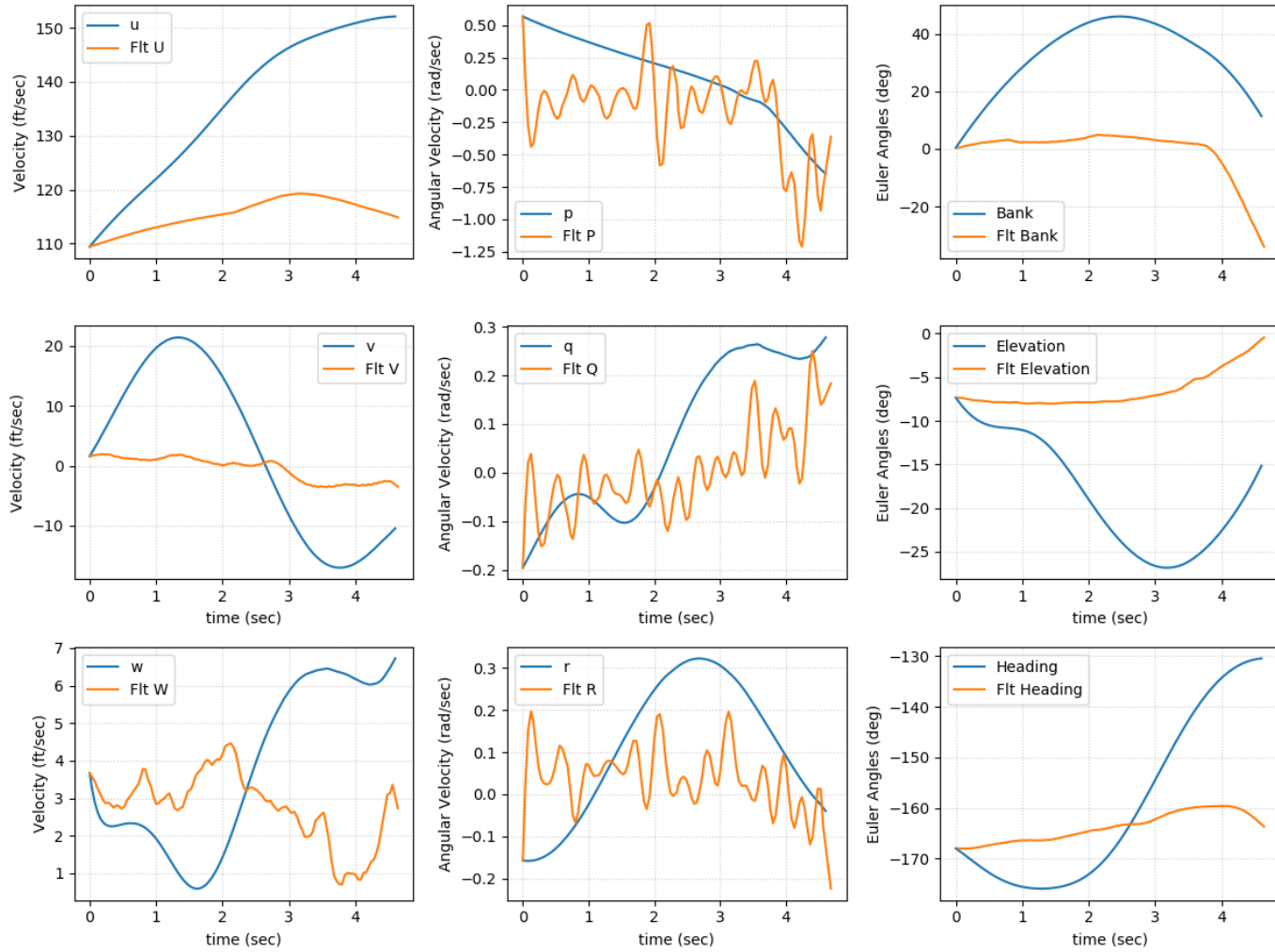


Figure 50: This is the first iteration of the simulation for Segment A. The blue shows the simulation data and the orange shows the actual flight data. The results use the raw control input data. There are all the flight characteristics: $u, v, w, p, q, r, \phi, \theta$, and ψ .

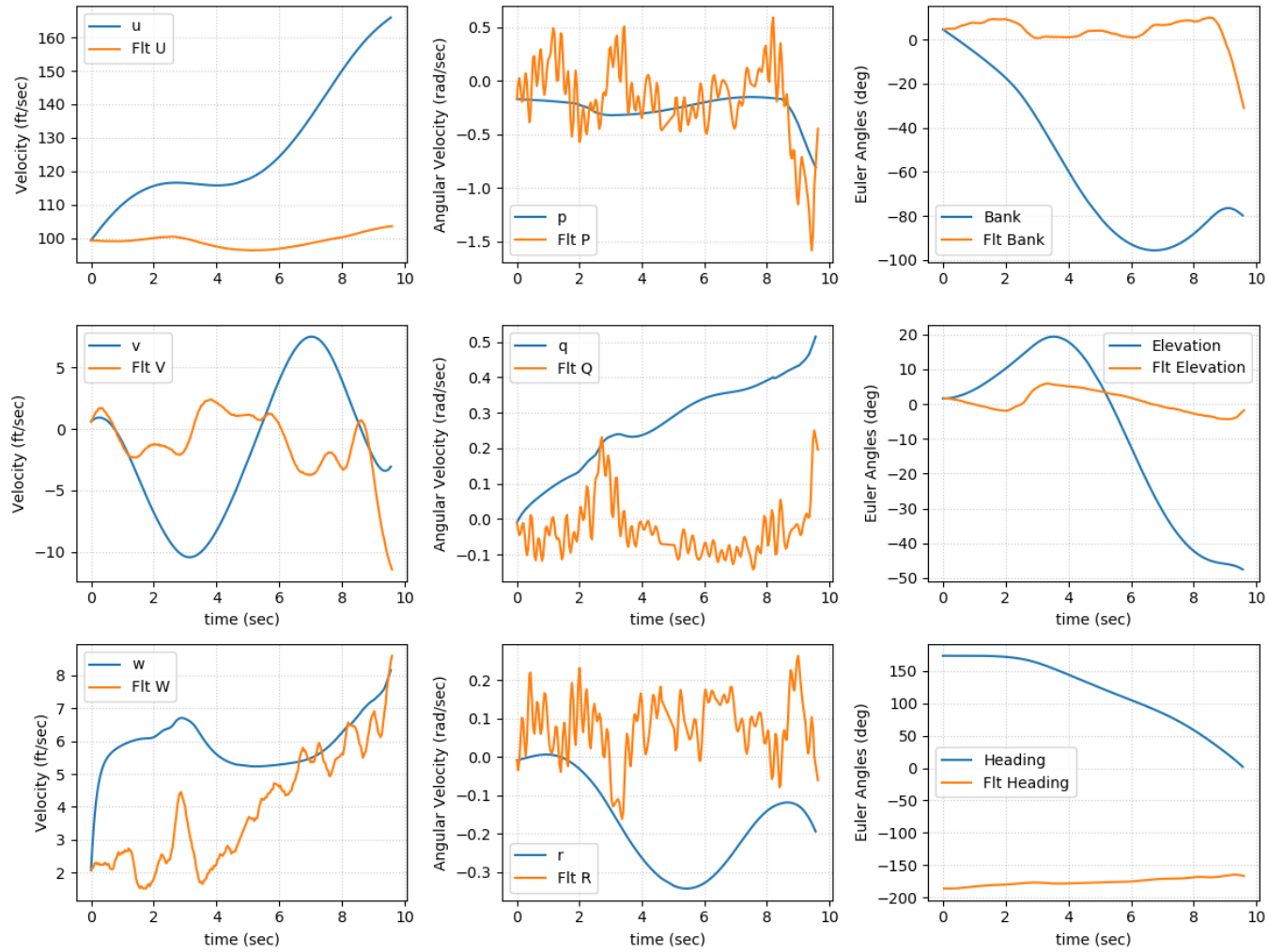


Figure 51: This is the first iteration of the simulation for Segment B. The blue shows the simulation data and the orange shows the actual flight data. The results use the raw control input data. There are all the flight characteristics: $u, v, w, p, q, r, \phi, \theta$, and ψ .

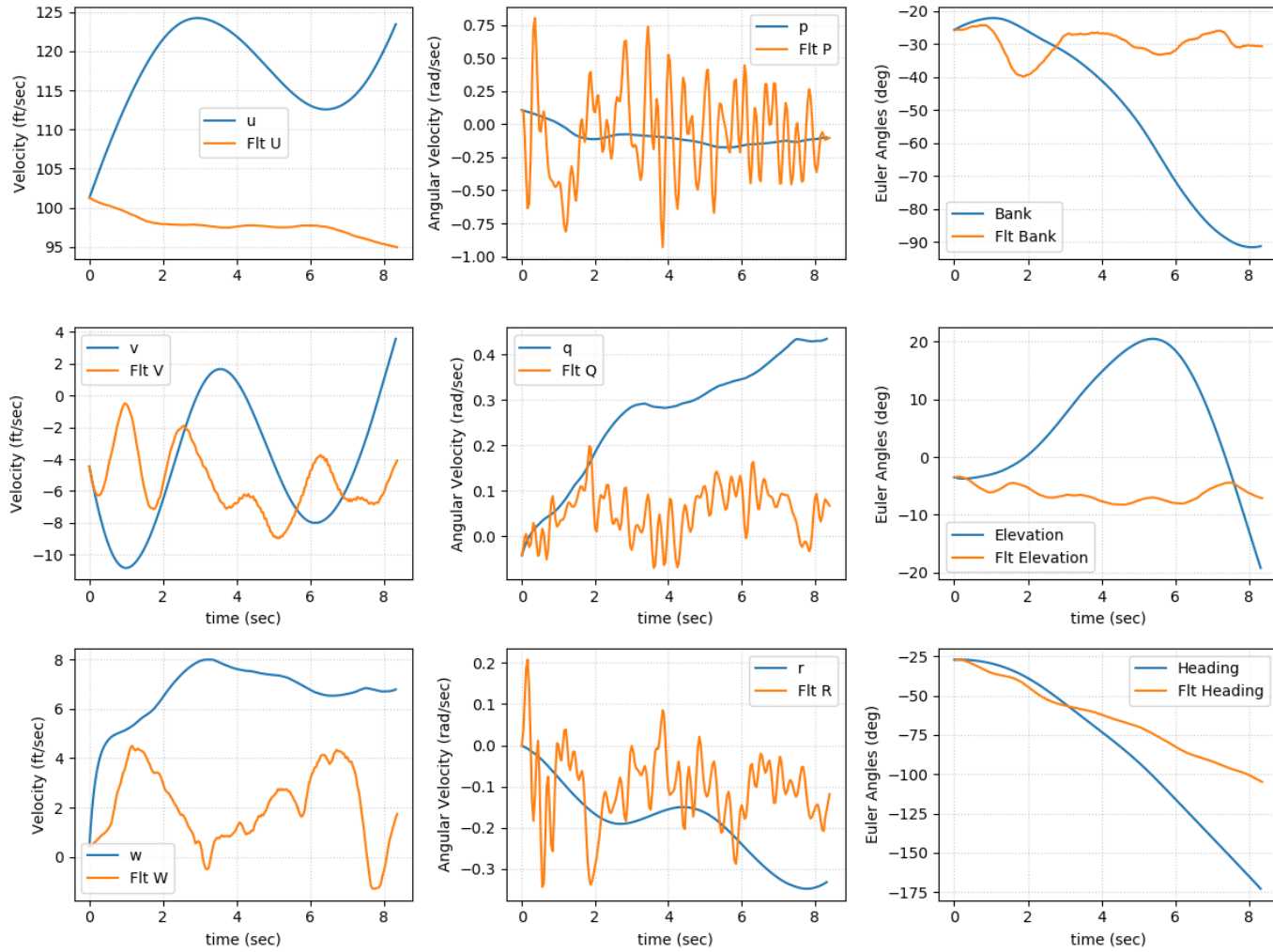


Figure 52: This is the first iteration of the simulation for the Segment C. The blue shows the simulation data and the orange shows the actual flight data. The results use the raw control input data. There are all the flight characteristics: $u, v, w, p, q, r, \phi, \theta$, and ψ .

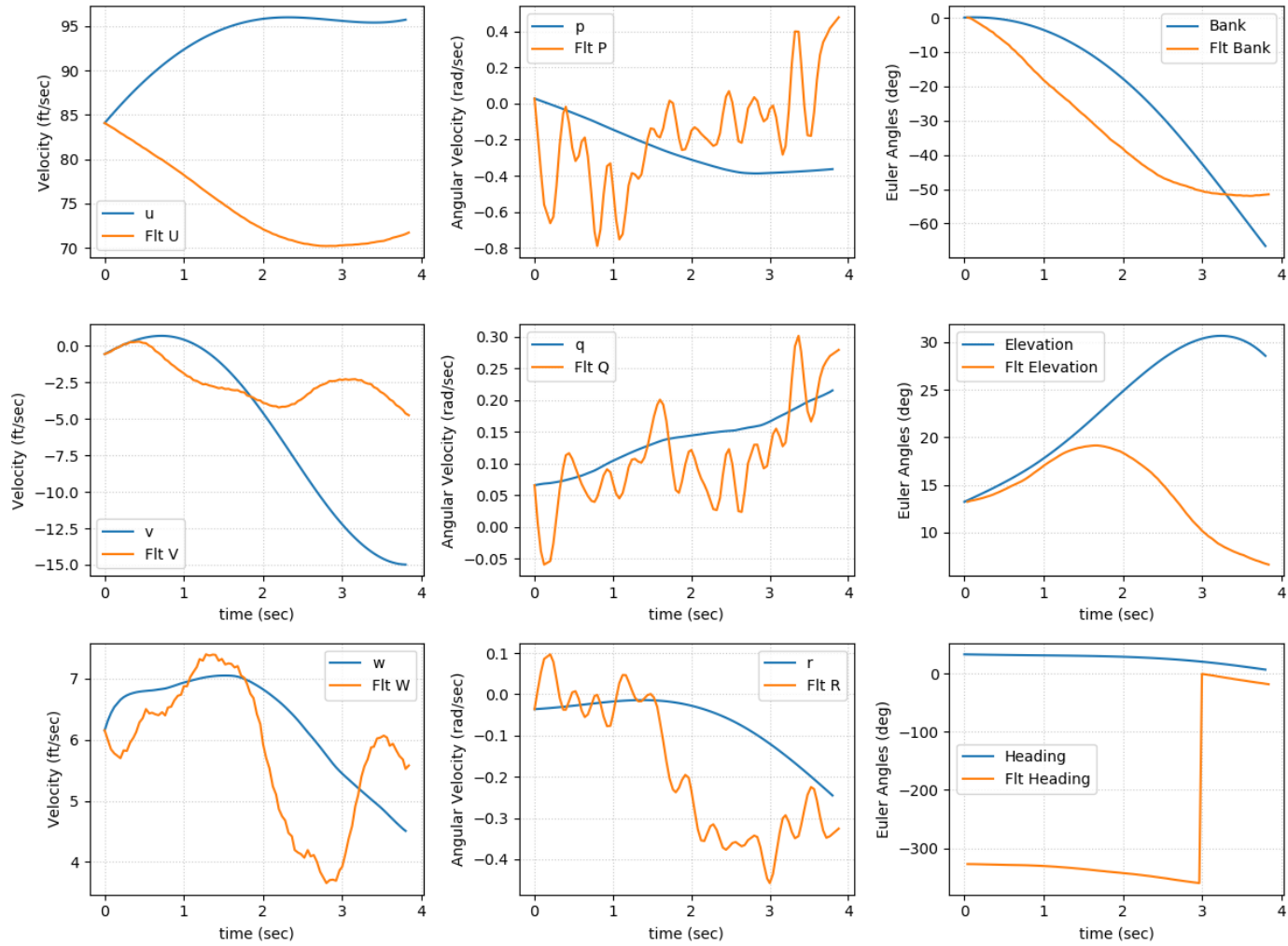


Figure 53: This is the first iteration of the simulation for Segment D. The blue shows the simulation data and the orange shows the actual flight data. The results use the raw control input data. There are all the flight characteristics: u , v , w , p , q , r , ϕ , θ , and ψ .

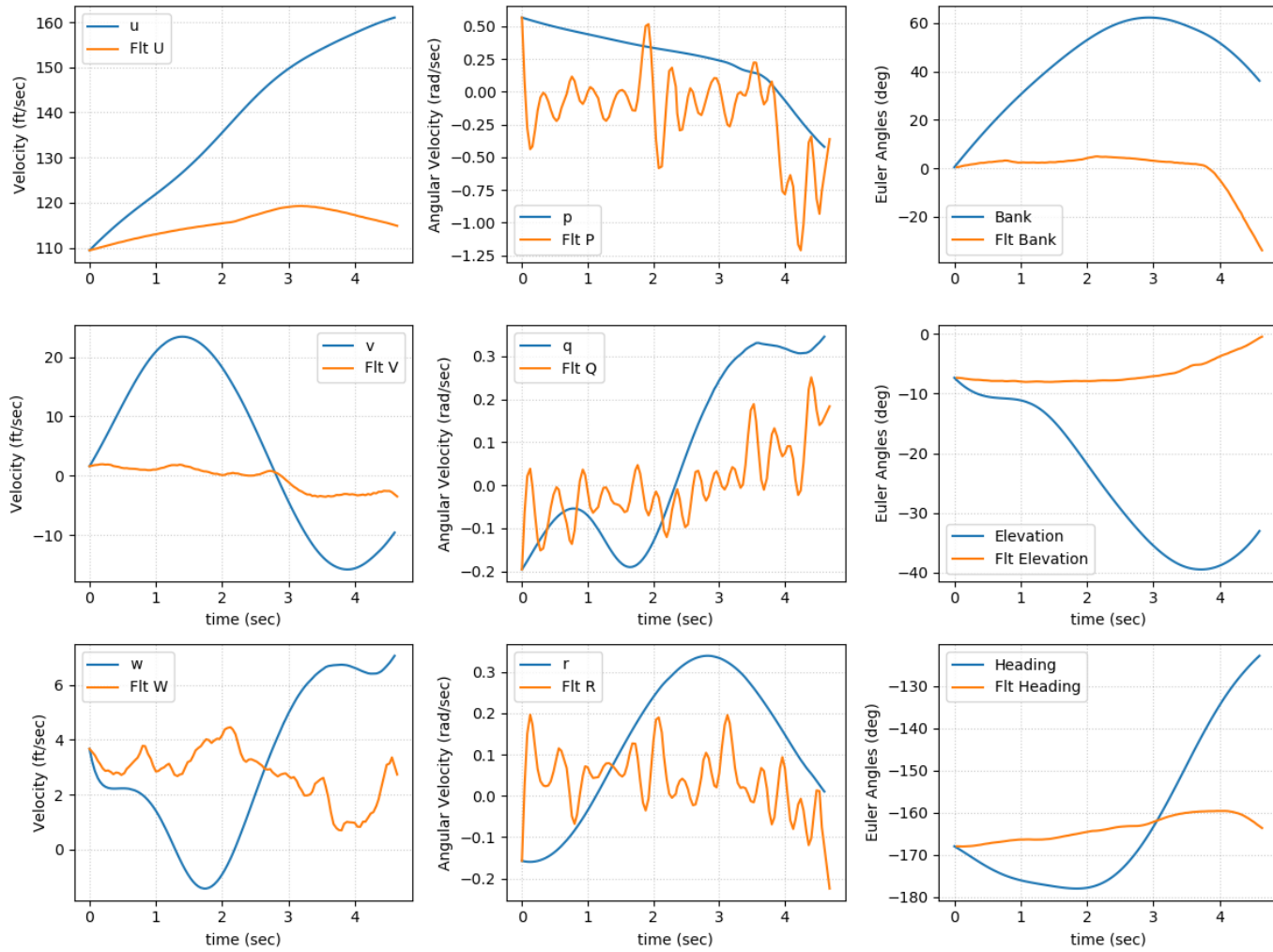


Figure 54: This is the second iteration of the simulation for Segment A. The blue shows the simulation data and the orange shows the actual flight data. There was an input bias on the aileron, elevator and rudder. However, the elevator bias was too drastic. This iteration removes the bias for the aileron and rudder.

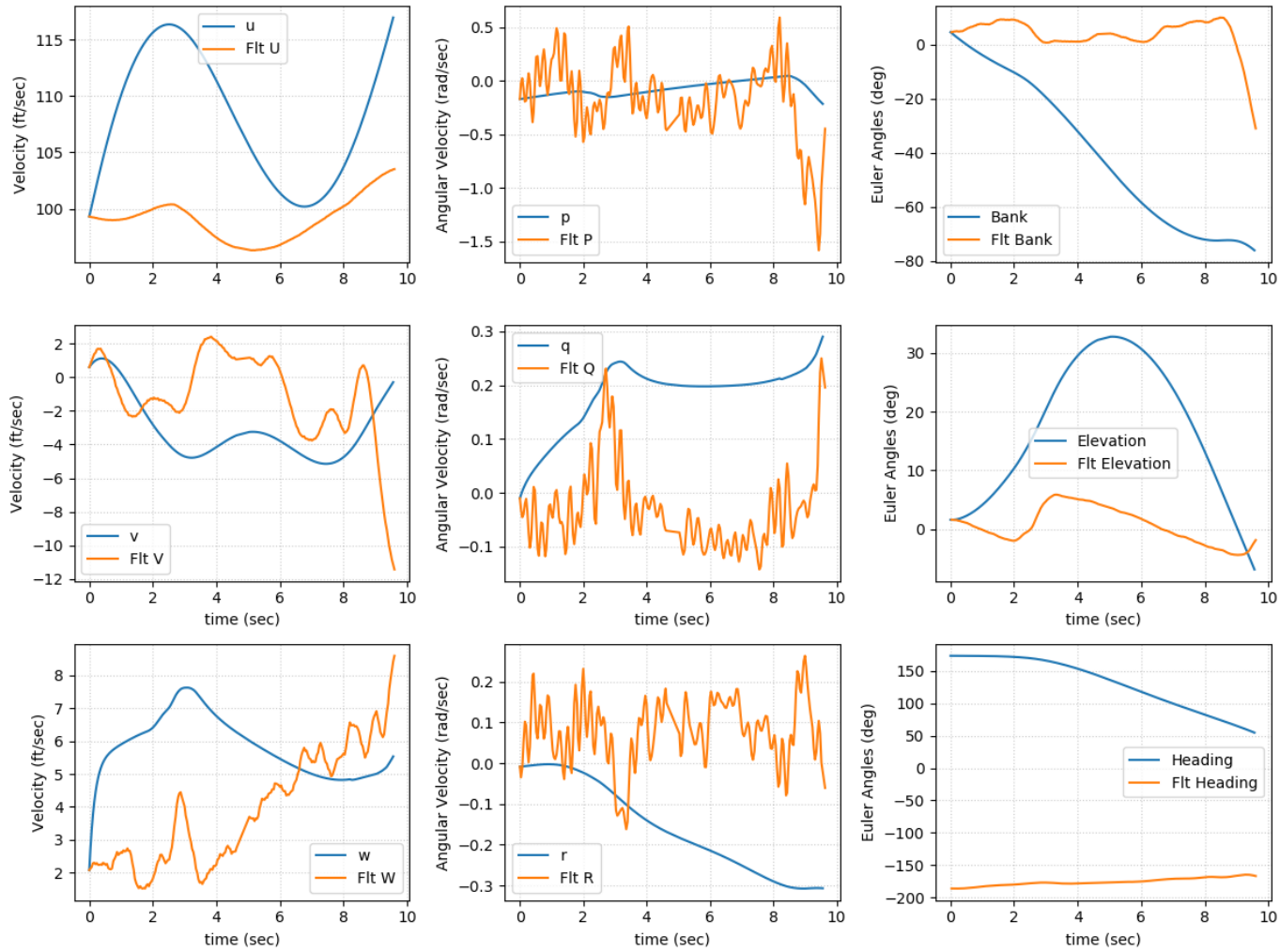


Figure 55: This is the second iteration of the simulation for Segment B. The blue shows the simulation data and the orange shows the actual flight data. There was an input bias on the aileron, elevator and rudder. However, the elevator bias was too drastic. This iteration removes the bias for the aileron and rudder.

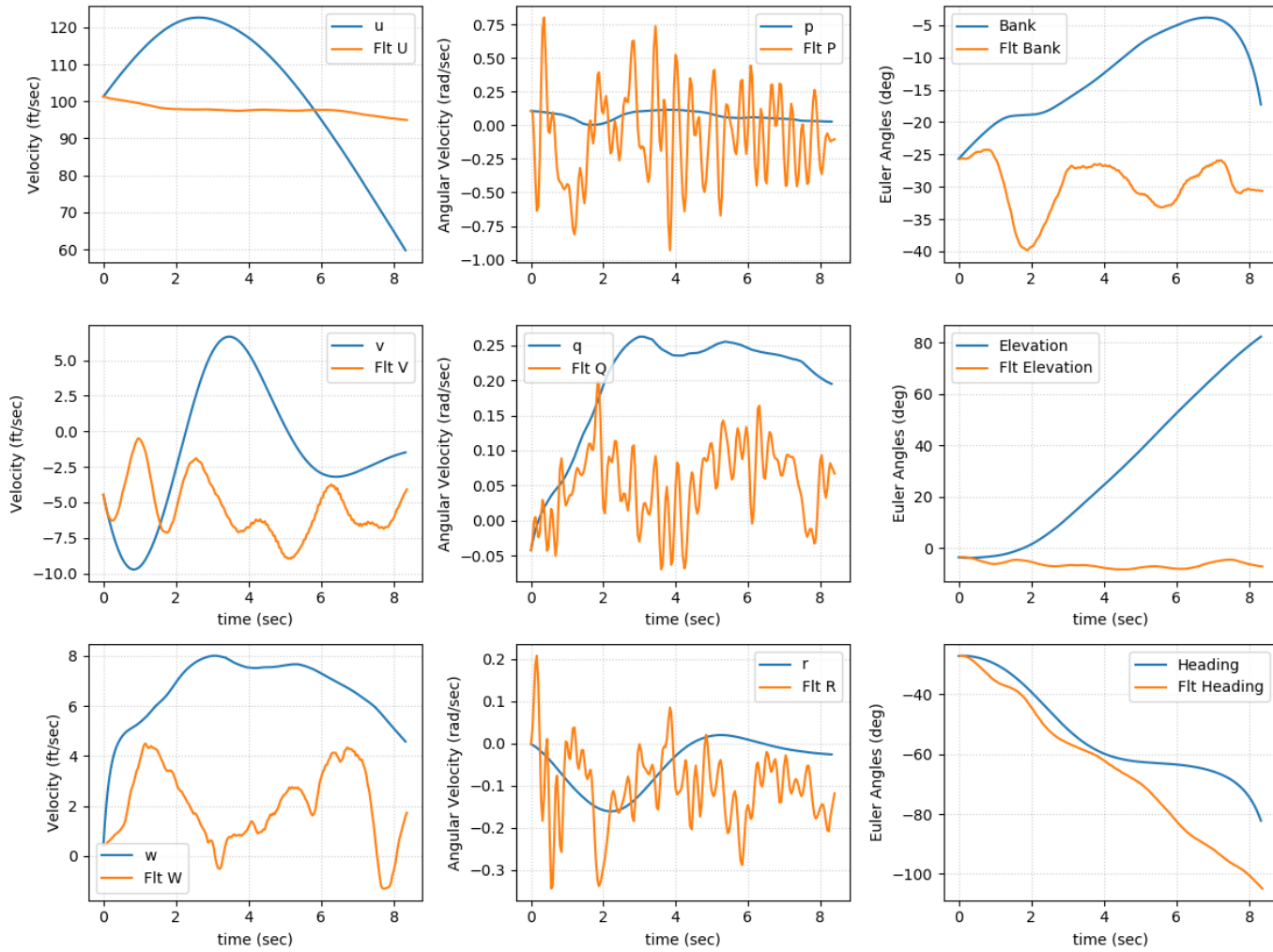


Figure 56: This is the second iteration of the simulation for Segment C. The blue shows the simulation data and the orange shows the actual flight data. There was an input bias on the aileron, elevator and rudder. However, the elevator bias was too drastic. This iteration removes the bias for the aileron and rudder.

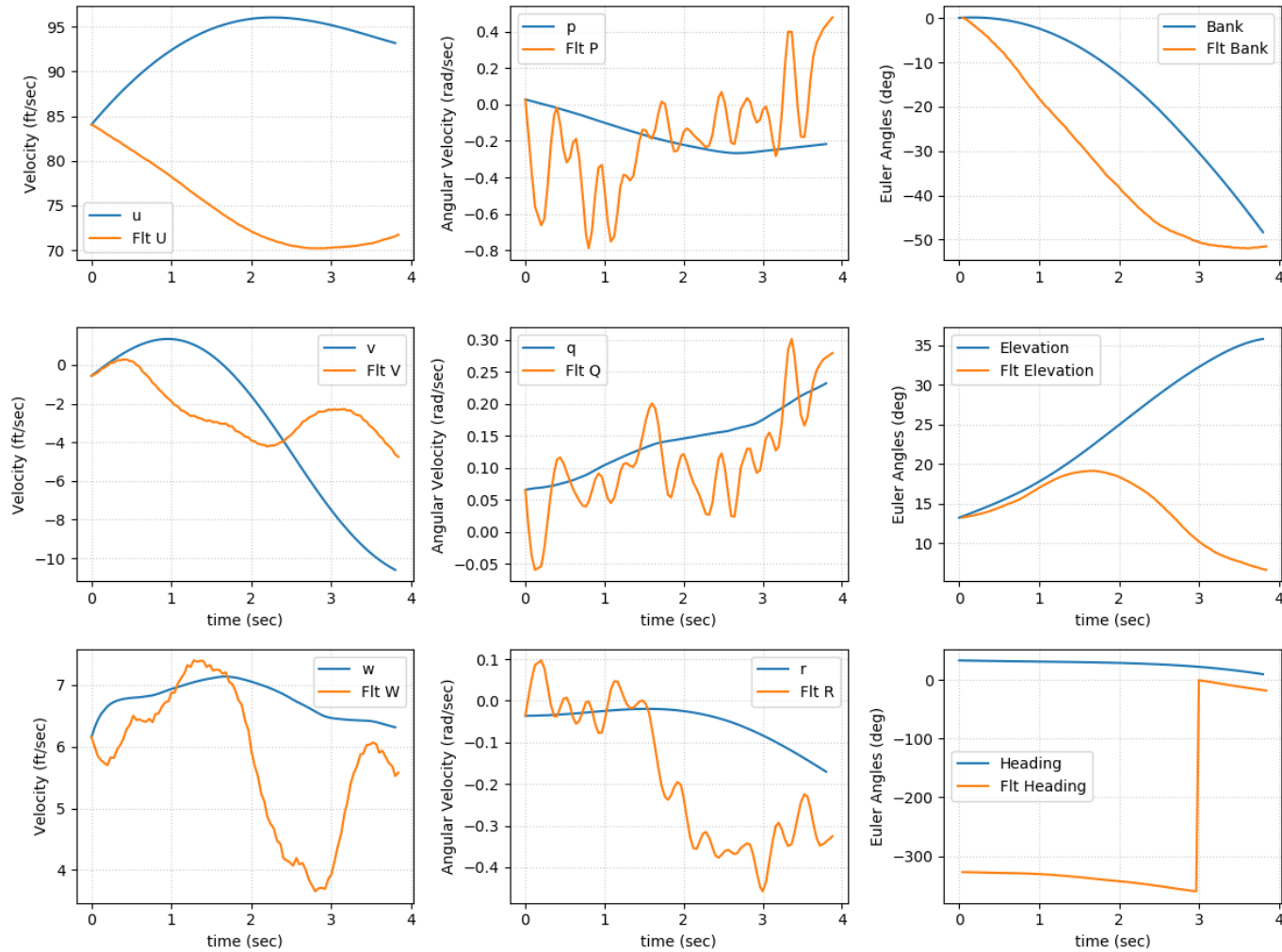


Figure 57: This is the second iteration of the simulation for the Segment D. The blue shows the simulation data and the orange shows the actual flight data. There was an input bias on the aileron, elevator and rudder. However, the elevator bias was too drastic. This iteration removes the bias for the aileron and rudder.

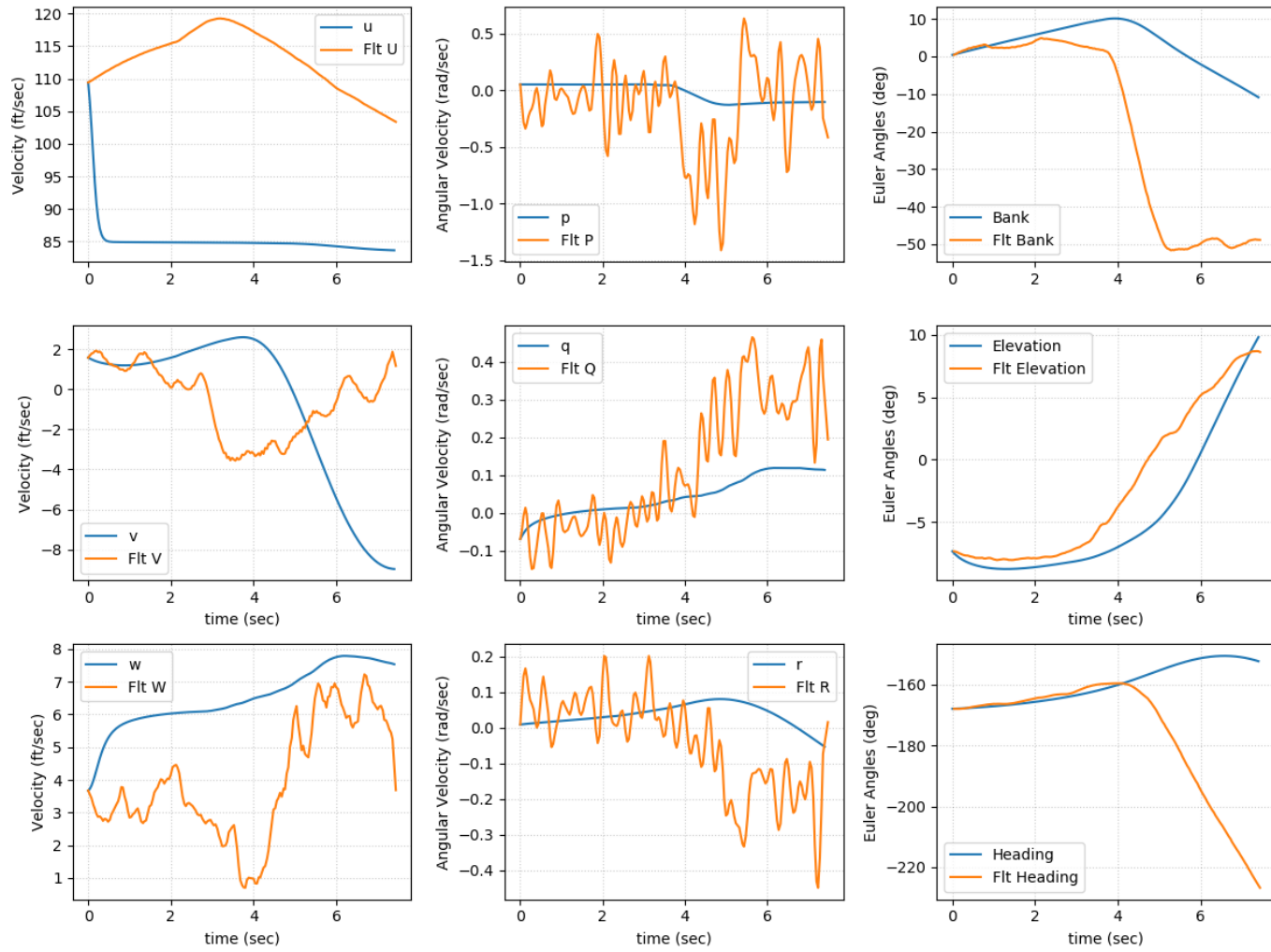


Figure 58: This is the third iteration of the simulation for Segment A. The blue shows the simulation data and the orange shows the actual flight data. This simulation uses the Least Squares Approach Design I: Segment C thrust model.

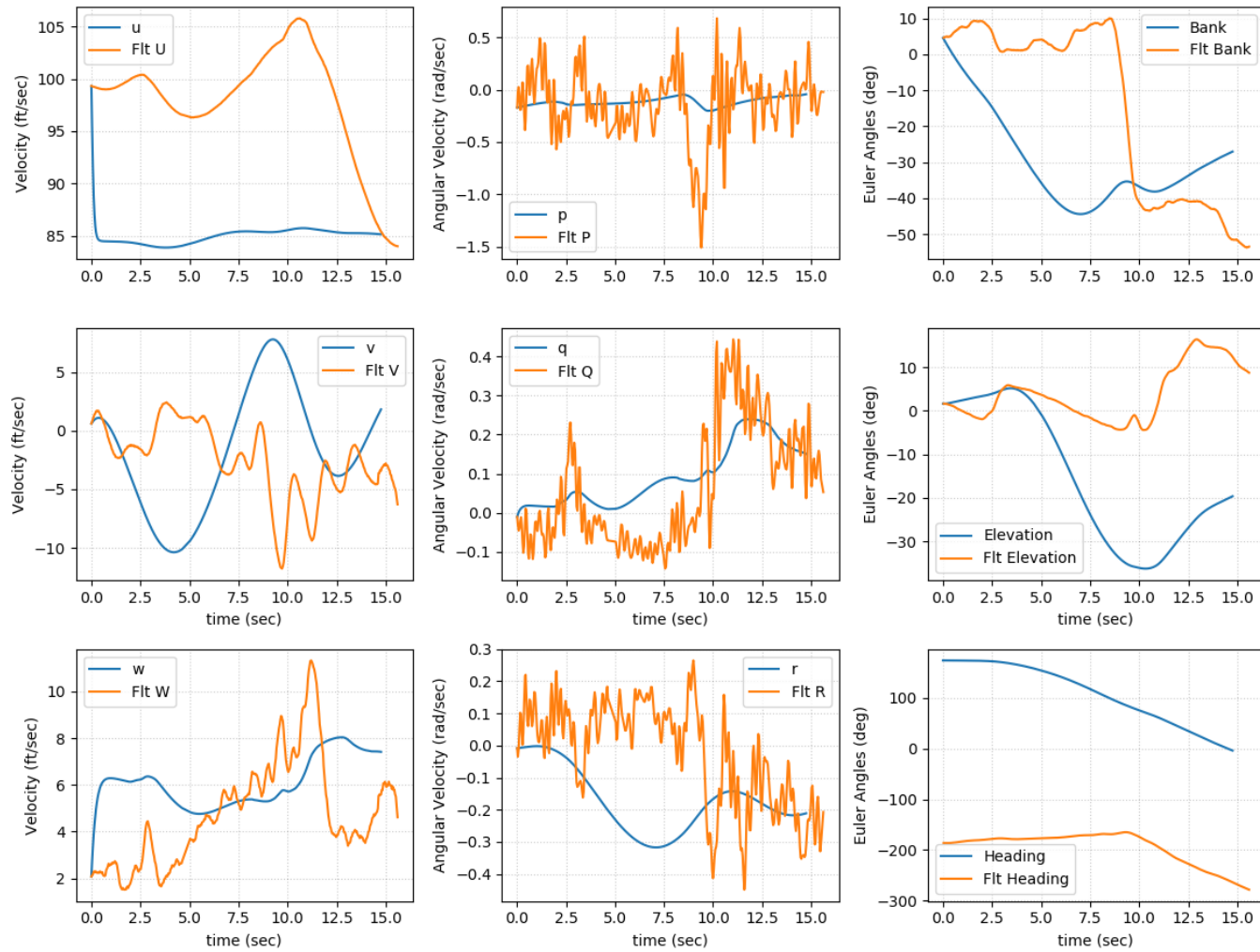


Figure 59: This is the third iteration of the simulation for Segment B. The blue shows the simulation data and the orange shows the actual flight data. This simulation uses the Least Squares Approach Design I: Segment C thrust model.

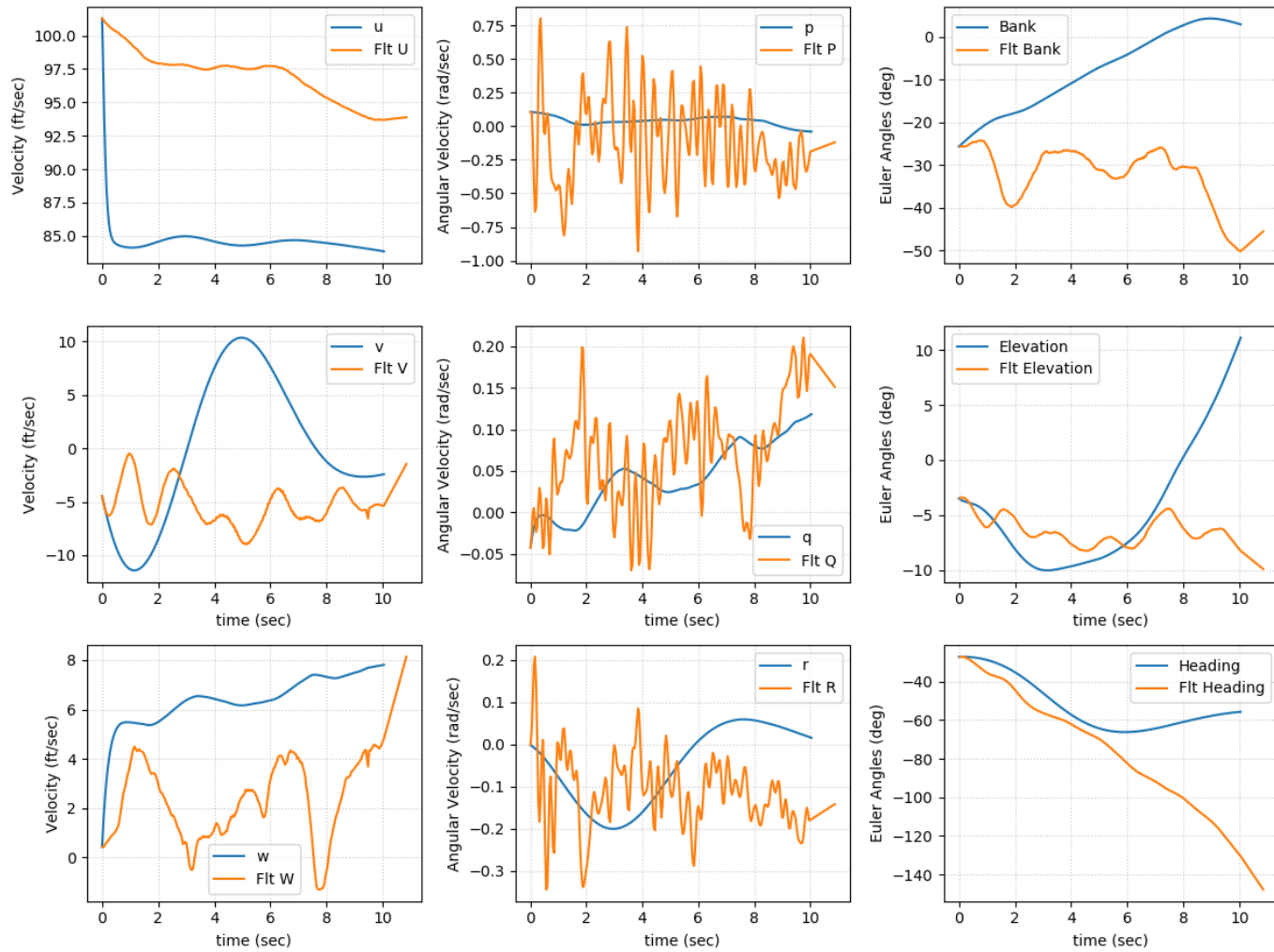


Figure 60: This is the third iteration of the simulation for Segment C. The blue shows the simulation data and the orange shows the actual flight data. This simulation uses the Least Squares Approach Design I: Segment C thrust model.

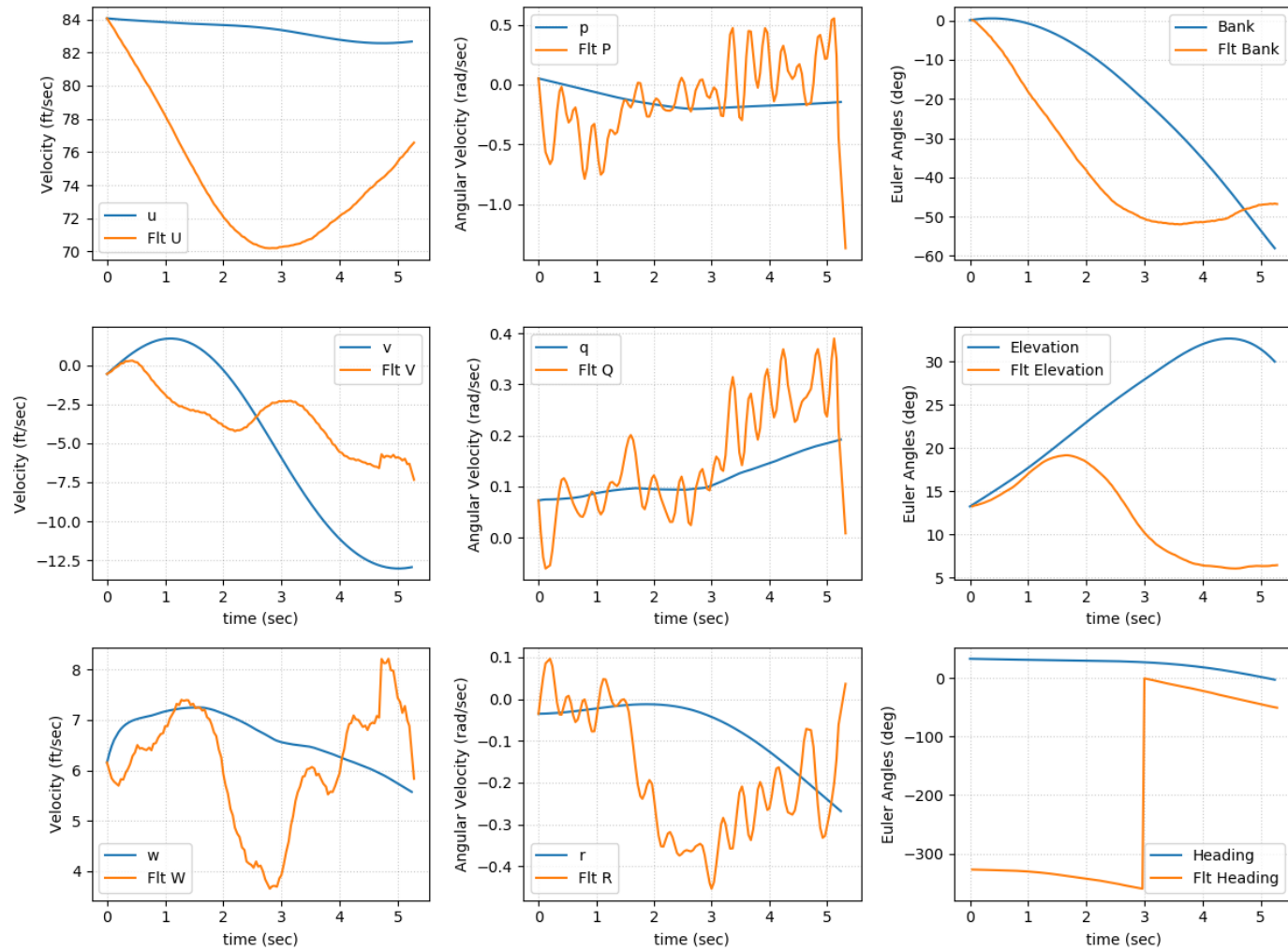


Figure 61: This is the third iteration of the simulation for the Segment D. The blue shows the simulation data and the orange shows the actual flight data. This simulation uses the Least Squares Approach Design I: Segment C thrust model.

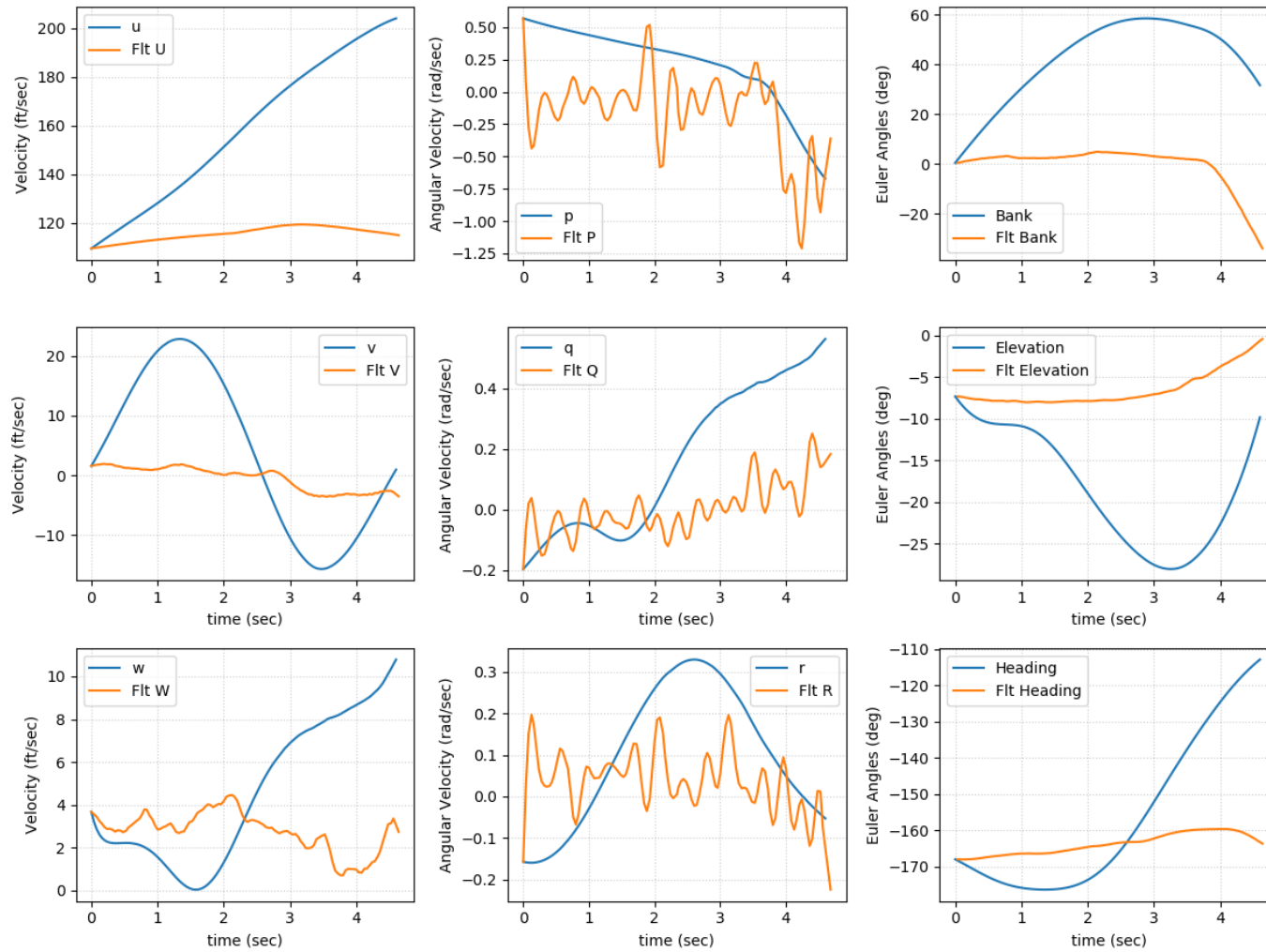


Figure 62: This is the fourth iteration of the simulation for Segment A. The blue shows the simulation data and the orange shows the actual flight data. This simulation uses the MotorCalc static thrust model.

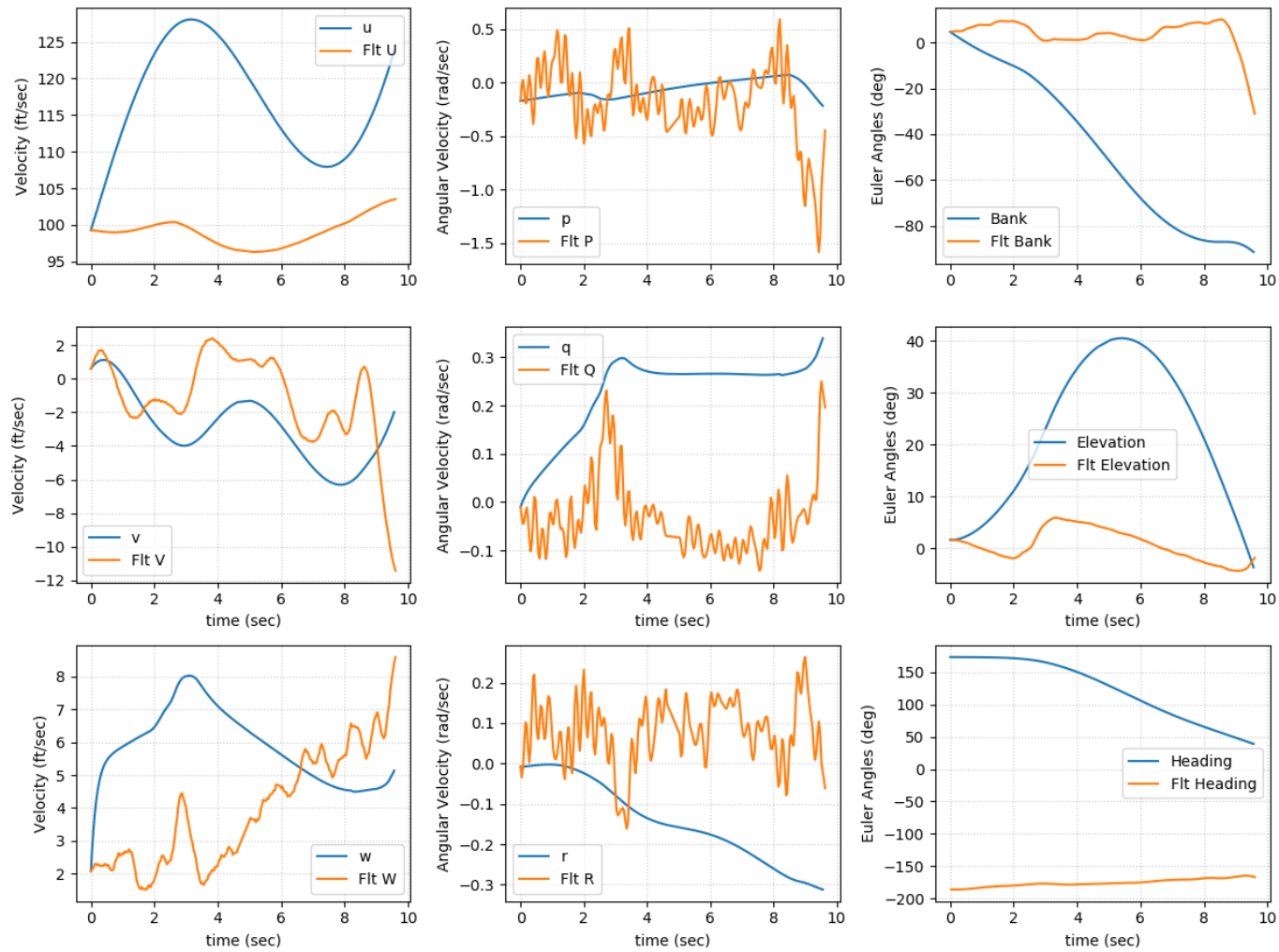


Figure 63: This is the fourth iteration of the simulation for Segment B. The blue shows the simulation data and the orange shows the actual flight data. This simulation uses the MotorCalc static thrust model.

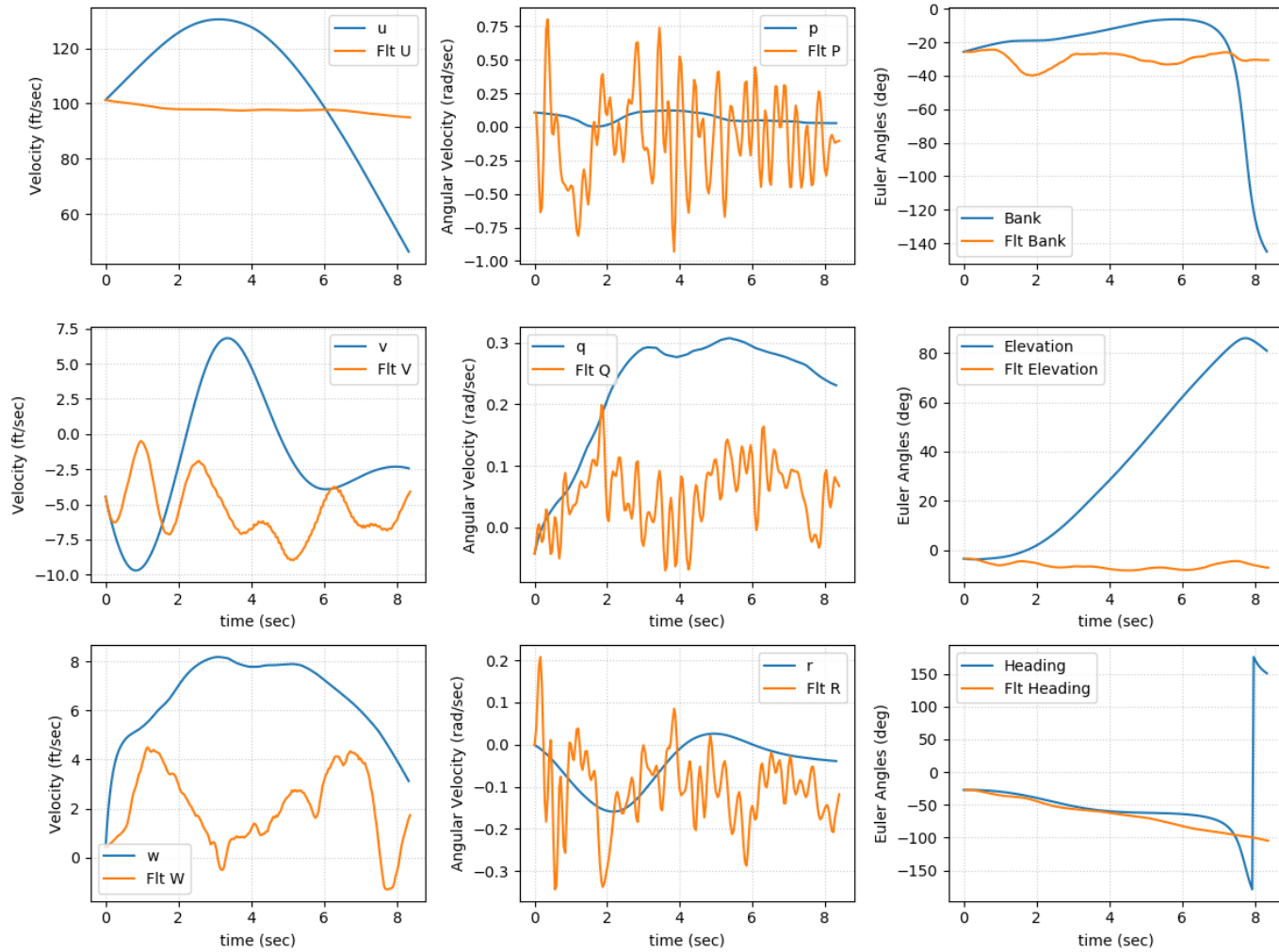


Figure 64: This is the fourth iteration of the simulation for Segment C. The blue shows the simulation data and the orange shows the actual flight data. This simulation uses the MotorCalc static thrust model.

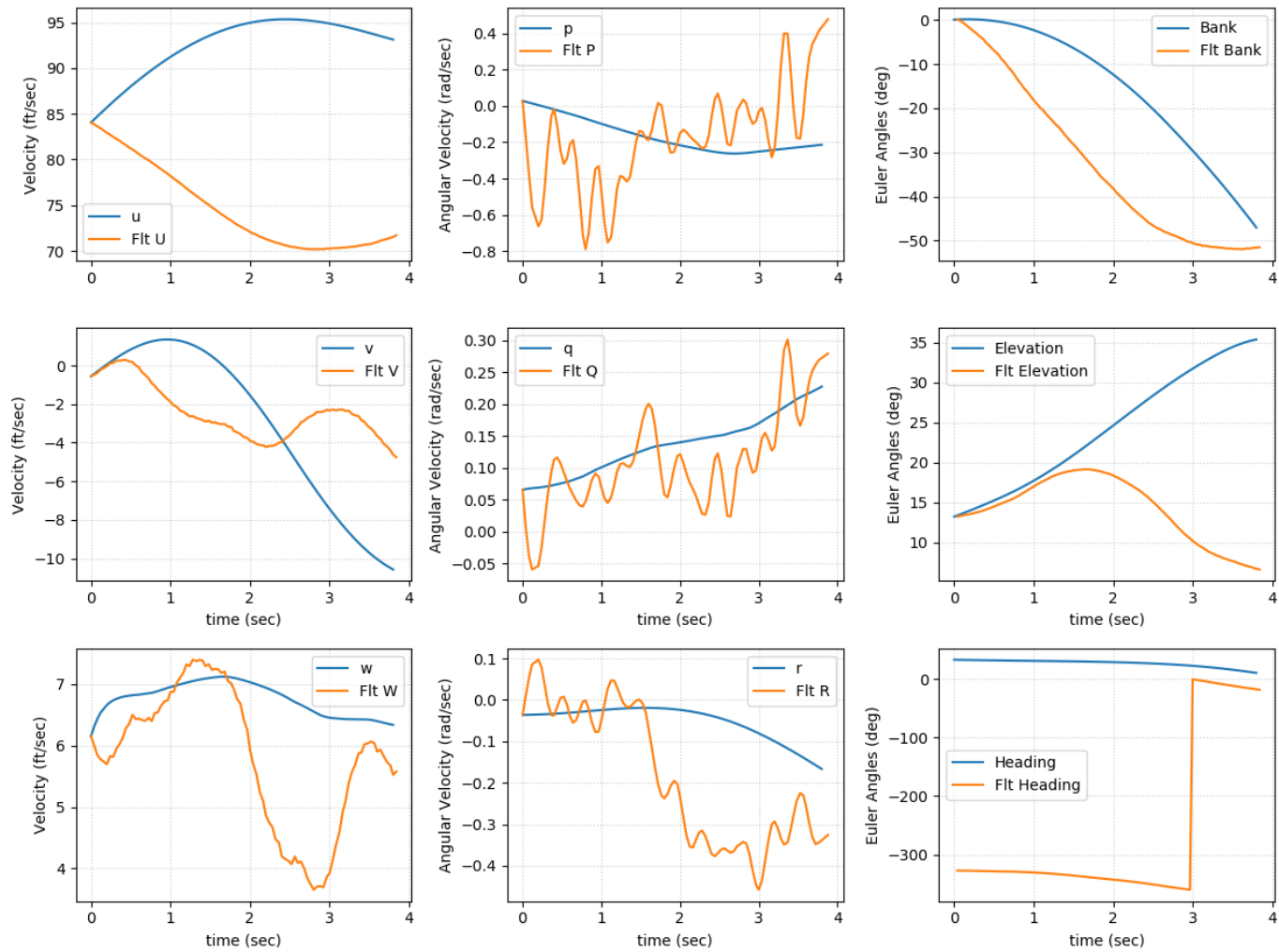


Figure 65: This is the fourth iteration of the simulation for the Segment D. The blue shows the simulation data and the orange shows the actual flight data. This simulation uses the MotorCalc static thrust model.

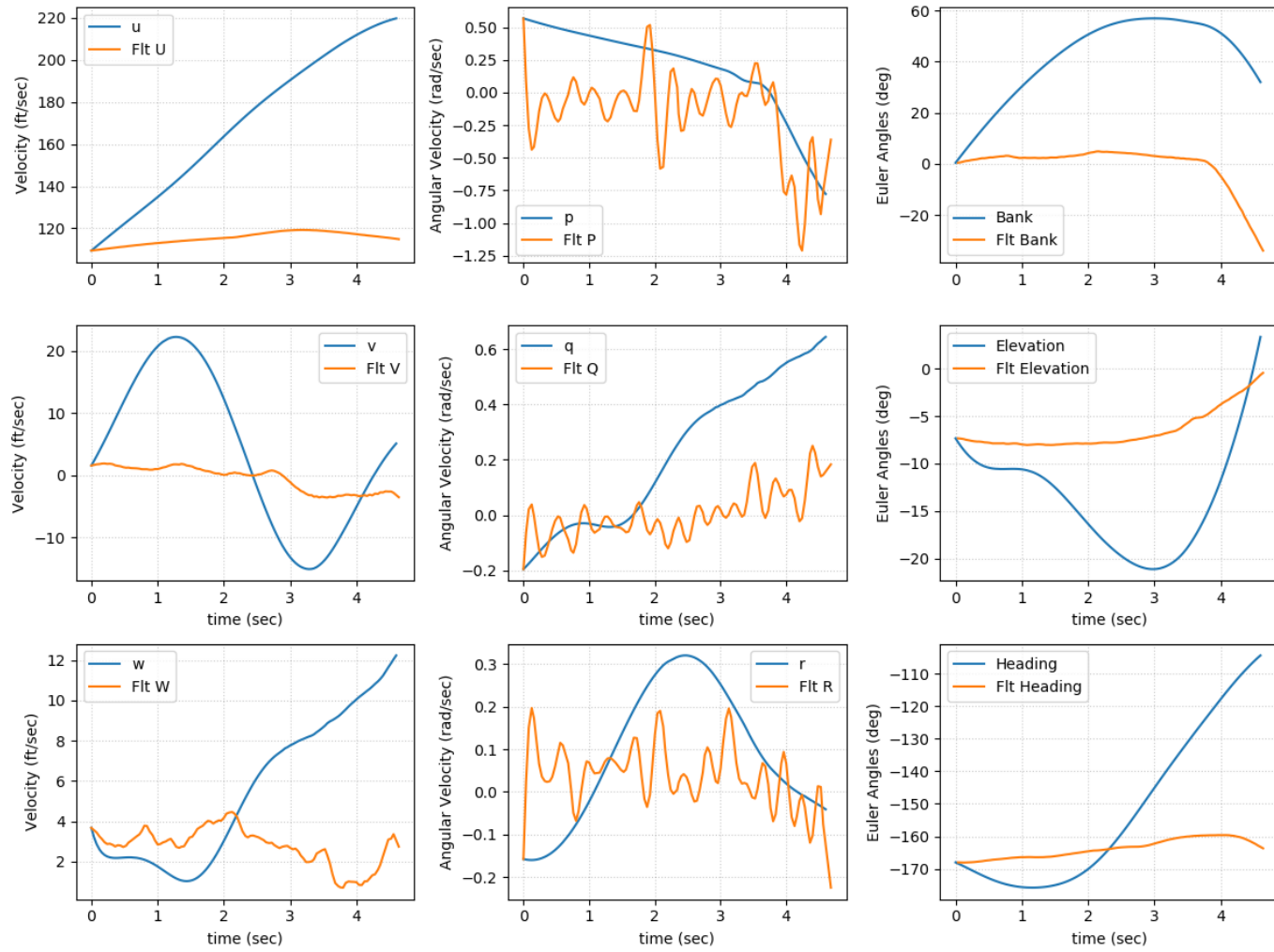


Figure 66: This is the fifth iteration of the simulation for Segment A. The blue shows the simulation data and the orange shows the actual flight data. This simulation uses the VCCW static thrust model.

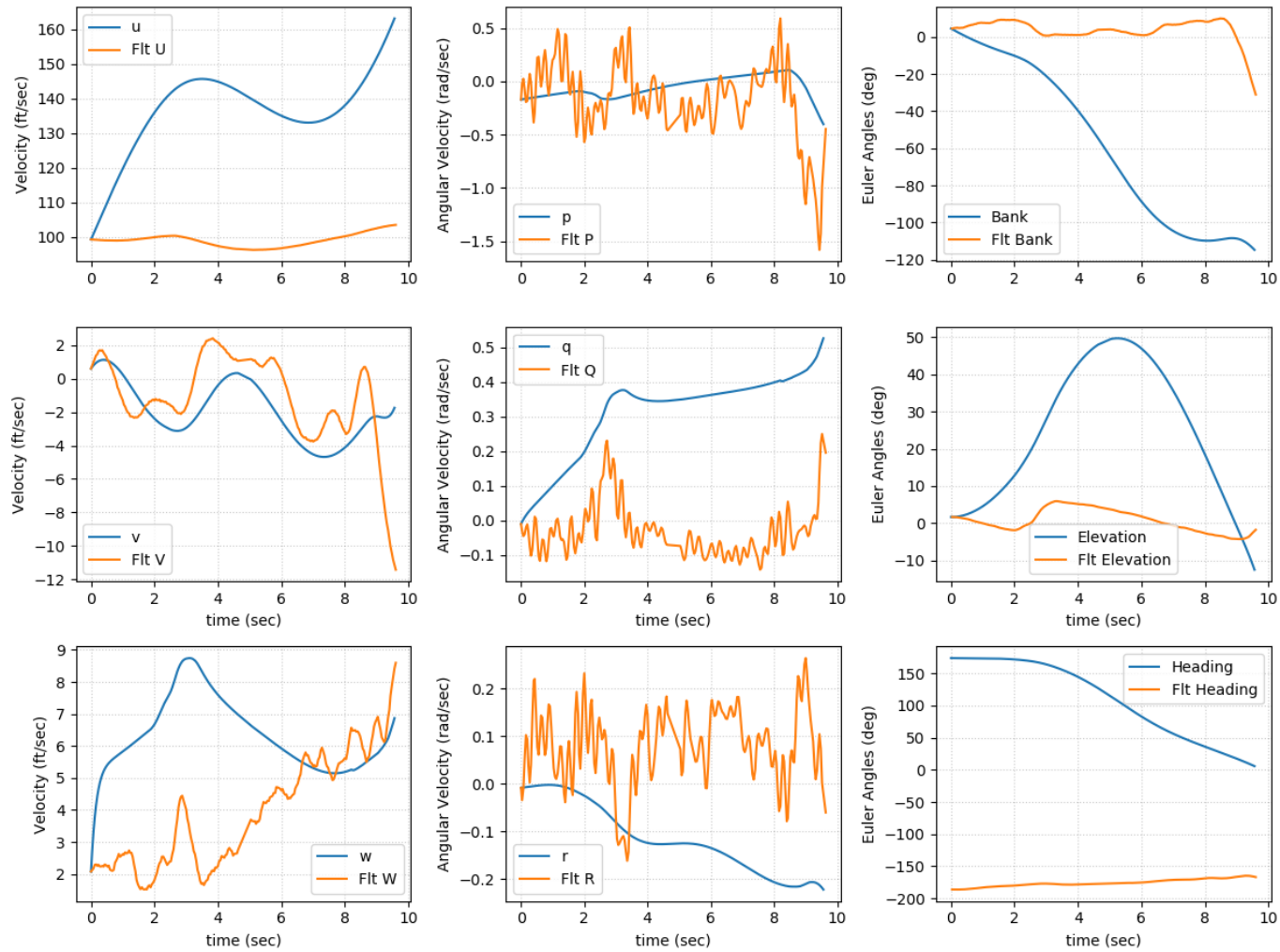


Figure 67: This is the fifth iteration of the simulation for Segment B. The blue shows the simulation data and the orange shows the actual flight data. This simulation uses the VCCW static thrust model.

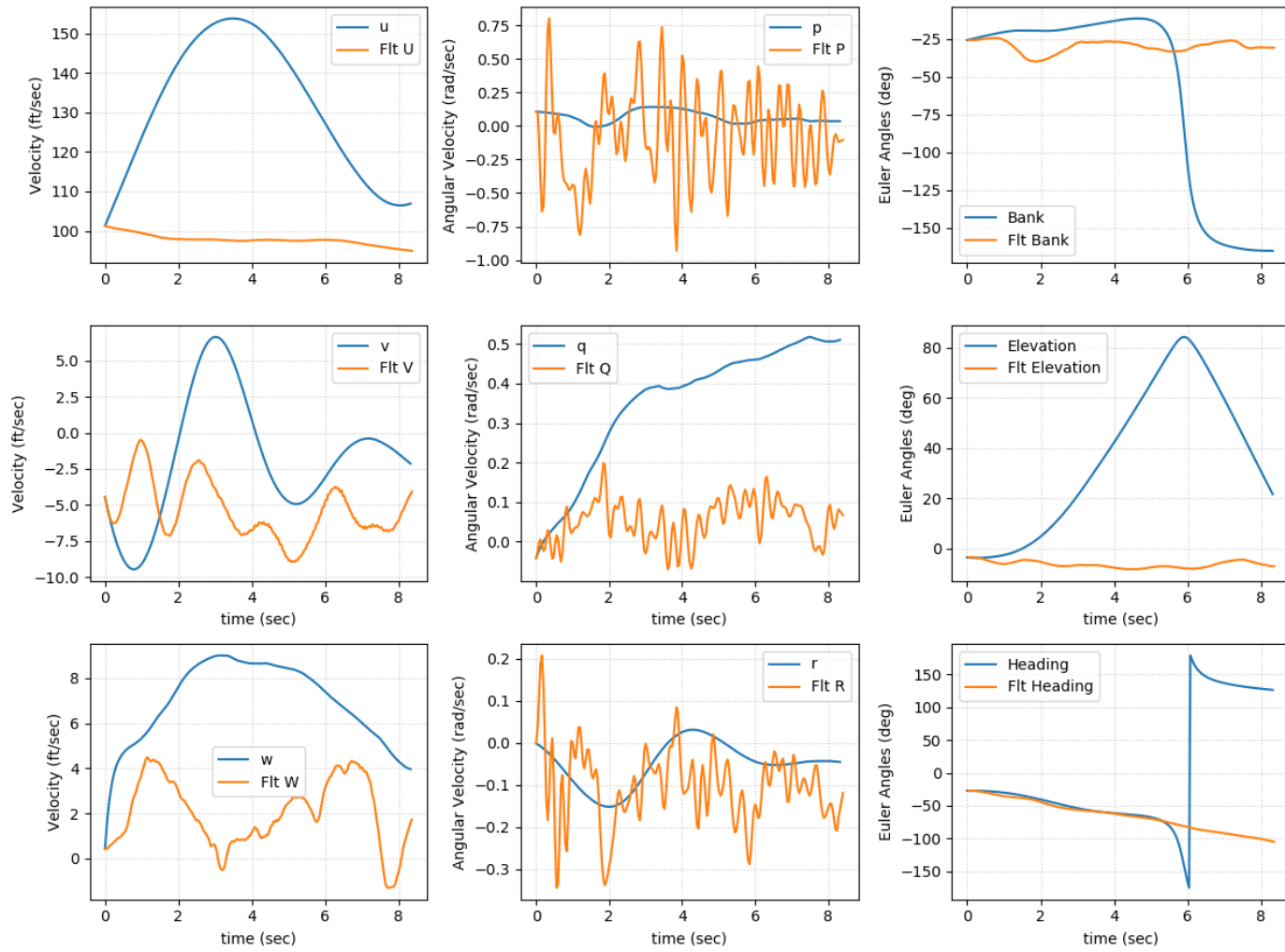


Figure 68: This is the fifth iteration of the simulation for Segment C. The blue shows the simulation data and the orange shows the actual flight data. This simulation uses the VCCW static thrust model.

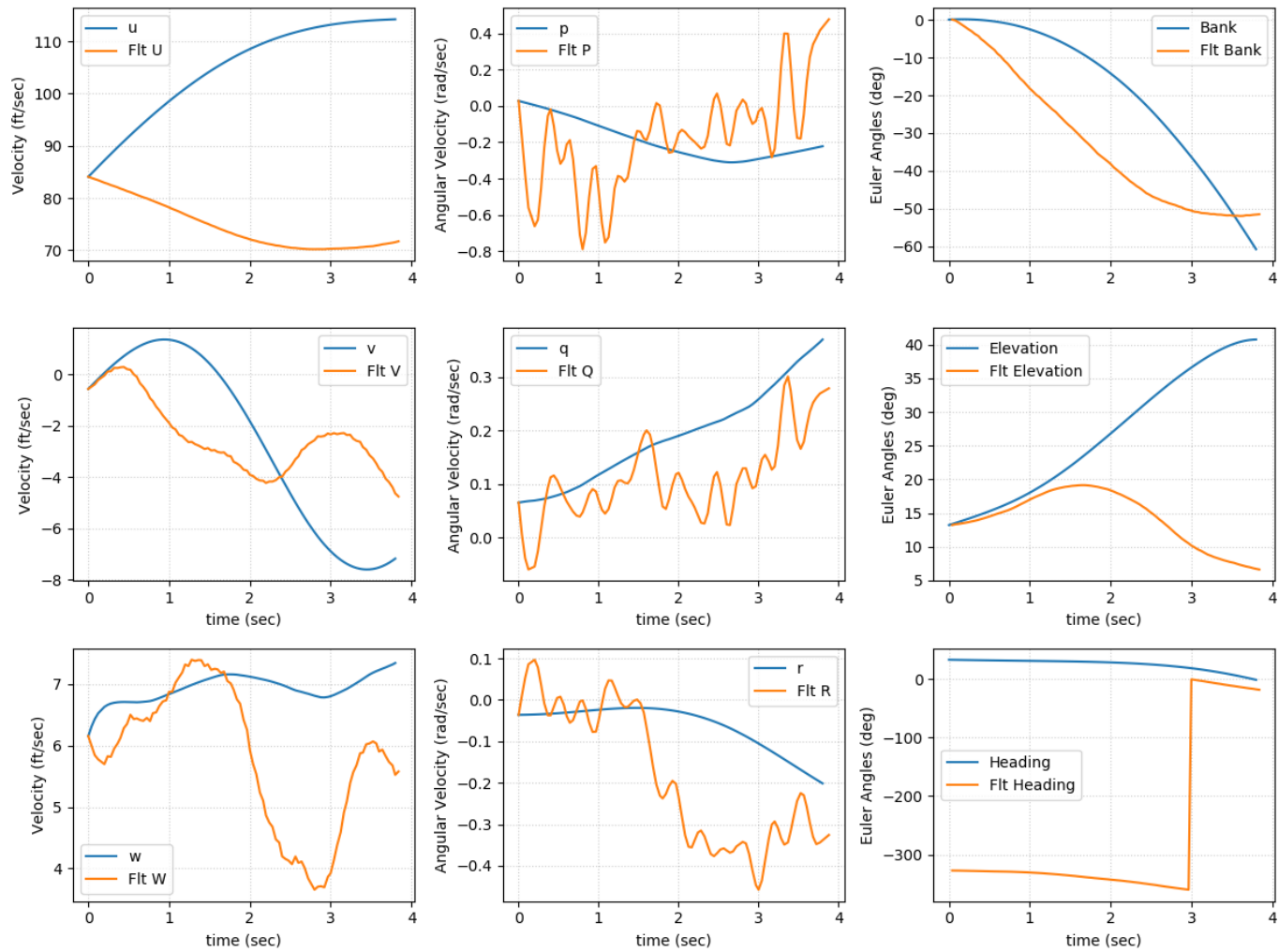


Figure 69: This is the fifth iteration of the simulation for the Segment D. The blue shows the simulation data and the orange shows the actual flight data. This simulation uses the VCCW static thrust model.

Bibliography

1. Carl Bereiter. Innovation in the absence of principled knowledge: The case of the wright brothers. *Creativity and Innovation Management*, 18(3):234–241, 2009.
2. Silvestro Barbarino, Onur Bilgen, Rafic M. Ajaj, Michael I. Friswell, and Daniel J. Inman. A review of morphing aircraft. *Journal of Intelligent Material Systems and Structures*, 22(9):823–877, 2011.
3. Lawren L. Gamble, Alexander M. Pankonien, and Daniel J. Inman. Stall Recovery of a Morphing Wing via Extended Nonlinear Lifting-Line Theory. *AIAA Journal*, 55(9):2956–2963, 2017.
4. Lawren L. Gamble and Daniel J. Inman. A tale of two tails: Developing an avian inspired morphing actuator for yaw control and stability. *Bioinspiration and Biomimetics*, 13(2), 2018.
5. L. L. Gamble and D. J. Inman. Why morphology matters in birds and UAV’s: How scale affects attitude wind sensitivity. *Applied Physics Letters*, 111(20), 2017.
6. Mica R Endsley and D Garland. Situation awareness analysis and measurement, chapter theoretical underpinnings of situation awareness. 2000.
7. Joshua D. Hodson, Douglas F. Hunsaker, and Robert E. Spall. Wing optimization using dual number automatic differentiation in MachUp. In *AIAA SciTech Forum - 55th AIAA Aerospace Sciences Meeting*. American Institute of Aeronautics and Astronautics Inc., 2017.

8. Ryan C Petrie. Characterization of the Variable Camber Compliant Wing using a Vortex Panel Method. Technical report, Air Force Institute of Technology, Wright-Patterson AFB, 2017.
9. V. P. Galantai, A. Y.N. Sofla, S. A. Meguid, K. T. Tan, and W. K. Yeo. Bio-inspired wing morphing for unmanned aerial vehicles using intelligent materials. *International Journal of Mechanics and Materials in Design*, 8(1):71–79, 3 2012.
10. Jae Sung Bae, T. Michael Seigler, and Daniel J. Inman. Aerodynamic and static aeroelastic characteristics of a variable-span morphing wing. *Journal of Aircraft*, 42(2):528–534, 2005.
11. Terrence A Weisshaar. Morphing Aircraft Technology-New Shapes for Aircraft Design. Technical report, Purdue University, Lafayette, 2006.
12. Yudi Heryawan, Hoon Cheol Park, Nam Seo Goo, Kwang Joon Yoon, and Yung Hwan Byun. Structural design, manufacturing, and wind tunnel test of a small expandable wing. In *Key Engineering Materials*, volume 306-308 II, pages 1157–1162, 2006.
13. Nam S. Goo Kwang J. Yoon Yung H. Byun Yudi Heryawan, Hoon C. Park. Design and demonstration of a small expandable morphing wing. *Smart Structures and Integrated Systems*, (Proc. SPIE 5764), 2005.
14. Gregory E. Dockter and Brian K. Hamilton. Geometric morphing wing with expandable spars, 2003.
15. H.F. Parker. The Parker Variable Camber Wing. Technical report, National Advisory Committee for Aeronautics, Washington DC, 1920.
16. Shawn E. Gano, Victor M. Pérez, John E. Renaud, Stephen M. Batill, and Brian Sanders. Multilevel variable fidelity optimization: Of a morphing unmanned

- aerial vehicle. In *Collection of Technical Papers - AIAA/ASME/ASCE/AHS/ASC Structures, Structural Dynamics and Materials Conference*, volume 4, pages 2777–2792, 2004.
17. Shawn E. Gano and John E. Renaud. Optimized unmanned aerial vehicle with wing morphing for extended range and endurance. In *9th AIAA/ISSMO Symposium on Multidisciplinary Analysis and Optimization*. American Institute of Aeronautics and Astronautics Inc., 2002.
 18. Hugo Rodrigue, Seunghyun Cho, Min Woo Han, Binayak Bhandari, Jae Eul Shim, and Sung Hoon Ahn. Effect of twist morphing wing segment on aerodynamic performance of UAV. *Journal of Mechanical Science and Technology*, 30(1):229–236, 1 2016.
 19. R. Pecora, F. Amoroso, and L. Lecce. Effectiveness of wing twist morphing in roll control. *Journal of Aircraft*, 49(6):1666–1674, 11 2012.
 20. Chinmaya Panda. Aeroelasticity - In General and Flutter Phenomenon. Technical report, Engineering and Industrial Services: TATA Consultancy Services Limited, Bangalore, 2009.
 21. Gerald Miller. Active Flexible Wing Program. Technical report, Rockwell International, Los Angeles, 1988.
 22. Zheng Min, Vu Khac Kien, and Liew J Y Richard. Aircraft morphing wing concepts with radical geometry change. *IES Journal Part A: Civil and Structural Engineering*, 3(3):188–195, 2010.
 23. Michael D. Skillen and William A. Crossley. Developing morphing wing weight predictors with emphasis on the actuating mechanism. In *Collection of Technical*

Papers - AIAA/ASME/ASCE/AHS/ASC Structures, Structural Dynamics and Materials Conference, volume 8, pages 5422–5438, 2006.

24. Yan Ren, Geng Liu, and Haibo Dong. Effect of surface morphing on the wake structure and performance of pitching-rolling plates. In *53rd AIAA Aerospace Sciences Meeting*. American Institute of Aeronautics and Astronautics Inc, AIAA, 2015.
25. Joseph Habeck and Peter Seiler. Moment of Inertia Estimation Using a Bifilar Pendulum. Technical report, University of Minnesota, Minnesota, 2016.
26. J Everaerts. THE USE OF UNMANNED AERIAL VEHICLES (UAVS) FOR REMOTE SENSING AND MAPPING. Technical report, Flemish Institute for Technological Research, Mol, Belgium, 2008.
27. Katherine D Mullens, Estrellina B Pacis, Stephen B Stancliff, Aaron B Burmeister, Thomas A Denewiler, Michael H Bruch, and H R Everett. An Automated UAV Mission System. *AUVSI Unmanned Systems in International Security*, 2003.
28. Kenneth Smith, Jeffrey Butt, Michael R. Von Spakovsky, and David Moorhouse. A study of the benefits of using morphing wing technology in fighter aircraft systems. In *Collection of Technical Papers - 39th AIAA Thermophysics Conference*, volume 2, pages 1497–1508, 2007.
29. Warren Phillips. *Mechanics of Flight*. John Wiley & Sons, Hoboken, second edition, 2010.
30. Douglas F. Hunsaker, Warren F. Phillips, and James J. Joo. Aerodynamic Shape Optimization of Morphing Wings at Multiple Flight Conditions. *55th AIAA Aerospace Sciences Meeting*, (January):1–14, 2017.

31. Douglas F. Hunsaker, Zachary S. Montgomery, and James J. Joo. Lifting-Line Analysis of Wing Twist to Minimize Induced Drag During Pure Rolling Motion. *AIAA Scitech 2019 Forum*, (January):1–24, 2019.
32. Madison J Montgomery. ACTIVE CONTROL OF A MORPHING WING AIRCRAFT AND FAILURE. Technical report, Air Force Institute of Technology, Wright-Patterson AFB, 2019.
33. Adam Niksch, John Valasek, Thomas Strganac, and Leland Carlson. Six Degree-of-Freedom Dynamical Model of a Morphing Aircraft. *AIAA Atmospheric Flight Mechanics Conference*, (August), 2009.
34. Boyd Perry, Stanley R. Cole, and Gerald D. Miller. Summary of an active flexible wing program. *Journal of Aircraft*, 32(1):10–15, 1995.
35. Cody Lafountain, Kelly Cohen, and Shaaban Abdallah. Camber controlled airfoil design for morphing UAV. In *47th AIAA Aerospace Sciences Meeting including the New Horizons Forum and Aerospace Exposition*, 2009.
36. Onur Bilgen, Michael I Friswell, Singleton Park, Kevin B Kochersberger, Daniel J Inman, and George R Goodson. Surface Actuated Variable - Camber and Variable - Twist Morphing Wings Using Piezocomposites. Technical report, Denver, 2011.
37. Andrew J Lee, Amin Moosavian, and Daniel J Inman. Control and characterization of a bistable laminate generated with piezoelectricity. *Smart Materials and Structures*, 26(8):085007, 2017.
38. Daniel Inman, Kevin Kochersberger, Onur Bilgen, Edward Diggs, and Andrew Kurdila. Morphing Wing Aerodynamic Control via Macro-Fiber-Composite Actuators in an Unmanned Aircraft. (May):1–17, 2012.

39. Ning Feng, Liwu Liu, Yanju Liu, and Jinson Leng. A bio-inspired, active morphing skin for camber morphing structures. *Smart Materials and Structures*, 24(3), 3 2015.
40. James J Joo, Christopher R Marks, and Lauren Zientarski. ACTIVE WING SHAPE RECONFIGURATION USING A VARIABLE CAMBER COMPLIANT WING SYSTEM. Technical report, Copenhagen, 2015.
41. James J. Joo, Christopher R. Marks, Lauren Zientarski, and Adam Culler. Variable camber compliant wing - design. In *23rd AIAA/AHS Adaptive Structures Conference*. American Institute of Aeronautics and Astronautics Inc., 2015.
42. Youngmin Jo, Seongim Choi, Lauren Zientarski, and James J. Joo. Aerodynamic Characteristics and Shape Optimization of a Variable Camber Compliant Wing. *34th AIAA Applied Aerodynamics Conference*, (June):1–19, 2016.
43. Christopher R. Marks, Lauren Zientarski, Adam J. Culler, Benjamin Hagen, Brian M. Smyers, and James J. Joo. Variable Camber Compliant Wing - Wind Tunnel Testing. *23rd AIAA/AHS Adaptive Structures Conference*, (January):1–14, 2015.
44. Randal Beard and Timothy McLain. *Unmanned Aircraft Systems*. Princeton University Press, Princeton, 2011.
45. Robert C. Nelson. *Flight stability and automatic control*. WCB/McGraw Hill, 1998.
46. Lorenz Meier. Pixhawk, 2020.
47. Zachary S Montgomery and Douglas F Hunsaker. A Methodology for Roll Control of Morphing Aircraft. Technical Report January, Utah State University, 2019.

48. Matt R. Jardin and Eric R. Mueller. Optimized measurements of unmanned-air-vehicle mass moment of inertia with a bifilar pendulum. *Journal of Aircraft*, 46(3):763–775, 5 2009.
49. W. F. Phillips and D. O. Snyder. Modern adaptation of Prandtl’s classic lifting-line theory. *Journal of Aircraft*, 37(4):662–670, 2000.
50. R T Jones. NASA Reference Publication 1050 Classical Aerodynamic Theory. Technical report, Ames Research Center, Moffett Field, 1979.
51. William. Mendenhall, Robert J. Beaver, and Barbara M. Beaver. *Introduction to probability and statistics*. Brooks/Cole, 2013.
52. Gene F. Franklin, J. David Powell, and Michael Workman. *Digital Control of Dynamic Systems*. Ellis-Kagle Press, Half Moon Bay, third edition, 1998.
53. All Markus Mueller. eCalc, 2018.
54. Waqas Khan and Meyer Nahon. Toward an accurate physics-based UAV thruster model. *IEEE/ASME Transactions on Mechatronics*, 18(4):1269–1279, 2013.
55. Pierre-Jean Bristeau, Philippe Martin, Erwan Salaün, and Nicolas Petit. The role of propeller aerodynamics in the model of a quadrotor UAV. Technical report, Budapest, 2009.
56. Dongwon Jung and Panagiotis Tsiotras. Modeling and hardware-in-the-loop simulation for a small unmanned aerial vehicle. In *Collection of Technical Papers - 2007 AIAA InfoTech at Aerospace Conference*, volume 1, pages 581–593, 2007.

REPORT DOCUMENTATION PAGE					<i>Form Approved</i> <i>OMB No. 0704-0188</i>	
The public reporting burden for this collection of information is estimated to average 1 hour per response, including the time for reviewing instructions, searching existing data sources, gathering and maintaining the data needed, and completing and reviewing the collection of information. Send comments regarding this burden estimate or any other aspect of this collection of information, including suggestions for reducing this burden to Department of Defense, Washington Headquarters Services, Directorate for Information Operations and Reports (0704-0188), 1215 Jefferson Davis Highway, Suite 1204, Arlington, VA 22202-4302. Respondents should be aware that notwithstanding any other provision of law, no person shall be subject to any penalty for failing to comply with a collection of information if it does not display a currently valid OMB control number. PLEASE DO NOT RETURN YOUR FORM TO THE ABOVE ADDRESS.						
1. REPORT DATE (DD-MM-YYYY)		2. REPORT TYPE		3. DATES COVERED (From — To)		
26-03-2020		Master's Thesis		Sept 2018 — Mar 2020		
4. TITLE AND SUBTITLE				5a. CONTRACT NUMBER		
Flight Characteristic Verification of the Variable Camber Compliant Wing				5b. GRANT NUMBER		
				5c. PROGRAM ELEMENT NUMBER		
				5d. PROJECT NUMBER		
				5e. TASK NUMBER		
6. AUTHOR(S)				5f. WORK UNIT NUMBER		
Acosta, Sharee B, 2d Lt						
7. PERFORMING ORGANIZATION NAME(S) AND ADDRESS(ES)					8. PERFORMING ORGANIZATION REPORT NUMBER	
Air Force Institute of Technology Graduate School of Engineering and Management (AFIT/EN) 2950 Hobson Way WPAFB OH 45433-7765					AFIT-ENG-MS-20-M-003	
9. SPONSORING / MONITORING AGENCY NAME(S) AND ADDRESS(ES)					10. SPONSOR/MONITOR'S ACRONYM(S)	
AFRL Advanced Structural Concepts Team James J. Joo, Ph.D 2790 D St. WPAFB, OH 45433-7402 james.joo.1@us.af.mil (937) 656-8759					AFVRL/RQVS	
12. DISTRIBUTION / AVAILABILITY STATEMENT DISTRIBUTION STATEMENT A: APPROVED FOR PUBLIC RELEASE; DISTRIBUTION UNLIMITED.					11. SPONSOR/MONITOR'S REPORT NUMBER(S)	
13. SUPPLEMENTARY NOTES This work is declared a work of the U.S. Government and is not subject to copyright protection in the United States.						
14. ABSTRACT Morphing wing technology gives aircraft the ability to change wing shape to control the aircraft and flight performance characteristics. AFIT, AFRL and USU Aero Lab have collaborated to design and test a variable camber compliant wing (VCCW) on an small unmanned aerial vehicle (UAV). Flight tests demonstrated the wing performance and provided data to refine a VCCW flight simulator. Work was completed with the USU AeroLab-generated MachUp and the actual flight data to improve the simulator to provide results close to those of the actual flight test. The research provides a tool to reduce time and cost for future flight testing for VCCW development.						
15. SUBJECT TERMS variable camber compliant wing, simulation, UAV flight test, aircraft control						
16. SECURITY CLASSIFICATION OF:			17. LIMITATION OF ABSTRACT		18. NUMBER OF PAGES	
a. REPORT	b. ABSTRACT	c. THIS PAGE			19a. NAME OF RESPONSIBLE PERSON	
U	U	U	UU		Dr. Robert Leishman, AFIT/ENG	
					19b. TELEPHONE NUMBER (include area code)	
					(937) 255-3636x4755; Robert.Leishman@afit.edu	